

## ABSTRACT

Title of Document: FORWARD HEATING IN WIND-DRIVEN  
FLAMES

Wei Tang, Doctor of Philosophy, 2017

Directed By: Associate Professor Michael J. Gollner  
Department of Fire Protection Engineering

Wildland fires pose a significant threat to the environment and society at large. The large number of unknowns makes wildland fire predictions much harder than those typically encountered within the built environment, especially under the influence of wind. The spread rate of a fire depends largely on forward heating from the flame to unburnt fuels, however few measurements of heat fluxes from wind-driven flames exist. In wildland fires, the intermittent nature of flame is also thought to be uniquely important to the flame spread process. In this work, both averaged and time-dependent aspects of the flame are studied, including the total heat flux distribution on the downstream surface, flame extension and attachment, and frequencies of intermittent flame movements. Correlations of these properties, dependent on both fire size and ambient wind, will provide a means to describe the thermal exposure during fuel heating and ignition in wind-driven wildland fires. This data will provide a basis for both understanding and model development for wildland fire spread as well as provide a dataset for future numerical validation of computational fluid dynamic models.

Detailed laboratory experiments were performed on line fires under forced flow with a variety of ambient wind velocities and fire sizes. Local heat fluxes were measured onto a nearly adiabatic surface downstream of a line burner. The downstream heat flux distribution was correlated as a piecewise function with the local Richardson number in two regimes, the first with higher heat fluxes, where the flame remained attached the downstream surface and the second with a steeper decay of heat fluxes. This observation was further corroborated by analysis of side-view images of the flame, which showed the attachment location was linearly correlated with the location where the  $Ri_x$  equaled unity. The flame forward pulsation frequency and the flame-fuel contact frequency were also extracted. Scaling analysis indicates that they can be well correlated with  $Fr$ ,  $Q^*$ , and local  $Ri_x$  respectively. The location of maximum pulsation frequency,  $x_{max}$ , for each burner/wind configuration was also obtained using the VITA technique. Further study indicates that  $x_{max}$  can be well estimated using mean flame properties.

FORWARD HEATING IN WIND-DRIVEN FLAMES

By

Wei Tang

Dissertation submitted to the Faculty of the Graduate School of the  
University of Maryland, College Park, in partial fulfillment  
of the requirements for the degree of  
Doctor of Philosophy  
2017

Advisory Committee:  
Professor Michael J. Gollner, Chair  
Professor Elaine Oran, Dean's Representative  
Professor Arnaud C. Trouvé  
Professor Peter B. Sunderland  
Professor Andre W. Marshall

© Copyright by  
Wei Tang  
2017

## DEDICATIONS

To my girlfriend Shaoli Lin, and my family, who keeps me motivated and is always there for me.

## ACKNOWLEDGEMENTS

Three years ago, when I first set foot on to the United States and came to the University of Maryland, I did not know that three years would pass so fast. But I have always been so lucky. Throughout all these years studying and doing research at universities, I have met the most dedicated advisors and the best colleagues and the most wonderful friends in the world, without whose help and guidance, this dissertation would never be possible.

First and foremost, I need to thank my advisor, Dr. Michael J. Gollner, who I think is not just one of the best professors, but one of the best person I have ever known. He impressed me with his dedicated work ethic, during this past 3 years, he has always been there throughout any difficulty I have met in the research. He has showed tremendous patience, even at the times when I felt very frustrated and had no clue how to proceed. It's been an absolute pleasure and honor to work with him and there is just so much to learn from him that 3 years seems not enough. Michael will remain as my mentor and advisor for life. I am forever thankful to all he has done to help and support me during my time at the University of Maryland.

I also would like to thank my committee members, Dr. Elaine S. Oran, who is serving as the Dean's Representative. Dr. Oran is such a knowledgeable and such a kind person that almost all the Ph.D. students in the Department of Fire Protection Engineering will invite her to be their committee member. Sorry Dr. Oran, there's just so much work for you, because we love you so much.

I also would like to thank Dr. Arnaud Trouve for all his help and support during the course of my Ph.D. Dr. Trouve has always provided some of the best advice in terms of doing a

detailed experimental work. His critical thinking from a modeler's perspective has been a great addition to this research work.

Thanks are also due to Dr. Sunderland and Dr. Marshall, for both serving on my dissertation committee and being so insightful and helpful during my dissertation proposal. Thank you so much for sparing your time reading and reviewing this manuscript. It's been just great to work with some of the leading experts in Fire Protection Engineering.

My colleagues and friends at the FPE department have made my life here so meaningful and colorful that I will never forget. Colin Miller helped me so much in my research and experiments that sometimes his own work was delayed. He is such a cool and nice guy that I have never seen him get angry at anyone or anything. He bought me my first beer in the U.S, and I brought him some little gifts when I return from China. We have worked together and gone to the gym together, he has been my best friend to date. My interactions with Ajay Singh, Daniel Gorham, Haiqing Guo, Xuan Liu, Zhao Zhao, Salman Verma, Cong Zhang, Yan Ding, Xiaoyue Pi, Nate May, Raquel Hakes, Sara Caton, Ali Tohidi, Pietro Maisto, Sriram Bharath, Lin Jiang, Kun Zhao, Yu Hu, Qiong Liu, Xinjie Huang, Dennis Kim, Zhengyang Wang, Wuquan Cui, Eric Link, Matthew Weston-Dawkes have been very joyful and I am forever grateful to all the help you have given me.

Also, special thanks to the other professors in our department, Dr. James Milke, Dr. Stanislav Stoliarov, and our department's coordinators and technicians, Mary Lou, Sharon Hodgson, Olga Zeller, Christine O'Brien for all your help, you made our research much easier.

I owe my heaviest debt to my family, my father, my mother, my sister, and my brother, who have always unwaveringly supported me no matter what, and who have always accompanied me throughout my life. I am so grateful to the help and trust you have given me.

Last but not least, I want to thank Shaoli Lin for showing up in my life and being my girlfriend and my love. Thank you for always standing by my side and adding all those “flavors” to our life.

Financial support for this work was provided by the USDA Forest Service Missoula Fire Sciences Laboratory and National Fire Decision Support Center under collaborative agreement 13-CS-11221637-124 and the National Science Foundation under Grants no. 1554026 and 1331615.

# Table of Contents

List of figures.....	ix
List of tables.....	xiii
Nomenclature.....	xiv
Chapter 1: Introduction.....	1
1.1 Wildland Fire Spread Modeling.....	1
1.2 The Structure of Wild-Blown Flames.....	3
1.3 Outline of the Dissertation.....	4
Chapter 2: Literature Review.....	6
2.1 Wildland Fire Spread Modeling.....	6
2.2 Flame Dynamics.....	8
2.3 Heat Flux Distribution.....	10
2.4 Flame Pulsations and Movement.....	14
2.5 Flame Extension and Flame Attachment.....	16
2.6 Summary.....	19
Chapter 3: Experimental Facility and Instrumentation.....	20
3.1 Wind Tunnel Setup.....	20
3.2 Gas Burner.....	22
3.3 Velocity Characterization.....	22
3.4 Temperature Measurements and Traverse System.....	27
3.5 Total Heat Flux Gauge.....	28

3.6 Radiometer .....	30
3.7 Digital Camera .....	31
3.8 Data Acquisition Systems .....	31
3.9 Experimental Conditions .....	32
Chapter 4: Heat Flux Analysis .....	37
4.1 Total Heat Flux Distribution .....	37
4.2 Richardson Number Analysis .....	42
4.3 Non-dimensional Heat Flux and Correlations .....	49
4.4 Discussions and Conclusion .....	55
Chapter 5: Flame Fluctuations and Attachment Length .....	57
5.1 Measurement Methodology .....	57
5.2 Maximum Flame Pulsation Location .....	62
5.3 Flame Attachment Length .....	70
5.4 Discussions and Conclusion .....	74
Chapter 6: Flame Intermittent Frequencies .....	76
6.1 Flame Forward Pulsation Frequency .....	78
6.2 Flame-fuel Contact Frequency .....	84
6.3 Discussions and Conclusion .....	91
Chapter 7: Conclusions .....	94
Chapter 8: Future Work .....	96
Published Journal/Conference articles .....	98

Appendix A: Convective and radiative heat flux.....	100
Bibliography .....	104

## List of Figures

Figure 1. Diagram of a wind-blown flame illustrating regions existing along the surface as well as movements that occur within the flame. ....	3
Figure 2. Wildland fire triangle (fuel, weather, and topography) and a representative schematic of fire propagation [14].....	7
Figure 3. An illustration of flame dynamics and the resulting instabilities from experiments performed by Finney et al. [10] are shown. A number of both streamwise and spanwise instabilities are shown to form which force flames and hot gases through “troughs” in the flame zone to intermittently heat unburned fuels ahead of the flame front.....	9
Figure 4. Comparison of wind-driven fire behaviors with that under quiescent conditions (from Rothermel [16-18]). ....	10
Figure 5. Photo of the wind tunnel apparatus .....	21
Figure 6. Schematic including dimensions of the wind tunnel [52] .....	21
Figure 7. Hot wire anemometer used in his study [78 dantec]. ....	23
Figure 8. Measurement locations for wind profile measurements.....	24
Figure 9. Low velocity (1.12 m/s) profile with height over the surface. ....	25
Figure 10. High velocity (2.15 m/s) profile with height over the surface. ....	25
Figure 11. Turbulence intensity profile with height and downstream distance over the surface (1.12 m/s, low wind case).....	26
Figure 12. Turbulence intensity profile with height and downstream distance over the surface (2.15 m/s, high wind case).....	27
Figure 13. Thermocouple and mount used in temperature measurements [79].....	28

Figure 14. The Vatel total heat flux gauge and amplifier used in experiments [80].	29
Figure 15. The calibration used for the Vattelle total heat flux gauge in the cone calorimeter. ....	29
Figure 16. Schematic of the Medtherm radiometer used from the manufacturer [81].	31
Figure 17. National Instrument data acquisition systems used in the study [82] .....	32
Figure 18. Experimental setup downstream of the tunnel outlet .....	34
Figure 19. Heat flux data taken on 11 cm downstream averaged for 6.3 kW, 9.5 kW fire size, 1.14 m/s, 1.62 m/s wind speed scenarios for a period of 150 s. ....	38
Figure 20. Comparison of heat flux profiles for different wind velocities and fire sizes	39
Figure 21. Experimental photos showing different flame shapes under wind.....	40
Figure 22. Heat flux distribution under low wind velocities .....	42
Figure 23. Vertical temperature profile taken 16.5 cm downstream of the trailing edge of the burner, with a fire size of 9.5 kW and a wind velocity of 1.91 m/s.....	44
Figure 24. Heat flux distribution under high winds (1.62 and 1.91 m/s).....	46
Figure 25. Heat flux distribution under high winds (2.14 and 2.45 m/s).....	47
Figure 26. Local $Ri_x$ number under high winds (1.62 and 1.91 m/s).....	48
Figure 27. Local $Ri_x$ number under high winds (2.14 and 2.45 m/s).....	49
Figure 28. Local $Ri_x$ number with local heat flux (9.5 kW, 1.91 m/s).....	51
Figure 29. Local $Ri_x$ number with local heat flux (7.9 kW, 2.14 m/s).....	52
Figure 30. Comparison of dimensionless downstream location at $Ri_x=1$ with the peak heat flux value.....	53
Figure 31. Dimensionless local total heat flux with local $Ri_x$ .....	55

Figure 32. Flame location between two time steps in a forced flow experiment. The flame attachment location ( $x_a$ ) is measured from the downstream edge of the burner to edge of the flame within the attachment region.....	58
Figure 33. Flame image processing based on luminosity .....	59
Figure 34. A side-view of mean flame properties including the flame height $H_f$ , flame length $L_f$ , maximum frequency location $x_{max}$ , mean flame attachment length $x_a$ , horizontal flame length $x_f$ and flame tilt angle $\theta$ .....	60
Figure 35. Fluctuating flame extension with time .....	61
Figure 36. Probability Density Function (PDF) of normalized flame position .....	62
Figure 37. Horizontal flame length versus the location of maximum frequency, $x_{max}$ .....	65
Figure 38. Histograms of flame extension length, $x_a$ for a $25 \times 5 \text{ cm}^2$ burner. ....	66
Figure 39. Probability of normalized flame attachment length, $x_a / \bar{x}_a$ for different fire sizes and wind velocities.....	68
Figure 40. The variance, $\sigma^2$ of the normalized flame attachment length, $x_a / \bar{x}_a$ , from Gaussian curve fits versus $Fr^{2/3}/Q^*$ .....	70
Figure 41. Averaged flame image from experimental pictures .....	71
Figure 42. Averaged flame images under different wind velocities show the attachment length ( $L_{attach}$ ) of the flame to the surface with scales. Regions between the two blue dashed lines represent the burner depth, while the red solid lines, which are 5 mm in height, represent the flame attachment length measured along the downstream surface. ....	72
Figure 43. $L_{Ri_x=1}^*$ with dimensionless flame attachment length $L_{attach}^*$ where error bars shown represents variation in the chosen threshold heights .....	74

Figure 44. Flame location between two time steps in a forced flow experiment .....	78
Figure 45. Fluctuating heat flux signals over time .....	79
Figure 46. Level-crossing frequency and Probability Density Function (PDF) shows the flame locations on the downstream surface (7.9 kW, 2.45 m/s).....	80
Figure 47. Forward pulsation frequency with different wind velocities and fire size	81
Figure 48. Flame forward pulsation frequencies are found to scale with $Fr^{1/2}/Q^{*1/4}$ .	84
Figure 49. Heat flux raw data at 11 cm, with 9.5 kW fire size, 1.91 m/s wind velocity, and frequency spectrum obtained from FFT.....	86
Figure 50. Comparison of frequency obtained from the FFT for different wind velocities. ....	86
Figure 51. Local flame fuel contact frequency for 7.9 kW under different wind velocities .....	87
Figure 52. Non-dimensional frequency $f_c^+$ versus local $Ri_x$ .....	91
Figure 53. Temperature distribution on the downstream board with fire size 7.9 kW, wind velocity 2.14 m/s.....	101
Figure 54. Interpolation of the temperatures measured above the downstream surface	102
Figure 55. Temperature gradient at the surface .....	103

## List of tables

Table 1. Vatell heat flux gauge specifications from the manufacturer [80]. .....	30
Table 2. Experimental conditions (I) .....	35
Table 3. Experimental conditions (II).....	36

## Nomenclature

$f$  : Frequency (Hz)

$f_F$  : Flame forward pulsation frequency (Hz)

$f_C$  : Flame-fuel contact frequency (Hz)

$f_C^+$  : Non-dimensional flame-fuel contact frequency (-)

$D$ : Pool fire diameter (m)

$Fr$ : Dimensionless Froude number (-)

$g$ : Gravitational acceleration ( $m/s^2$ )

$St$ : Dimensionless Strouhal number (-)

$x_p$  : Burning (pyrolysis) region (m)

$\dot{q}_f''(x)$ : Heat flux distribution at  $x$  location ( $kW/m^2$ )

$x_f$  : Flame region (m)

$a$ : Constant in equation (5) (-)

$n$ : Constant in equation (5) (-)

$A, B, C$ : Constants in equation 32 (-)

$c_p$ : Specific heat ( $kJ/kgK$ )

$H_f$ : Flame height (cm)

$L$ : Burner characteristic length/hydraulic diameter (m)

$L_f$ : Flame length (cm)

$\dot{Q}$ : Heat release rate (kW)

$Q^*$ : Dimensionless heat release rate (-)

$T_0$  : Ambient temperature (K)

$\Delta T_f$ : Flame temperature rise over ambient (K)  
 $U_{wind}$ : Wind velocity (ms<sup>-1</sup>)  
 $u^+$ : Characteristic fuel velocity based on mass loss rate (ms<sup>-1</sup>)  
 $V$ : Buoyant flame velocity (ms<sup>-1</sup>)  
 $x_a$ : Flame extension location (cm)  
 $\bar{x}_a$ : Average flame extension location (cm)  
 $x_f$ : Horizontal flame length (cm)  
 $x_{max}$ : Location of maximum frequency (cm)  
 $\theta$ : Flame tilt angle (deg)  
 $\sigma^2$ : Variance of flame extension (-)  
 $\rho_0$ : Air density (kg/m<sup>3</sup>)  
 $L$ : Downstream location (m)  
 $L^*$ : Dimensionless downstream location (-)  
 $L^+$ : Characteristic length scale (m)  
 $S$ : Surface area of burner (m<sup>2</sup>)  
 $P$ : Perimeter of the burner (m)  
 $Gr_x$ : Local Grashof number (-)  
 $\beta$ : Thermal expansion coefficient (1/K)  
 $T_h$ : Hot fluid temperature (K)  
 $T_\infty$ : Ambient temperature (K)  
 $\nu$ : Viscosity (m<sup>2</sup>/s)  
 $Re_x$ : Local Reynolds number (-)

$b$ : Constant chosen as 2 in equation (12) (-)

$Ri_x$ : Local Richardson number (-)

$T_f$ : Flame temperature (K)

$L_{Ri_x=1}^*$ : Dimensionless location where  $Ri_x=1$  (-)

$L_{peak}^*$ : Dimensionless location where peak heat flux is observed (-)

$\dot{q}_f^*$ : Dimensionless heat flux (-)

$A$ : Atwood number (-)

$\rho_a$ : Density of air ( $\text{kg}/\text{m}^3$ )

$c_p$ : Specific heat capacity of air ( $\text{J}/\text{kgK}$ )

$\dot{q}_{f,c}''$ : Convective heat flux ( $\text{kW}/\text{m}^2$ )

$\dot{q}_{f,r}''$ : Radiative heat flux ( $\text{kW}/\text{m}^2$ )

$\dot{q}_{s,rr}''$ : Re-radiation heat flux ( $\text{kW}/\text{m}^2$ )

$k_w$ : Conductivity ( $\text{W}/\text{m}\cdot\text{K}$ )

$\sigma$ : Stephan-Boltzmann constant ( $\text{kgs}^{-3}\text{K}^{-4}$ )

$D_H$ : Hydraulic diameter (m)

$S$ : Area of the burner top surface ( $\text{m}^2$ )

$P$ : Perimeter of the burner top surface (m)

$L_{attach}$ : Flame attachment length on the downstream surface (m)

$L_{attach}^*$ : Dimensionless flame attachment length (-)

$h$ : Convective heat transfer coefficient ( $\text{W}/(\text{m}^2\text{K})$ )

$T'$ : Temperature gradient ( $\text{K}/\text{m}$ )

$\dot{m}''$ : Mass burning rate ( $\text{kg}/\text{m}^2\text{s}$ )

$u^*$  : Non-dimensional wind velocity (-)

VITA: Variable-Interval-Time-Average

PDF: Probability Density Function

$I_R$  : Reaction intensity

$\phi_w$  : The wind coefficient

$\phi_s$  : The slope coefficient

$\rho_b$  : Oven-dried bulk density

$\varepsilon$  : Effective heating number

$Q_{ig}$  : Heat of pre-ignition

## **Chapter 1: Introduction**

Despite many years of study, mankind's understanding of wildland fires is still incredibly limited. The large scale and destructive nature of these fires makes them both important for society and incredibly difficult to study. Generally, wildland fires can occur or progress between two stages, from desirable natural fires that have occurred over the landscape for millennia and second, unwanted wildland fire disasters, wildfires. Wildfires as a disaster are a growing concern around the world. They pose a significant threat not only to the natural landscape, but also to surrounding environments and populations via smoke and other effluents, downstream effects such as erosion and floods, and the destruction of properties and threat to life in the Wildland-Urban Interface (WUI) [1, 2]. Many factors, most importantly deficient fuel management practices, the movement of persons into the WUI, and a changing climate have caused an explosive growth in the budget for wildland fire suppression in the United States. Unfortunately, these factors are predicted to get worse over the coming decades, necessitating research that may mitigate future disasters [3].

### **1.1 Wildland Fire Spread Modeling**

Accurately modelling the spread of wildland fires has become a key goal for the fire research community [4]. Wildland fire modeling is now used for a number of essential purposes including fire risk mapping, fire management, suppression planning and, in a limited sense, active fire suppression. In the future, accurate predictions of ongoing wildfires will be an essential source of data for fighting fires. It will be possible, for instance, to calculate what the chance of a fire spreading towards a community is, predicting the largest possible extent, when and where it might endanger firefighters, better predict the most cost-effective prescribed burning locations and improve fire suppression

and evacuation strategies. While current models can do some of this, they are limited by inaccuracies both in the model and input data [5, 6]. While there are many efforts under way to improve input data, future predictions in time will remain severely limited if the physical model for fire spread is incorrect.

The dynamics of wind-driven fires, especially those resembling a line fire configuration similar to spreading wildland fires have not been well documented, instead focusing on their steady or averaged characteristics [7]. While Albini studied the response of a spreading fire to a non-steady wind [8, 9], he did not account for fluctuations produced by the flame front itself or the effects of these motions on unsteady heating. Recent results by Finney and Cohen et al [10, 11] have revealed the influence of intermittent convective heating on wildland flame spread due to the small diameter of wildland fuels which are incredibly sensitive to rapid convective heating and cooling but have a low response to radiation due to a low surface to volume ratio. Despite this recent discovery, no work has yet addressed the intermittent effects of heating from wind-blown flames.

Information on steady and intermittent heating and flame-movement will help us to understand how fuel downstream of the flame front will be heated as a function of time and thus fill in an important part of the puzzle of how wildland fires spread. The convective heating found in previous studies from Finney et al. [4] were hypothesized to appear from buoyant instabilities in the fire itself. Similar behavior has been observed in laboratory-scale fires with steady gas burners [12], indicating this may be a reasonable configuration from which to study the intermittent behavior of wind-blown flames.

## 1.2 The Structure of Wild-Blown Flames

A detailed look at the structure of wind-blown flames reveals that there are a variety of structures and regions which vary in both time-dependent and averaged characteristics. Figure 1 shows an image of a wind-blown flame from a stationary burner that at first appears attached along the downstream surface, but eventually lifts into a tilted flame. In this work, three regions will be defined to describe this region. First, a flame attachment region exists where the flame is visibly forced to attach the surface, occurring for some distance downstream of the burner since the wind momentum overpowers buoyancy from the flame. As the flame moves forward, buoyancy increases in proportion to the wind momentum and the flame enters a transitional, “intermittent” region, where the flame fluctuates between competition with wind momentum and flame buoyancy. After this region, the flame is finally lifted due to the dominant role of buoyancy which grows with distance as distribute reactions continue to occur within the flame.

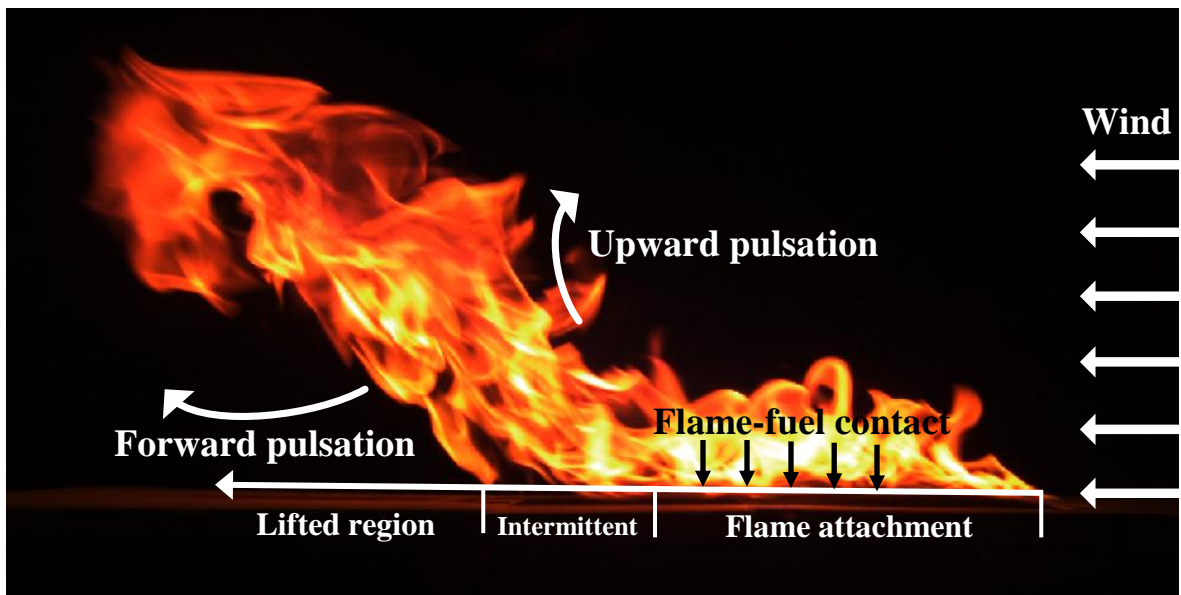


Figure 1. Diagram of a wind-blown flame illustrating regions existing along the surface as well as movements that occur within the flame.

In the process of the flame moving forward, a two-directional fluctuating behavior is anticipated, also indicated on Fig. 1. One is *forward pulsation*, where the flame intermittently flickers forward onto the downstream surface ahead of the flame front. In a spreading fire scenario, this may potentially reach more unburnt fuels and heat them, albeit for short times. This likely occurs due to a competition between momentum-driven wind and a counter-clockwise recirculation zone at the flame front, a buoyant instability similar to puffing pool fires, or a combination of the two. The other is *intermittent contact*, which appears most rapid in the region between the attached flame length and the lifted region. The up-and-down motion of the flame here is most likely due to a local buoyant instability and might subject to change along the downstream distance. Separately measuring these two components will help to determine the influence intermittent heating has in each of the mentioned regions. Flame *forward pulsation* and *intermittent contact* will play a significant role in the ignition of unburnt fuels within the flame's reach in wind-driven fires.

### **1.3 Outline of the Dissertation**

In this study, a stationary, non-spreading fire configuration will be used to study wind-driven fire spread as it allows for a thorough statistical analysis of the flame structure and its intermittent behavior. Long-duration experiments provide a large sample size and more control over variations in experimental parameters, such as decoupling the heat-release rate of the fire from flow conditions, unachievable in spreading fires. The flame zone depth in the direction of fire spread can also be carefully adjusted via the size of a burner. Experiments are conducted at laboratory scale, where control of the experiments is more tractable and they can be taken over long times to develop a statistical view of the flame and its movement.

First, total heat flux measurements on a nearly adiabatic surface downstream of a burner are used to correlate the heat flux distribution there for a variety of fire sizes and forced air flow velocities. The data is evaluated versus a local Richardson number to describe how heat fluxes change downstream in both attached and lifted scenarios. Next, a time-dependent view of the extension of the flame is extracted from side-view images with a focus on the flame attachment length. Locations of maximum forward flame pulsation frequency are then related to correlations of mean flame properties. A statistical view of the flame is also presented, dependent on both wind speed and fire size. Finally, the frequency of forward flame pulsations extracted from side-view images of the flame and frequencies of flame-fuel contact measured using a high-frequency heat flux gauge on the surface are measured and analyzed using previous scaling laws.

Using this stationary configuration, the intermittent behavior of the flame, including its motion and heating to the fuel surface will be quantified. These experiments represent a first step toward understanding the behavior of larger (and more complex) spreading wildland fires, providing a framework from which to study the movements of larger fires in the future.

## Chapter 2: Literature Review

### 2.1 Wildland Fire Spread Modeling

In the wildland fire research community, it's well known that there are several factors that control wildland fire spread, namely the fuel, weather, and topography, shown in Figure 2. These three factors are the main forces that have been found to affect wildland fire spread. In the 1970's Rothermel [13] developed a semi-empirical correlation to estimate the forward rate-of-spread (ROS) based on laboratory experiments,

$$ROS_{surface} = \frac{I_R \xi (1 + \phi_w + \phi_s)}{\rho_b \varepsilon Q_{ig}}, \quad (1)$$

where the ROS is the steady, forward rate of spread of a fire,  $I_R$  is the reaction intensity,  $\xi$  the propagating flux ratio,  $\phi_w$  the wind coefficient,  $\phi_s$  the slope coefficient,  $\rho_b$  the oven-dried bulk density,  $\varepsilon$  the effective heating number, and  $Q_{ig}$  the heat of pre-ignition. Essentially, the numerator describes the amount of heat released by the fire ( $I_R$ ) and how much of that is propagated forward to unburned fuels ( $\xi$ ), adjusted by factors for wind and slope. The denominator then describes how much heat is required to ignite unburned fuel.

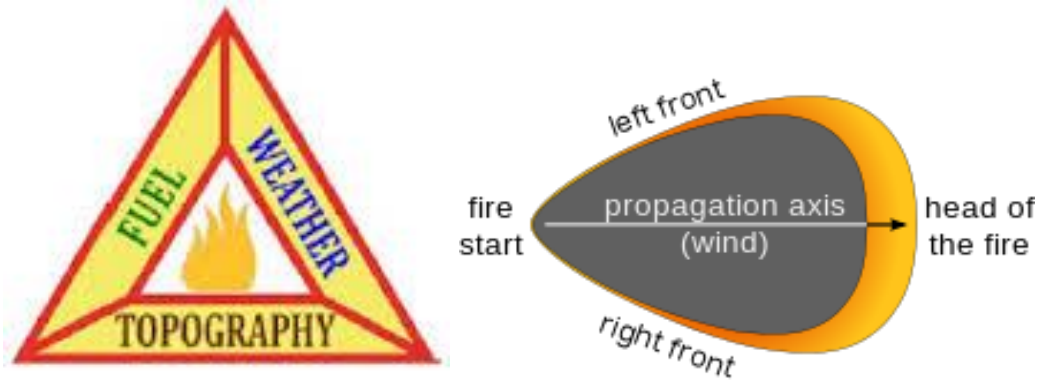


Figure 2. Wildland fire triangle (fuel, weather, and topography) and a representative schematic of fire propagation [14].

While this formulation was a huge leap at the time, it has a number of substantial limitations. The model is not perfect, there are many aspects of wildland fire spread that have not been incorporated into the model. First and foremost, the model is not entirely physically based and relies on correlations at laboratory scale that may or may not scale to large scale. For example, the model assumes that the fuels are uniformly distributed, which is not often the case in real wildland fires spread. The model also treats flame spread to be steady and uniform in one direction only. In reality, fires accelerate and spread laterally (flanking spread) as well, however the model ignores all time-dependent effects including the natural instabilities of the flame and its interactions with the wind. This model was simply a correlation to the observed wildland fire phenomena, and most of the data they used came from lab tests and prescribed burning. What we are trying to do in this dissertation is to further investigate processes which are incorporated into this model, particularly under wind-driven scenarios, so that they can be added into future models for wildland fire spread.

## 2.2 Flame Dynamics

Recent studies of spreading fires in the 3×3 m wind tunnel at the Missoula Fire Science Laboratory have revealed coherent structures that form in the stream-wise direction of the flow as well as span wise fluctuations that propagate to the downstream edge of the flame zone contributing to fuel heating [15], shown in Figure 3. The highly spatially-uniform fuel beds used in these experiments allowed for the observation of these structures with more repeatable results than previous efforts. The results suggest that flame spread in fine fuel beds is driven by non-steady convective heating and intermittent flame contact on fuel particles. These heating characteristics were measured using micro thermocouple arrays and high speed video. The unsteady flame front, however, made it difficult to carefully study these properties, such as a statistical analysis of these features which appear stochastically in the flow. A technique is therefore needed that could study these new instabilities and other general structures of propagating wildfires in a small-scale configuration that can be utilized over long times. Because of the intermittent behavior of wind-driven fires, the average and time-dependent properties of flame, including the heat transfer to the unburnt fuels, flame extension and intermittent pulsation frequencies, will also be affected.

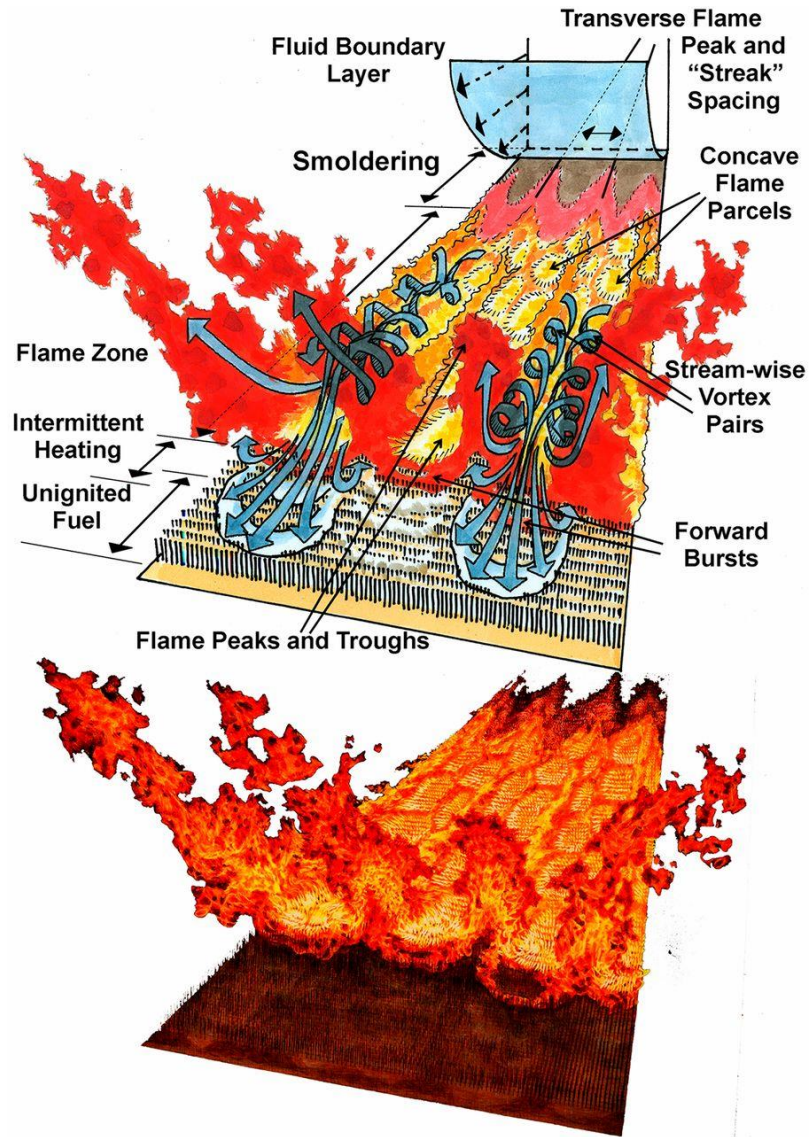


Figure 3. An illustration of flame dynamics and the resulting instabilities from experiments performed by Finney et al. [10] are shown. A number of both stream-wise and span-wise instabilities are shown to form which force flames and hot gases through “troughs” in the flame zone to intermittently heat unburned fuels ahead of the flame front.

Several early studies on flame spread revealed that wind can change the flame shape and thus the flame-fuel interaction significantly, shown in Figure 4 [16-18]. In wind-driven fires, flames tend to be elongated and forced to attach to the fuel bed surface. Flames and the fuel will intermittently interact with each other due to the fluctuating nature of the flame. Compared to conditions under stagnant conditions, heat transfer from the flame to the unburnt fuel in wind-driven fires may change, for example, convection will play an important role as the flame is forced down and intermittently contacting the fuel, thus modifying the heat flux distribution on the downstream surface, which will largely determine the ignition process of the unburnt fuels, changing the spread rate.



Figure 4. Comparison of wind-driven fire behaviors with that under quiescent conditions (from Rothermel [16-18]).

### 2.3 Heat Flux Distribution

The heat flux downstream from a burning fire has often been of interest to fire safety researchers because this heating is known to govern a fire's rate of spread [19]. Formulations [20] describing the rate of flame spread often requires input of the heat flux to unburned fuel ahead of the burning (pyrolysis) region,  $x_p$ , the distribution of this heat

flux (as it may not be constant),  $\dot{q}_f''(x)$ , and the length of this region (nominally the flame height minus the pyrolysis height,  $x_f - x_p$ ). While these features have been somewhat well studied in upward configurations over a vertical wall, where buoyancy and spread occur in the same direction [21-23], little information is available in wind-driven configurations where fire-driven buoyancy and wind-driven momentum compete [24]. These configurations are vitally important to understand the dynamics of spreading wildland fires [25], tunnel fires [26] and mine fires [27]. While some of these configurations occur in a closed (bounded) configuration, e.g., a tunnel, the dynamics of these process are still relatively translatable, except in the regime where the top surface begins to influence the flame. While many studies of flame spread have used a constant value for the heat flux distributed to the surface of the unburnt region [28, 29], more detailed measurements in vertical configurations have shown that this is only a coarse approximation that introduces significant errors. In reality, the heat flux to the unburnt area is often in the form of parabolic or exponentially-decaying profile [30–32].

Spreading fires are difficult to study because the flame moves as a function of time, often accelerating, making it challenging to measure important features such as downstream heat fluxes. Experiments with real fuels are also complicated because external conditions such as ambient winds or slope not only affect the spread rate, but also the burning rate of the fuel, modifying the downstream flame length and heat fluxes. In order to decouple and simplify the problem, a gas burner is often used to represent the pyrolyzing region,  $x_p$ , which then remains stationary with a fixed burning rate over time. This technique has previously been used to study flame spread over fabrics [33] and sloped surfaces [34, 35], however little information is available in the literature for a forced-flow configuration [36].

Certainly, a forced-flow configuration will be more complicated, not only because of a competition between buoyancy and momentum, but also because it is difficult to define the flame length,  $x_f$ , as the flame lifts away from the surface of the fuel, but technically is present. The stationary gas-burner configuration will enable measurements of heat fluxes from the flame to a nearly-adiabatic downstream surface over long times, resulting in averaged profile of the flame behavior and how it would affect flame spread.

Heat fluxes from both spreading and stationary fires in upward [37-39], sloped [40, 41] and forced-flow configurations [42-44] have been measured in the past using various techniques. Because the flame spread process is incredibly complex, most formulations simplify the spatial dependence of the heat flux ahead of  $x_p$  as a constant [45-46] or as a power-law or exponential function of downstream distance [47]. Markstein and de Ris [48] fit this dependence for upward and inclined line burners to simulate flame spread over fabric as a decaying power law function, here represented as

$$\dot{q}_f''(x) = a(x/x_p)^n, \quad (2)$$

where  $x$  is the downstream distance from the upstream edge of the fuel,  $x_p$  is the pyrolysis length and  $a$  and  $n$  are constants fit to the data [48]. In a study by Gollner *et al.*, the exponent  $n$  was found to vary between -2 to -7 for different inclined angles of thermally-thick PMMA [30], but to the best knowledge of the author, no values have been presented in the literature for forced-flow flames.

Heat fluxes to the downstream surface can be divided into two components, convective, and radiative. The energy balance at the surface for a steady burning can be written as [49-51]:

$$\dot{q}_f'' = \dot{q}_{fl,c}'' + \dot{q}_{fl,r}'' - \dot{q}_{s,rr}'' \quad (3)$$

where

$$\dot{q}_{fl,c}'' = k_w \left( \frac{dT}{dy} \right)_{y=0}, \text{ and } \dot{q}_{s,rr}'' = \sigma(T_w^4 - T_\infty^4).$$

Thus

$$\dot{q}_f'' = k_w \left( \frac{dT}{dy} \right)_{y=0} + \dot{q}_{fl,r}'' - \sigma(T_w^4 - T_\infty^4), \quad (4)$$

where  $\dot{q}_{fl,c}''$ ,  $\dot{q}_{fl,r}''$ ,  $\dot{q}_{s,rr}''$  are the convective heat flux received by the surface, radiative heat flux received by the surface and re-radiation heat flux from the surface to the ambient, respectively. The convective heat flux can be approximated close to the fuel surface as

$\dot{q}_{fl,c}'' \approx k_w \left( \frac{dT}{dy} \right)_{y=0}$ , which is the gas phase convective heating assuming the Chilton-

Colburn extension to the Reynolds analogy near the fuel surface [52]. Re-radiation from the surface to the ambient can be evaluated from the wall and ambient temperatures. The total heat flux to the surface can thus be described as the sum of the convective and radiative component of the flame. For small-scale laminar experiments over liquid fuels, it has been reported that the convective heat flux is relatively high, contributing 85% of the total heat flux [52]. While the absolute value of the convective heat flux will eventually reach a relative plateau downstream, radiation will continue to increase as the flame sheet thickens. It has also been observed that the radiative component of the total heat flux will decrease to some degree with an increase in wind speed. As found in the work of Singh et al. [52], the radiative heat flux is 28% and 20% of the total incident heat flux for ambient velocities of 0.79 and 2.06 m/s, respectively for PMMA burning cases, because when the

wind velocity is high, it pushes the flame to attach the board surface and the local temperature gradient is increased, causing the local convective heat flux to increase, too.

The heat flux from the flame to the unburnt fuel surface is closely related to fuel heating and ignition and thus fire spread. The heat flux distribution in vertical wall fires have been studied extensively, however information regarding the heat flux on the downstream surface in a wind-driven fire scenario has not been clearly investigated. This information has strong implication on the wildland fire spread as the heat to the unburnt fuels controls the flame spread.

## **2.4 Flame Pulsations and Movement**

The “puffing” phenomenon of pool fires has been relatively well studied, with a universal scaling law of the frequency of flame pulsations being well correlated with the diameter of the burner. The results from Cetegen [53, 54], Rasbash [55], and Hamins [56] on circular pool fires indicates the pool fire puffing involves a strong coupled interaction between a generated toroidal vortex, formed a short distance above the surface of the fuel, and the perturbations it supplies to the flow field in the vicinity of the flame surface. Experiments have been conducted using circular burners with a wide range of diameters, including both gaseous and liquid fuels. Measurements of fluctuations were performed to study the influence from various parameters to the flame behavior, such as heat release rate effects and disturbances introduced around fires.

Cetegen [54] and Hamins [56] noted that the pool fire puffing frequency,  $f$  is relatively insensitive to the heat release rate of the fire, but is closely related to the diameter of the diameter of the pool,  $D$ , expressed as

$$f \propto D^{-1/2}. \quad (5)$$

Scaling relationships between these quantities have also been proposed, among which the Froude number,

$$Fr = U^2 / gD , \quad (6)$$

which characterizes the inertial force over the gravity force, and the Strouhal number,

$$St = fD/U, \quad (7)$$

which characterizes oscillating flow mechanics or vortex shedding, have been most commonly used [57]. Here,  $U$  represent the characteristic velocity and  $g$  represents the acceleration due to gravity. For pool fires, the characteristic length is often the diameter of the pool and velocity the fuel velocity at the surface, approximated from the burning rate.

Based on Eq. 5, a relationship between  $St$  and  $Fr$  can be formed,

$$St = fD/U \sim \frac{D^{-1/2} * D}{U} = \frac{D^{1/2}}{U} \sim Fr^{-1/2} . \quad (8)$$

Most of the existing literature on pool fire puffing fits both the diameter and St-Fr scaling, however all of these results have investigated fire behavior under stagnant conditions [58-60]. Some results have extended scaling from pool fires to line fires [61, 62], however these have not addressed the puffing phenomena, which has also been observed for wildland fires, over a broad range of scales [63]. For smaller fires, a “flickering” instability at a higher frequency than “puffing” is also formed at the top of small flames [64]. When a fire is influenced by a perpendicular wind, e.g. during a wildland fire, it is easily observed that the wind will also significantly affect the movement of the flame and influence the frequency by which the flame extends forward of the mean flame zone, reaching the unburnt area, but these motions have not been thoroughly described.

More recent studies on stagnant pool fire puffing behavior have also been conducted under various ambient conditions. For instance, Tang and Hu [65] studied puffing from pool fires with different burner sizes and aspect ratios in normal and sub-atmospheric environments. They noticed the puffing frequency will increase with burner aspect ratio, and reaches a relative constant with different ambient pressures. Abe [66] studied the influence of gravity on the puffing frequency, finding that the puffing phenomenon was suppressed under low gravity and that the puffing frequency under low-gravity environments cannot not summarized by previous correlations. His results were summarized by a relationship between the Strouhal-Froude number as  $St=0.577Fr^{-0.502}$ . Different fuel types were also tested in the study of pool-fire puffing behavior [67] and it was noticed that the fuel type does not have much impact on the puffing frequency and puffing intensity.

The intermittent behavior of flames in wind-driven fire spread would certainly differ from puffing under stagnant conditions. Because wind is introduced, perpendicular to the upward movement of the buoyant flow, it will push the flame to move in the span-wise direction, with flame buoyancy pushing the flame upward. Thus, in wind-driven fires, flame pulsations can be divided into two directions, upward, primarily driven by buoyancy, and forward in the wind direction, driven primarily by momentum supplied by the wind. There may of course be many interactions between these two modes, however both are ultimately the outcome of these competing mechanisms and will be studied separately here.

## **2.5 Flame Extension and Flame Attachment**

The geometry of flames under various configurations have been studied extensively, however most research addresses flames under quiescent ambient conditions. Under these stagnant conditions, the flame height is the same as the flame length, often also the most

important length scale in characterizing the geometry of the flame. Thomas found the flame height is well correlated with the burning rate and fire diameter for different fuels [68]. Heskestad [69, 70] later proposed a widely-used correlation for flame height, based on a wide variety of fire sources,

$$\frac{H}{D} = 3.7\dot{Q}^{*2/5} - 1.02, \quad (9)$$

where  $H$  is flame height,  $D$  is fire source diameter, and  $\dot{Q}^*$  is the dimensionless heat release rate, defined as

$$\dot{Q}^* = \frac{\dot{Q}}{\rho_a c_p T_a \sqrt{gD^5}}. \quad (10)$$

Here,  $\dot{Q}$  is the heat release rate of the fire,  $\rho_a$  is the density of ambient air,  $c_p$  the specific heat capacity, and  $T_a$  the temperature of ambient air in Kelvin.

In a wind-driven fire, flames will be tilted toward unburnt fuel to form an angle from the vertical. The flame will also be “stretched”, and grow longer along the surface. A reduction in the overall length may also occur due to better mixing with air, especially at higher velocities. The flame extension or flame drag behavior by the wind has not been investigated thoroughly. Hu et al [71] studied the flame extension behavior of circular pool fires under wind, considering air mixing, and developed a correlation to predict the flame extension length,

$$\frac{\ell_f}{D} = 3.7\dot{Q}^{*2/5} - 1.02 + 2.48\left(\frac{u}{\sqrt{gd}} \cdot \frac{s\Delta H_C}{M_{fuel}\Delta H_{fg}} \cdot \frac{M_{O_2}}{\rho_a Y_{O_2,\infty}}\right), \quad (11)$$

where  $\ell_f$  is the flame extension length,  $u$  is the wind speed,  $D$  is the pool diameter,  $s$  is the molar stoichiometric oxygen to fuel ratio,  $\Delta H_C$  is the heat of combustion of the fuel,

$M_{fuel}$  and  $M_{O_2}$  is the molecular weight of the fuel and oxygen,  $\Delta H_{fg}$  is the effective heat of evaporation,  $\rho_a$  is the air density, and  $Y_{O_2,\infty}$  is the oxygen mass percentage concentration in ambient air. Here, the flame extension length in wind-driven fire cases has been shown to not only be a function of heat-release rate, but also wind velocity, fuel type and the rate of mixing with air.

In a wildland fire scenario, the flame length has been shown to have a strong relationship with the fire spread rate since it provides information on the potential distance the flame can convectively heat unburned fuels (a forward heating length), although this relationship is much more complex than the simple relationship presented by Byram [72]. In wildland fire spread the flame attachment length on the downstream surface, or the flame drag length [73, 74] is important in determining this forward heating length. This phenomenon has been observed for a long time. Several equations based on laboratory pool fire experiments have been proposed to describe this phenomenon. Wellker and Sliepcevich [75] correlated the flame attachment length against the Froude number of the wind ( $Fr_w$ ),

$$\frac{D + \Delta D}{D} = 2.1 Fr_w^{0.21} \left( \frac{\rho_v}{\rho_a} \right)^{0.48}, \quad (12)$$

where  $\rho_v$ ,  $\rho_a$  are the density of fuel vapor at the boiling point and ambient air respectively,  $D$  is the diameter of the pool, and  $\Delta D$  is the flame attachment length on the surface. Raj [76] further proposed

$$\frac{\Delta D}{D} = 2.375 Fr_w^{0.5} \left( \frac{\rho_v}{\rho_a} - 1 \right)^{0.5}, \quad (13)$$

based on a combination of data from Welker [75] and Raj [76] to predict the attachment length in a wind-driven fire.

Flame attachment along a downstream surface has also been observed during spreading fires, such as the study by Apte et al. [77] which investigated large-scale wind-driven fire spread over a larger thermally-thick slab of polymethyl methacrylate (PMMA) in a mine tunnel. The flame and, therefore, attachment was generally divided into regimes of attached, boundary-layer like flame spread and lifted, plume-like behavior where the flame was lifted and tilted some angle from the surface of the fuel. These distinctive regions are formed due to the competing mechanisms of momentum from the wind and buoyancy from the flame. In this study, we will also define an intermittent attached region which occurs between the attached and lifted regions.

## **2.6 Summary**

Based on the literature review, intermittent flame behavior in wind-driven fires is not yet well understood. While heat flux distributions have been well-studied in a vertical wall configuration, little information is available when the flame is driven by wind. Some information on flame shapes, including the flame height and flame length under stagnant and some wind-driven conditions have been studied, however there is much left to be understood. This information will be important to develop a physical model of wind-driven wildland fire spread.

## **Chapter 3: Experimental Facility and Instrumentation**

A wind tunnel apparatus was used, which mainly includes a blower, gas burner, and a test section. A description of the apparatus, instrumentation and experimental procedures are provided below.

### **3.1 Wind Tunnel Setup**

A specially-designed wind tunnel was used at the University of Maryland to conduct forced-flow fire experiments. The structure and dimensions of this lab-scale tunnel can be seen in Figs. 5 and 6 [12, 52, 78-81]. Revisions were made to the wind tunnel to facilitate our measurements. At one end of the tunnel, a  $100 \times 75 \times 100$  cm plenum with an EBM blower (G3G250-MW72-01) with a maximum flow rate of 1200 cfm was connected to pressurize the plenum. A pulse-width modulation controller allowed for precise control of the wind blowing without generating significant perturbations to the air flow. The pressurized air then travels through a  $30.48 \times 30.48 \times 122$  cm straight tunnel before reaching the test section. A set of fine turbulence reduction screens and 5 cm thick honeycombs with 0.3 cm diameter holes were built and installed within the tunnel. The final piece of the wind tunnel setup is the exhaust duct (tunnel), from which the uniform and steady wind travels and provide wind to the test section.



Figure 5. Photo of the wind tunnel apparatus

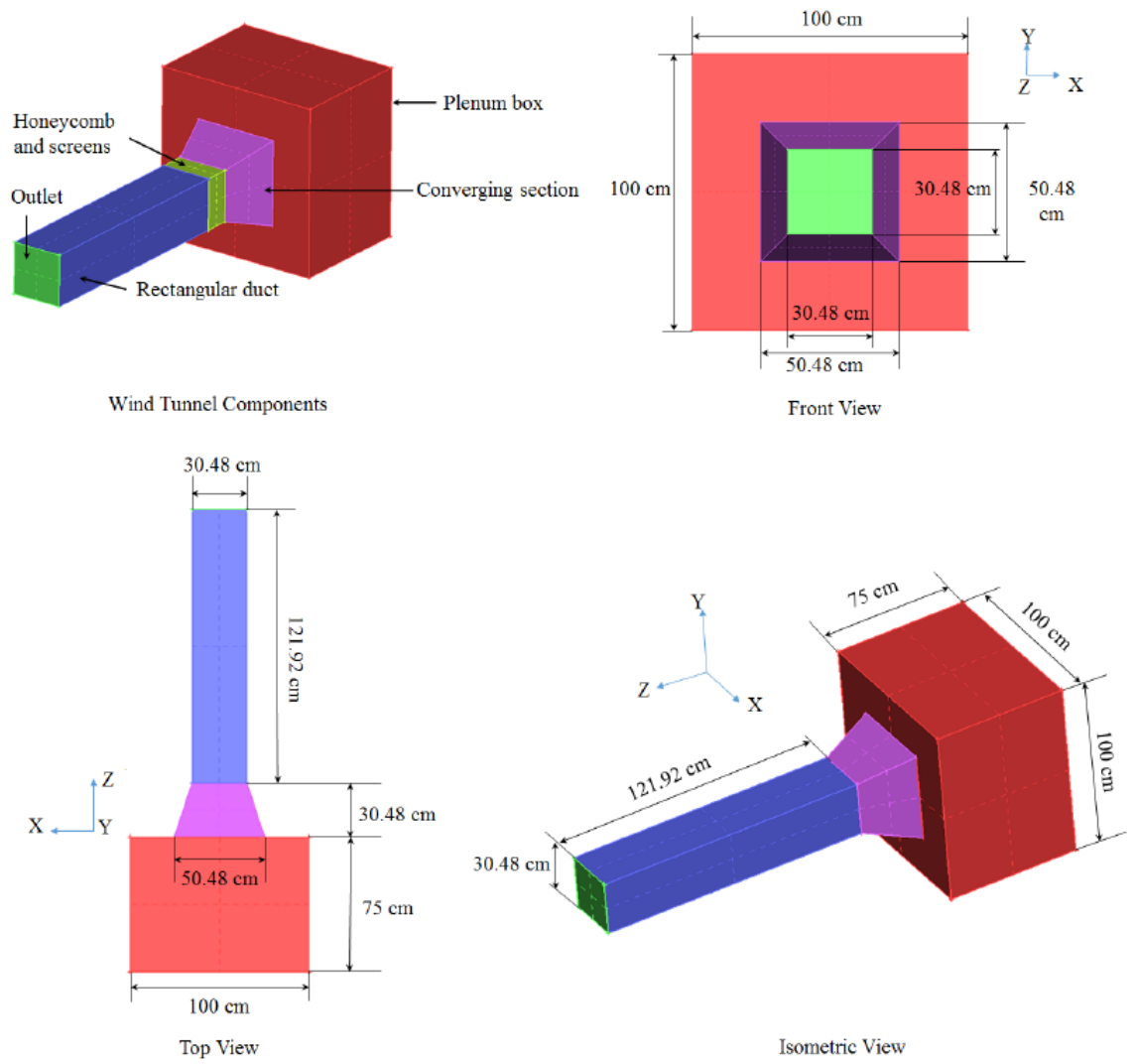


Figure 6. Schematic including dimensions of the wind tunnel [52]

### **3.2 Gas Burner**

Two gas burners, previously designed and built by Gorham [12] and Singh [52], were used to simulate wind-driven fires. The 6.5 cm tall burners were  $25 \times 5 \text{ cm}^2$  and  $25 \times 10 \text{ cm}^2$  wide, built with thick galvanized steel. They were built with a 2 cm tall plenum and had 4.5 cm of fine sand placed on top of a fine mesh to distribute the fuel. Propane gas enters the sand burner through 0.6 cm diameter NPT bulkhead fitting on the bottom side of the burner plenum. The fire size of the tests can be controlled by the mass flow rate of the propane, controlled using an Alicat MCR-100SLPM-D mass flow controller. The fire sizes of the tests ranged from about 3 to 15 kW.

### **3.3 Velocity Characterization**

The ambient wind velocity coming out the tunnel was measured using a Dantec Dynamics hot-wire anemometer system. The hot-wire anemometer used here can be seen in Fig. 7. Note that the single-direction hot-wire anemometer is fragile, records at high frequency, and is very sensitive to ambient conditions. Extra care needs to be taken when making the measurement using this device. The maximum sampling frequency of the hot-wire anemometer is 1000 Hz, and the maximum ambient temperature it can withstand is 150 C. Before performing experiments the hot-wire anemometer is calibrated in a controlled Poiseuille flow against a known hand-carry anemometer, with the wind speed during calibration ranging from 0 to about 3 m/s, which covers the wind speed range that was used during experiments.

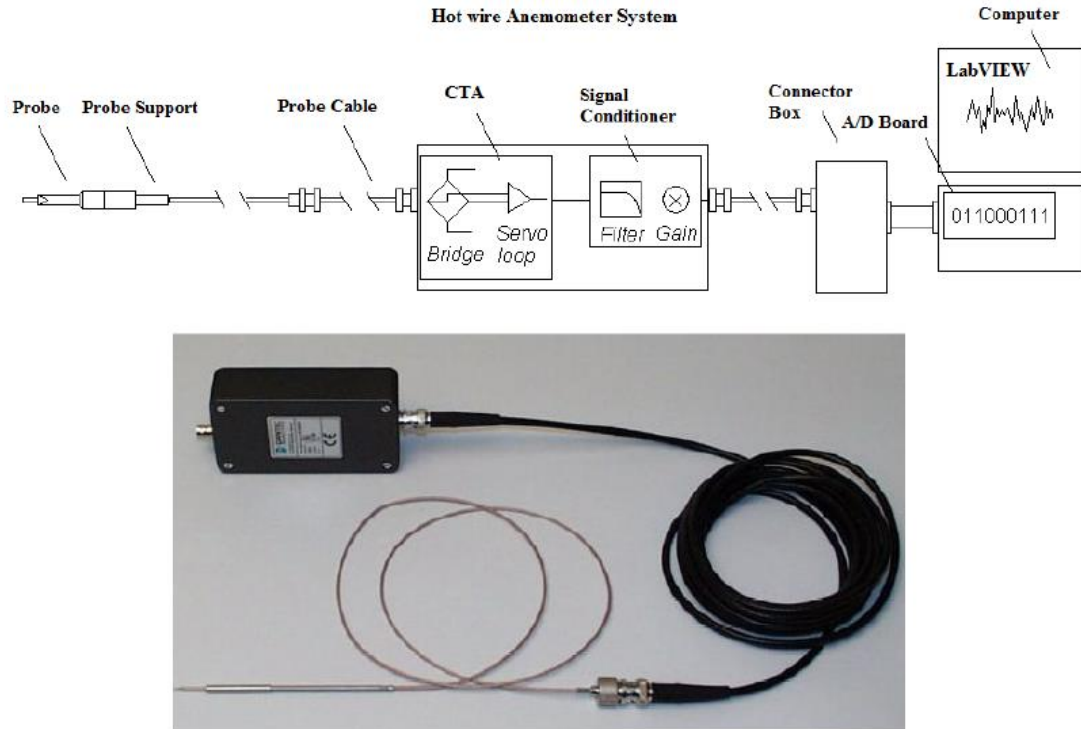


Figure 7. Hot wire anemometer used in his study [82].

The ambient wind velocity in our experiments ranged from about 0.5 to 2.5 m/s. The velocity profile and corresponding turbulence intensities of the wind (ratio of the root-mean-square of the deviation of the wind velocity to the mean velocity) were characterized and checked every time in the ambient flow before taking experimental measurements.

Two ambient velocity conditions were characterized for these experiments, a low wind speed at 1.12 m/s, and a high wind speed at 2.15 m/s. The measurement locations used are shown in Fig. 7. For each of the two wind conditions characterized, 5 different downstream locations were measured, starting from the leading edge of the metal sheet, where the incoming wind flow first reaches the test surface, which is labelled as 0 cm in Fig. 8, and then 4 more vertical lines were taken every 10 cm along the downstream surface. At each measurement location, measurements were taken along a vertical line, starting from 2 mm

above the surface, at an interval of 0.5 mm up to 20 mm above the surface. At each measurement location, data were taken for 30 seconds and the averaged velocity was calculated. The velocity data are shown in Figs. 9 and 10. The bulk velocity can be estimated from the two figures above the boundary layer thickness. The data shows that the ambient velocity is very uniform and steady above the boundary layer thickness.

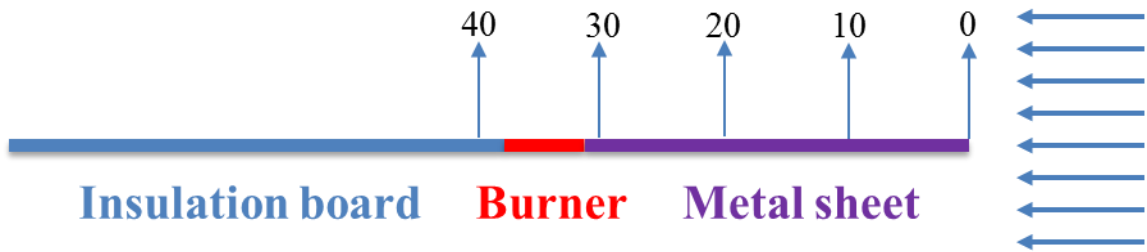


Figure 8. Measurement locations for wind profile measurements.

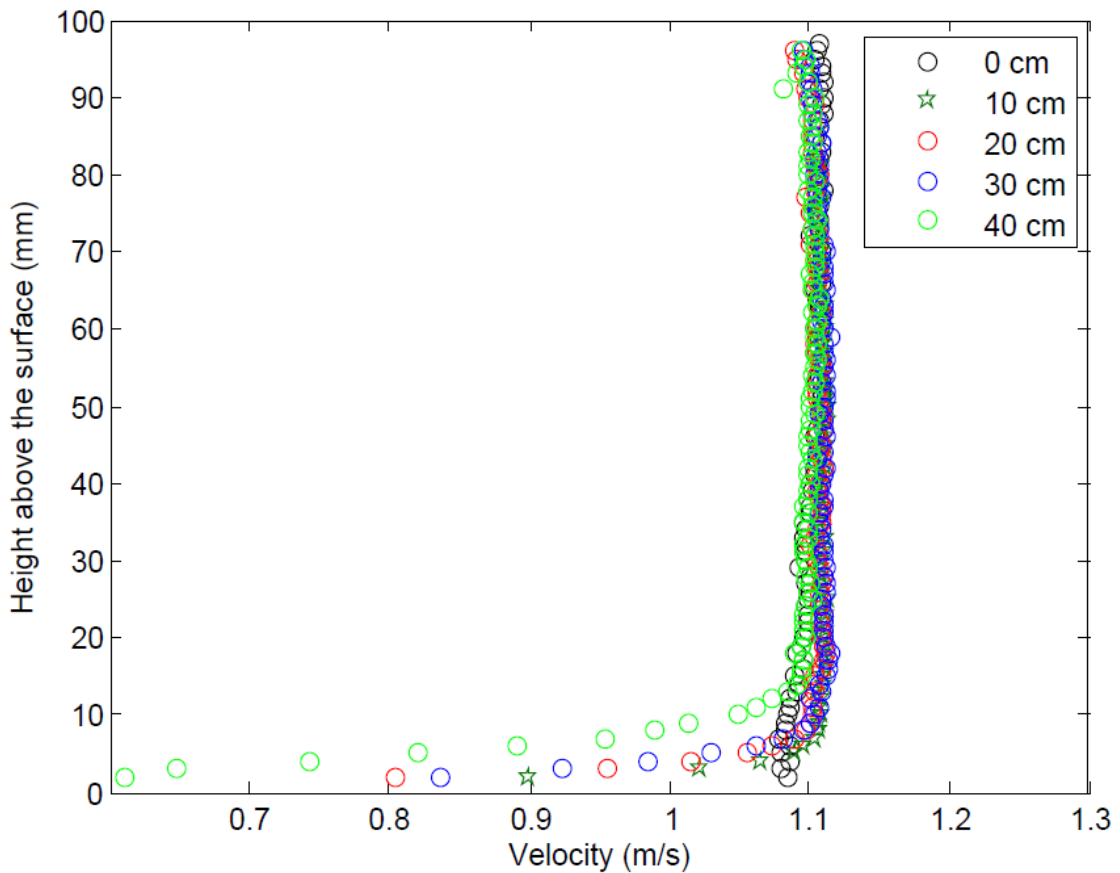


Figure 9. Low velocity (1.12 m/s) profile with height over the surface.

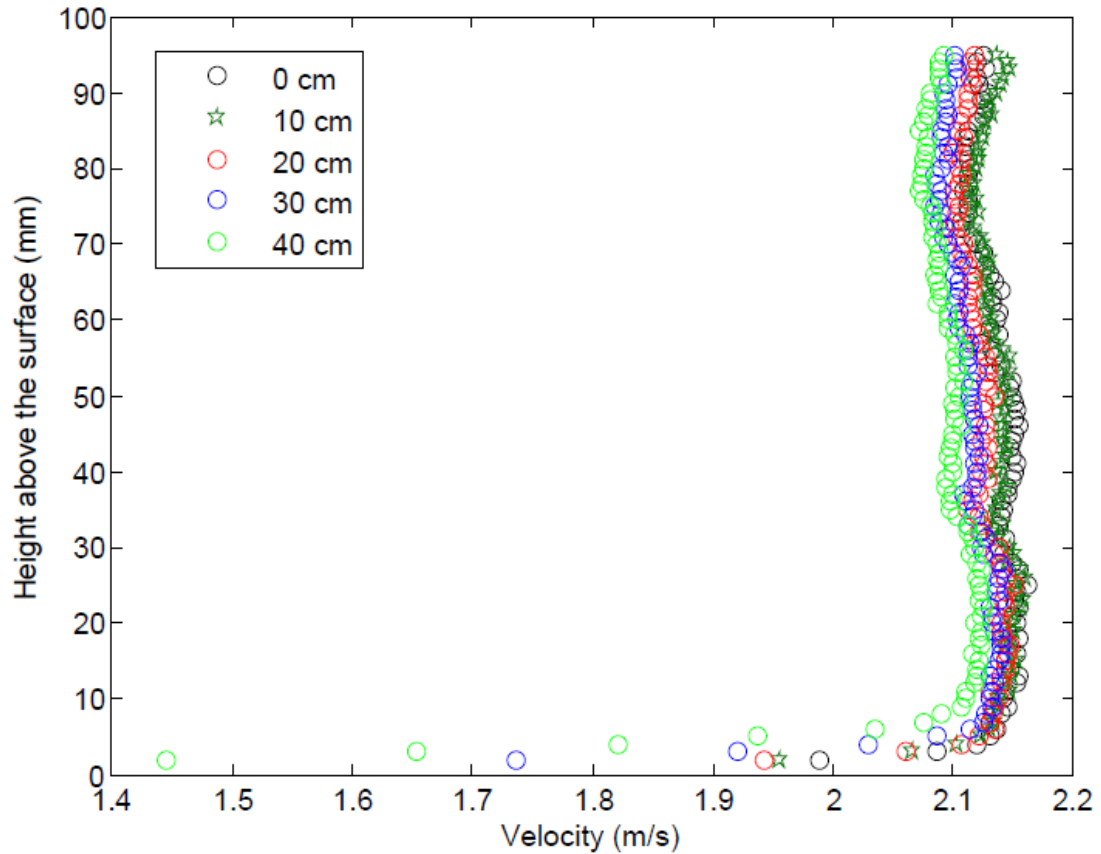


Figure 10. High velocity (2.15 m/s) profile with height over the surface.

The turbulence intensity of the ambient flow was also recorded to provide more information on ambient boundary conditions. Figures 11 and 12 show the turbulence intensity for the two wind velocities mentioned above, measured at different downstream locations along a vertical line above the board surface. It can be seen that, for the most part, the turbulence intensity is well controlled below 2%, with several points approaching as high as 5%, where these locations are close to the board surface and surface roughness within the boundary layer makes the turbulence intensity increase. It is also found that, when the wind velocity is high, the turbulence intensity increases a little bit higher than the low velocity ones, but the wind profile remains very uniform and the turbulence intensity

very low in the central core of the tunnel exit, which provides a steady wind profile for our experiments, shown in Figs. 11 and 12.

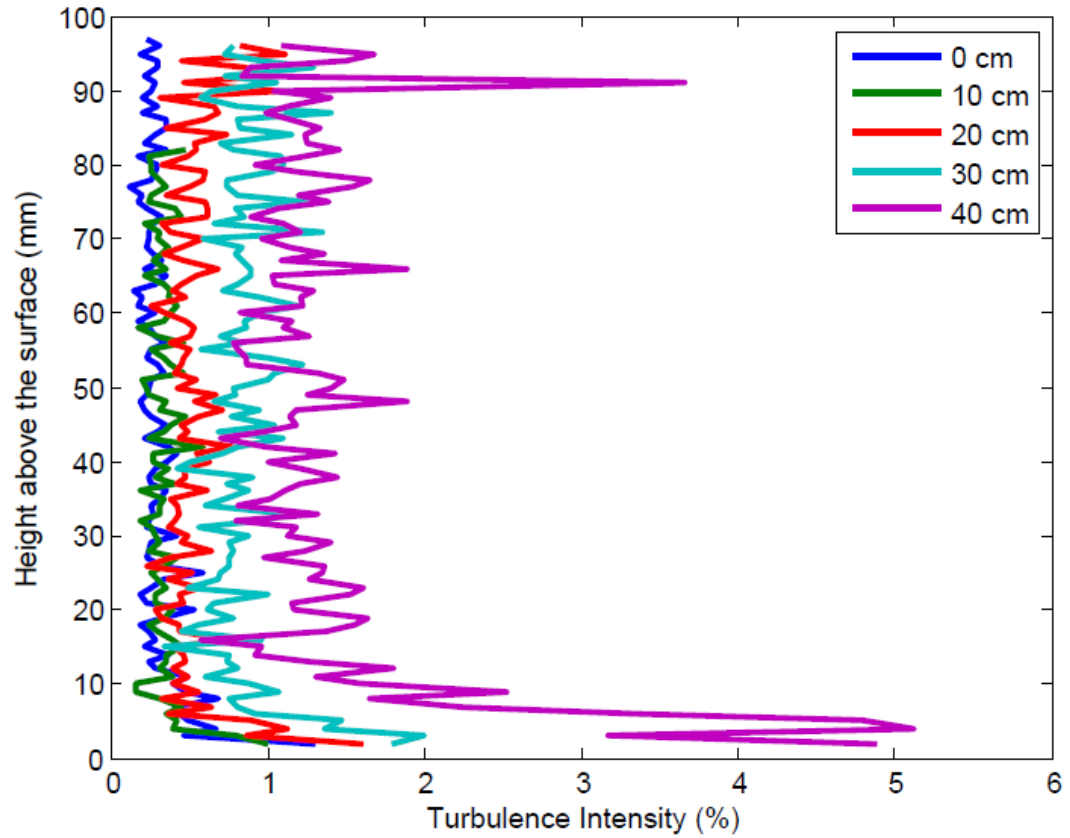


Figure 11. Turbulence intensity profile with height and downstream distance over the surface (1.12 m/s, low wind case).

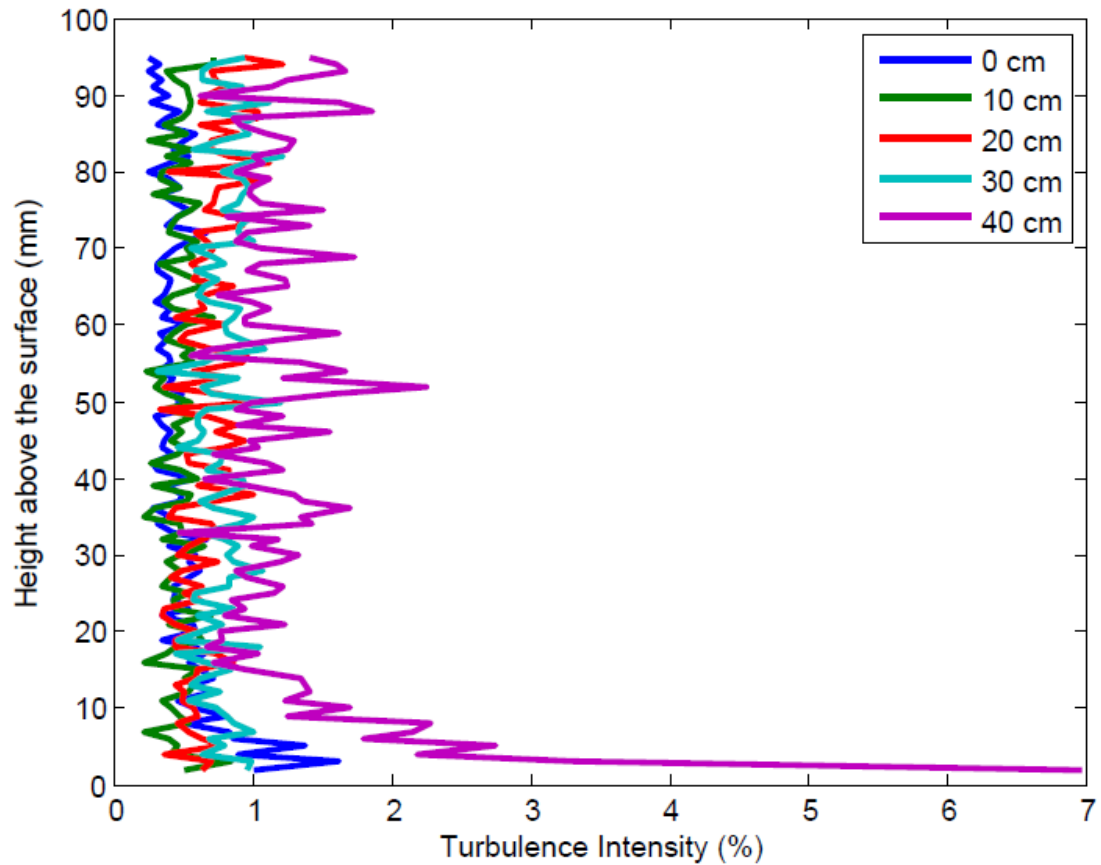


Figure 12. Turbulence intensity profile with height and downstream distance over the surface (2.15 m/s, high wind case).

### 3.4 Temperature Measurements and Traverse System

R-type thermocouples with Pt/Pt-13% Rh are used here for temperature measurement. Two wire diameters, 50 and 75  $\mu\text{m}$ , with bead diameters 100 and 150  $\mu\text{m}$ , respectively are used [83]. The small diameters of the R-type thermocouples made high-resolution measurements possible. Also, disturbances to the flame and the radiation loss correction from the thermocouple bead are minimized. A schematic figure of the thermocouple used, including a connector, ceramic tube and thermocouple bead are shown in Fig. 13. In our

tests, to apply a radiation correction to our temperature data, both 50 and 75  $\mu\text{m}$  diameter thermocouples were used. A transverse system was also used to obtain accurate positioning and incremental movement of the thermocouples. Two computer-controlled Velmex X-Y unislides allowed the thermocouple to move in two directions with a maximum spatial resolution of 1.5  $\mu\text{m}$ .

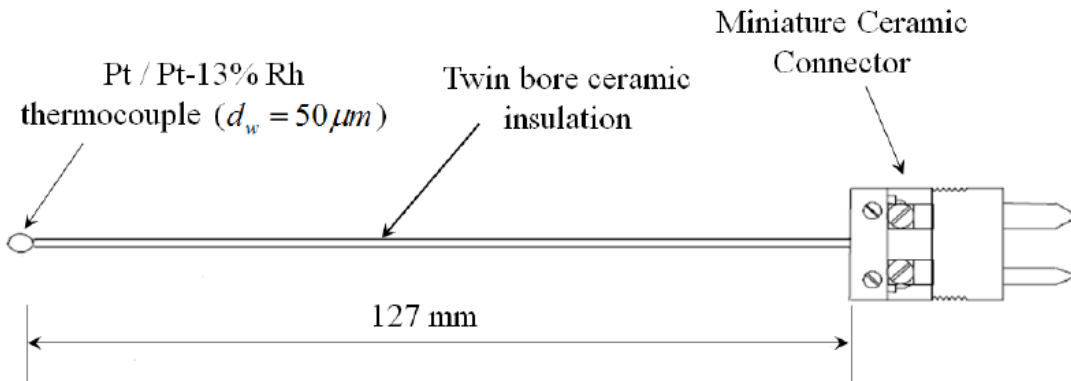


Figure 13. Thermocouple and mount used in temperature measurements [83].

### 3.5 Total Heat Flux Gauge

A Vatell water-cooled total heat flux gauge [84] (model HFM1000-0) was used in our tests to measure the total heat flux distribution on the downstream surface of wind-driven line fires. Before taking measurements, the heat flux gauge was calibrated against a NIST-traceable Medtherm incident heat flux sensor in the cone calorimeter. The result of the calibration can be seen in Fig. 15. An amplifier was also used to process the data output before being recorded by the data acquisition system. The total uncertainty for a single heat flux sample acquired with this water-cooled heat flux gauge is found to be less than 3%. The fitting equation for calibration between the heat flux and the voltage output gives an adjusted  $R^2$  higher than 99.99%. Additional product details are shown in Table 1.



Figure 14. The Vatell total heat flux gauge and amplifier used in experiments [84].

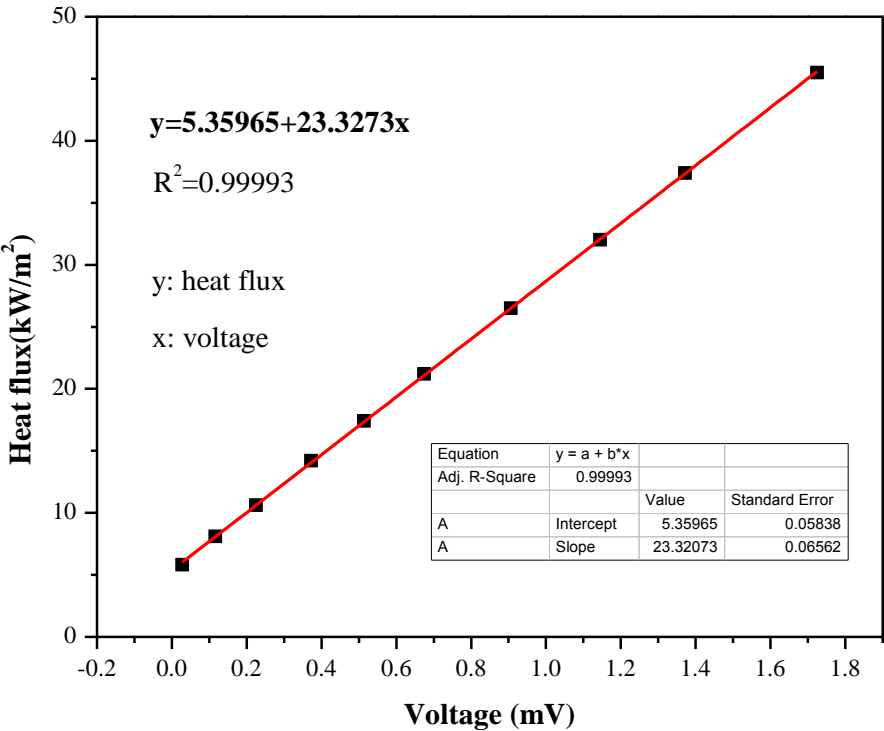


Figure 15. The calibration used for the Vatell total heat flux gauge in the cone calorimeter.

Table 1. Vatel heat flux gauge specifications from the manufacturer [84].

Product details	Vatell HFM 1000-0
Output signal	Linear output
Sensor coating	Pyromark 1200, 0.95 emissivity
Repeatability	0.5%
Resistance (at 24°C)	3690 ohm

### 3.6 Radiometer

In order to measure radiation from the flame to the downstream surface, a water-cooled Medtherm Schimdt-Boelter radiometer (model NO. 64O-10SB-22) was used [85]. The radiometer was pre-calibrated with a water temperature at 29.4°C, with a 3% uncertainty, about 95% confidence level. Calibration was performed in compliance with ISO/IEC 17025, ANSI/NCSL Z540-1 and MIL-STD-45662A to Medtherm PI-20 with traceability to the National Institute of Standards and Technology. A sapphire purge window was also used to avoid soot from the flame clouding on the radiometer surface. The full-scale output level was 9.59 mV at 100 kW/m<sup>2</sup> with responsivity 0.0959 mV per kW/m<sup>2</sup>. The maximum non-linearity of the gauge is about 2% of the full range, and repeatability within 0.5%. A schematic of the radiometer sensor is shown in Fig. 16. The diameter of the sensor 2.5 cm with sapphire window installed on top. The standard window is at 150° view angle. Two water tubes, each with diameter 0.32 cm were connected to the sensor to provide cooling effect to the gauge when working with heat sources. A 0.32 cm diameter gas purge tube was also connected to the gauge to blow nitrogen along the sensor surface.

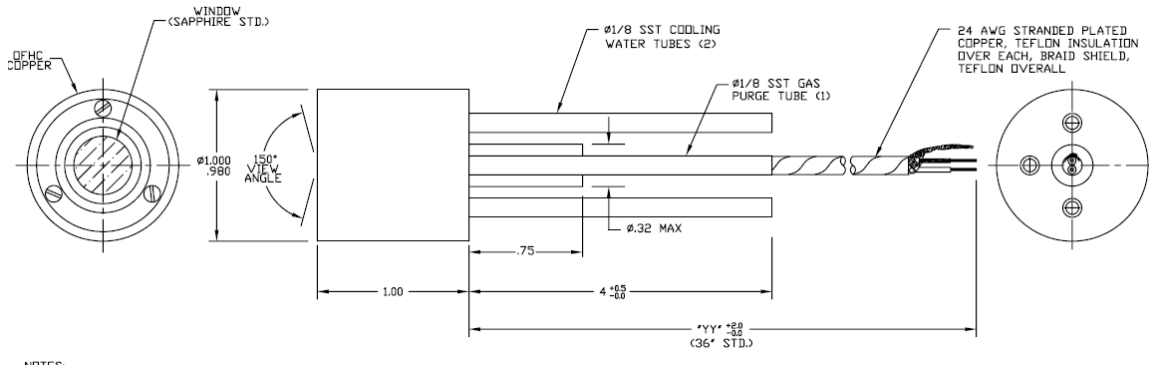


Figure 16. Schematic of the Medtherm radiometer used from the manufacturer [85].

### 3.7 Digital Camera

A Nikon D7000 digital SLR camera (4,928 × 3,264 pixels) was used to capture flame side-view images during tests. A MATLAB program is then used to process the images to obtain an averaged image. The camera was set up to perpendicular to the side of the test section in order to capture the whole flame. Averaged flame images are determined by a 50% light intensity threshold, and the flame attachment length on the downstream surface is determined based on the distance between the flame and the downstream surface.

### 3.8 Data Acquisition Systems

A Compact DAQ USB chassis with C-series I/O modules from National Instruments were used in tests for velocity, temperature, and heat flux measurement input and output. For temperature measurements, the voltage signal from the thermocouple was acquired, conditional and digitized through a NI-9214, which is a 24-bit high density 16-channel thermocouple input module with a 0.02°C measurement sensitivity. A built-in cold-junction compensation circuit is provided in the NI 9214. In addition to the cold-junction compensation system, the NI 9214 also has an extra, internal-only channel known as the

auto-zero channel, from which an offset error can further be eliminated to provide more accurate measurements.

The NI 9214 module is used for thermocouple and heat flux measurements, however, for hot wire wind velocity measurements at high frequencies, an NI 9239 module needs to be implemented, which is 4-channel, 24-bit C Series analog input module and comes with a channel-to-channel isolation and built-in signal conditioner. Figure 17 shows a view of the NI-cDAQ 9178, NI 9124, and NI 9239 C-series modules.

LabVIEW is used for continuous data acquisition, with different scripts prepared for temperature, velocity, and heat flux measurements. The scripts also provide readings of the data, such as maximum value, minimum value, mean value, standard deviations, and turbulence intensity.

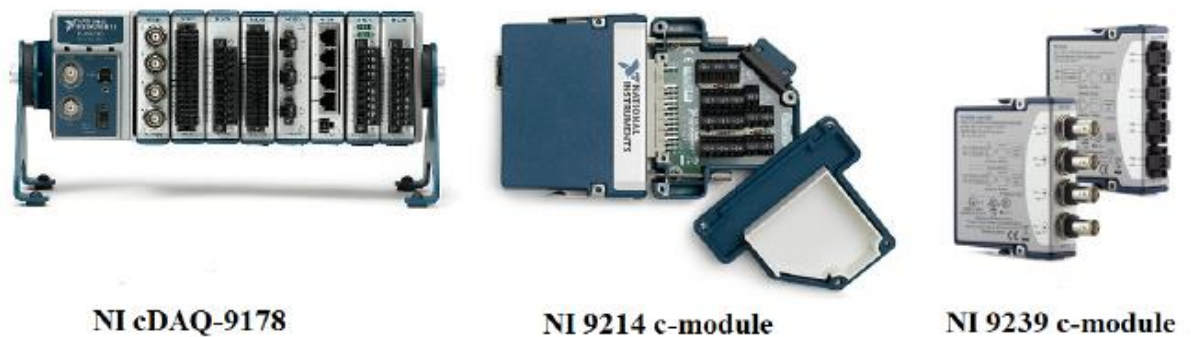


Figure 17. National Instrument data acquisition systems used in the study [86].

### 3.9 Experimental Conditions

Tests were conducted in the large fire lab at the University of Maryland to study the heat flux and temperature distribution of wind-driven line fires. For heat flux measurements, the water-cooled Vatell heat flux gauge was used, with a measurement range from 0-100 kW/m<sup>2</sup> and a response time of 1 kHz. A ceramic fiber insulation board (Superwool board

pre-painted with matte black high temperature paint) with dimensions of  $45 \times 90 \times 2.5 \text{ cm}^3$  was used to hold the gas burner and provide a surface over which to take measurements. The heat flux gauge was inserted into pre-drilled holes and kept flush with the surrounding insulation board to measure the total heat flux received by the surface downstream of the burner. The heat flux gauge was calibrated against a known incident heat flux gauge, with calibration results showing a measured uncertainty less than  $\pm 3\%$ . Heat fluxes were averaged over 200 s for each test point. The spacing between adjacent holes on the insulation board for the heat flux gauge was 5.5 cm measuring up to 33 cm downstream. The first measurement point could only start as close as 5.5 cm away from the trailing edge of the burner due to the configuration of the burner and gauge water-cooling system. Each heat flux test was repeated three times and an averaged value is taken as the final measurement data. The wind velocity in the experiments ranged from about 0.5 m/s to 2.5 m/s. Three different fire heat release rates, 4, 5 and 6 liter per minute (lpm) of propane gas flow were employed for the experiments, corresponding to 6.3, 7.9 and 9.5 kW fire sizes. A schematic of the test section is shown in Fig. 18.

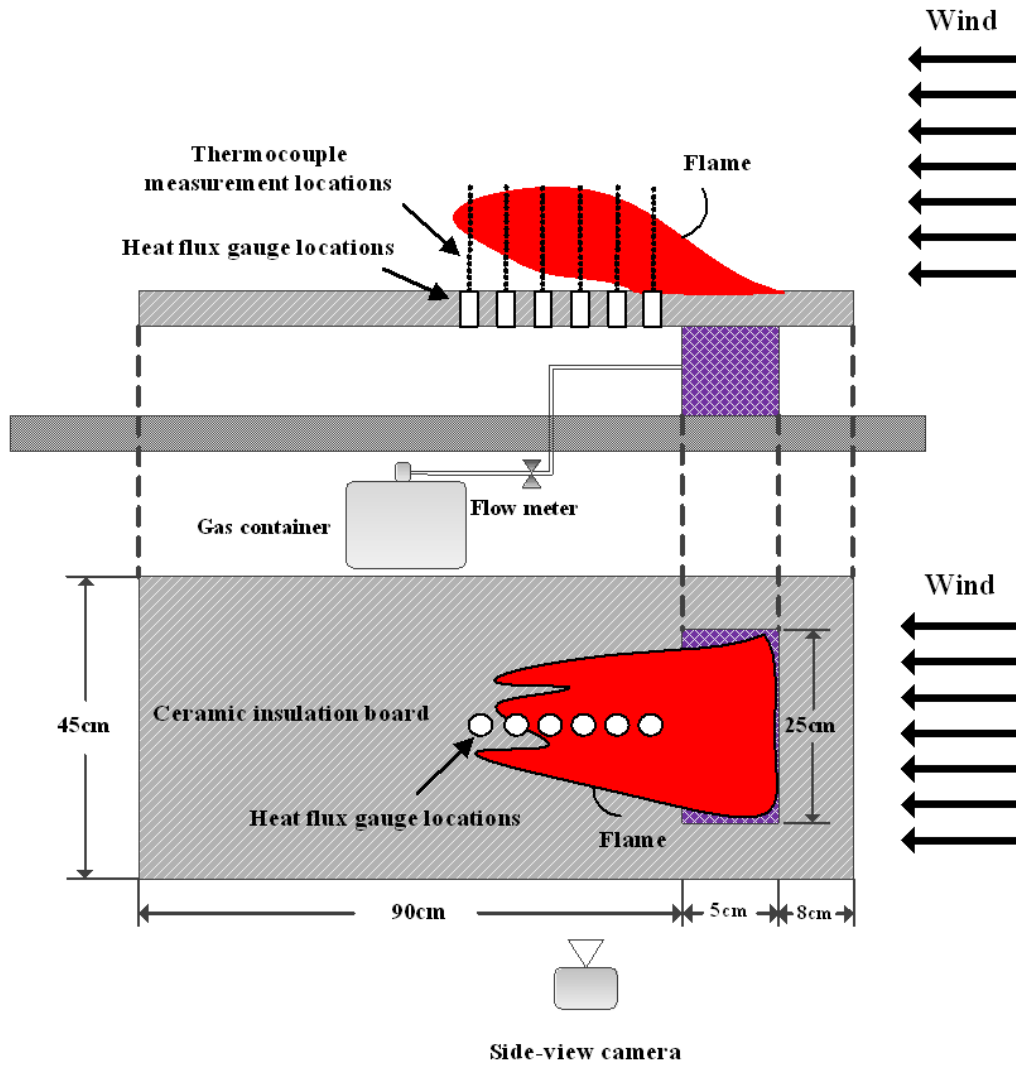


Figure 18. Experimental setup downstream of the tunnel outlet.

Local flame temperatures were also measured using R-type thermocouples traversed via an X-Y unislide from the surface of the heat flux gauge to the thermal boundary layer above the flame. The first measurement point in one vertical line is the insulation board surface, measuring vertically above that at 1 mm intervals. In one vertical direction line, there are nearly 20 measuring points, up to the flame height. Voltage signals from the thermocouples were acquired, conditioned and digitized through a National Instruments NI 9214, averaged

at each point for 60 s. All tests were repeated 3 times to ensure repeatability. Table 2 shows the experimental conditions used.

Table 2. Experimental conditions (I)

Fire size (kW)	Wind velocity (m/s)	Downstream heat flux locations (cm)	Thermocouple locations above the surface (mm)
	0.87	5.5	0
	1.14	11	2
6.3	1.37	16.5	4
7.9	1.62	22	6
9.5	1.91	27.5	8
	2.14	33	...
	2.45		20

A side-view camera was also used to capture flame images. Pictures are averaged, a threshold applied to distinguish flame vs. no flame and the flame attachment length on the downstream surface determined as the distance between the burner trailing edge to the location where the distance between the flame and the surface reaches 5 mm using a custom MATLAB script was used, applying different thresholds (1, 2, 4, 6 mm) to test the validity of the method. No variations of the trend were observed, though the absolute values shift slightly.

In another set of experiments, different burner geometries, wind velocities and fire heat release rates were used to study fluctuations of the flame with wind. The experimental setup was very similar to Fig. 18 but without the heat flux gauge and thermocouple measurements. The main methodology used there was image analysis. High-speed

videography was used to capture digital images of the flame in all configurations from a side view. The camera used was high-speed Casio EFX-1, recording at 120 frames per second with a 640×480 pixel resolution. The experimental conditions are listed in Table 3.

Table 3. Experimental conditions (II)

Burner dimensions (cm <sup>2</sup> )	Heat-release rate (kW)	Free-stream wind velocity (m/s)
25×5	2.38	1.11, 1.39, 1.61, 1.89, 2.11, 2.36
	3.21	1.11, 1.39, 1.61, 1.89, 2.11, 2.36
	4.96	1.39, 1.61, 1.89, 2.11, 2.36, 2.55, 2.65, 2.75
	6.86	1.61, 1.89, 2.11, 2.36
25×10	4.87	0.95, 1.09, 1.45, 1.78, 1.59, 2.06
	7.30	0.95, 1.09, 1.45, 1.78, 1.59, 2.06
30×25	4.38	0.223, 0.447, 0.67, 0.894, 1.11
	6.32	0.223, 0.447, 0.67, 0.894, 1.11, 1.34
	8.76	0.223, 0.447, 0.894, 1.11, 1.34

## Chapter 4: Heat Flux Analysis

### 4.1 Total Heat Flux Distribution

In this chapter, the total heat flux distribution obtained under different fire and wind conditions are presented and correlated against a parameter representing the influence of fire-induced buoyancy and wind-driven momentum. The parameter, namely the local Richardson number ( $Ri_x$ ), is proposed to scale with heat flux data. A piece-wise function of the non-dimensional heat flux versus the local  $Ri_x$  can then be used to predict the heat flux in wind-driven fires. Some future work to be done in this area is also discussed.

Figure 19 shows heat flux data collected at the same point (11 cm downstream surface) averaged for 150 s for 4 different sets of experiments, with 2 two fire sizes, 6.3 kW and 9.5 kW, and 2 wind velocities, 1.14 m/s and 1.62 m/s. The average data will be used in later analysis. It is clear that, when the wind velocity is high, the heat flux is quite stable with few fluctuations, while on the other hand, the heat flux data varies more with a low wind velocity. It is speculated that, when the wind speed is high, most of the flame is forced to attach to the surface, and the heat flux gauge is fully covered within the stable flame region, thus the heat flux data received is reflecting the stable flame movement. When the wind speed is low, only a small portion of the flame is attached to the surface, and heat flux gauge is within the unstable flame region, thus the data fluctuates a bit more.

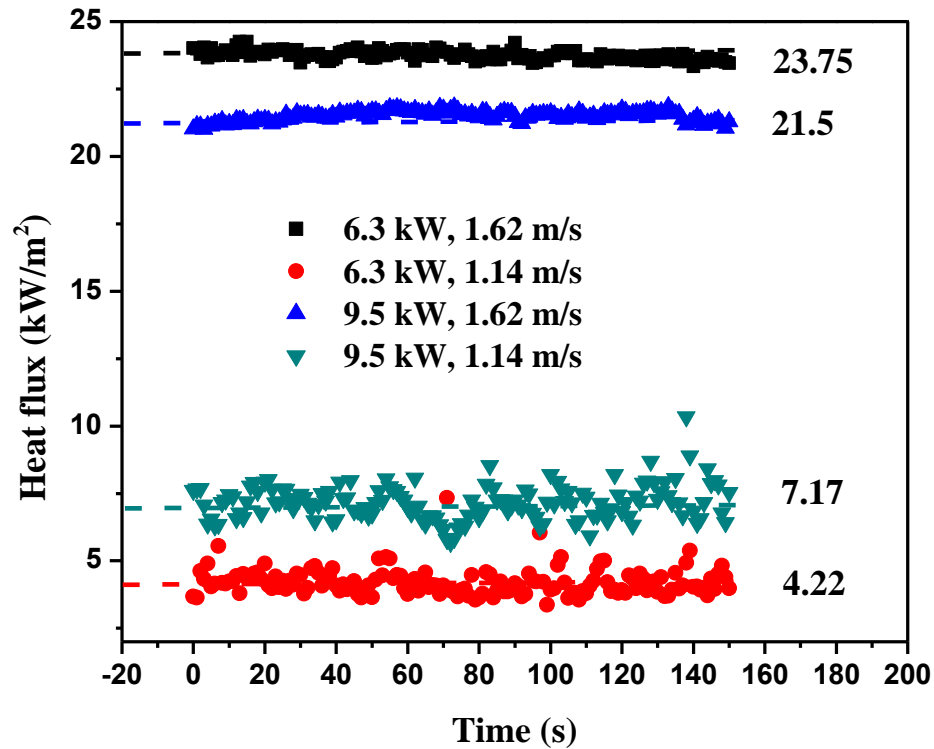


Figure 19. Heat flux data taken on 11 cm downstream averaged for 6.3 kW, 9.5 kW fire size, 1.14 m/s, 1.62 m/s wind speed scenarios for a period of 150 s.

In order to quantify the total heat flux in a somewhat universal manner, the local distance where each heat flux was measured was first normalized [87, 88]. The distance along the downstream surface from the trailing edge of the burner is denoted here as  $L$ , which is normalized by dividing by the burner hydraulic diameter,  $D_H$ , which for a rectangular burner, is defined as four times the area over the perimeter [89],

$$L^* = L / D_H \quad (14)$$

$$D_H = 4S / P \quad (15)$$

Here,  $S$  is the area of the burner,  $P$  is the perimeter, and  $L^*$  is the non-dimensional downstream distance.

A significant difference was observed between the heat flux distribution profiles of the high and low wind velocities. For low velocities, buoyancy dominates the flame shape and only a small portion of the flame was observed to attach to the surface ahead of the burner. Because the nearest heat flux gauge is located 5.5 cm from the burner edge, the peak heat flux, which we later show occurs at this transition point, is not picked up, instead only resolving the downstream decaying heat flux profile in the thermal plume, where the flame has already lifted off from the surface. This is seen in Fig. 20, where the heat flux decays from approximately 10 kW/m<sup>2</sup> to 0, following a power-law decay like Eq. 2.

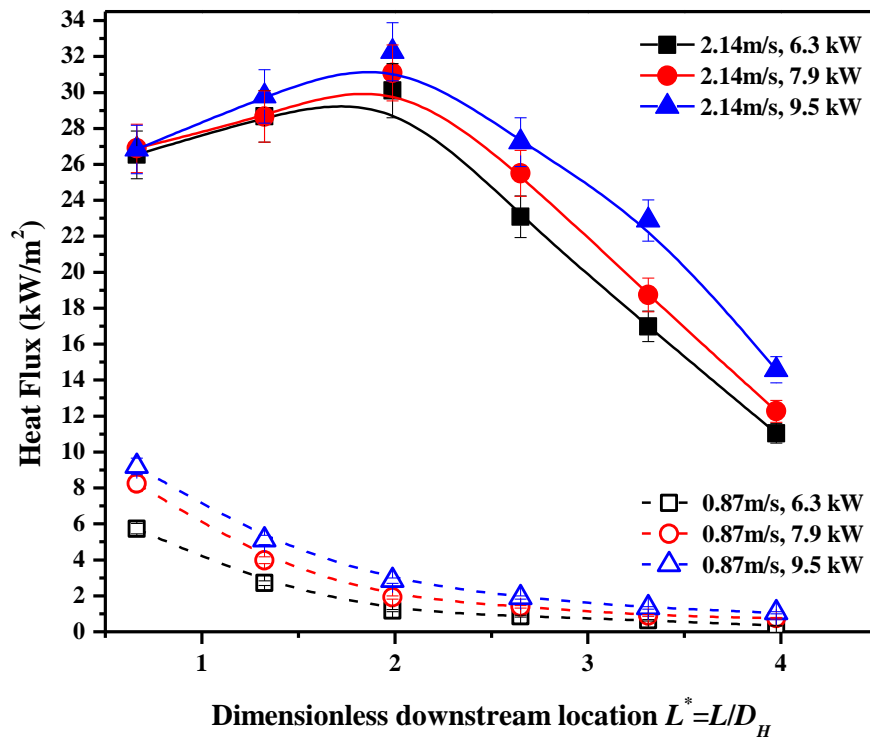


Figure 20. Comparison of heat flux profiles for different wind velocities and fire sizes.

On the other hand, when the wind velocity is high enough, the flame starts to transition from a buoyancy-dominated to a momentum-dominated regime, remaining attached to the downstream surface for considerably longer distances. This momentum-dominated regime can also be seen in Fig. 21, where the heat flux to the downstream surface first increases to a peak value, then decreases with downstream distance. This makes sense for these smaller, convectively-dominated flames, where the location of closest attachment occurs at a certain distance downstream of the burner, followed by a decay in the remaining attached flame. This work will focus on finding the location where this heat flux value reaches its maximum and the implications of this location, as it may indicate transition from a momentum to buoyancy-dominant regime.

Distinct differences can also be observed from the flame images. Following Fig. 21 is a comparison of the flame images under 0.87 m/s and 2.13 m/s wind velocities, corresponding to the heat fluxes shown in Fig. 20. The differences between the two flame shapes are clear as the wind velocity goes from low to high.

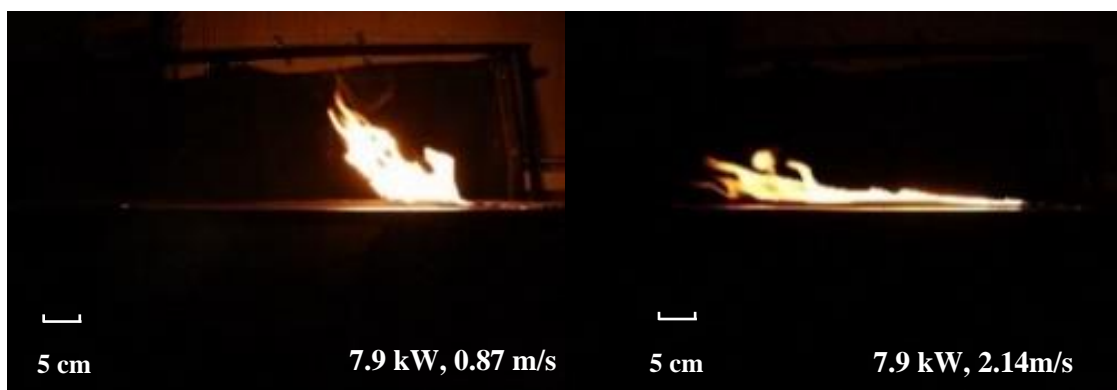


Figure 21. Experimental photos showing different flame shapes under wind.

Further analysis of the heat flux data shows that, when the wind velocity is relatively low, the heat flux distribution follows a power law, as has been reported in previous literature [90],  $\dot{q}_f''(x) = a(x/x_p)^n$ . The fitted constants  $a$  and  $n$  are shown in Fig. 22 for each test. Unlike previous results for upward or inclined flame spread, where the exponent,  $n$  varied from -2 to -7, here the exponent was closest to -1 for low velocities. This corresponds to a heat flux value roughly inversely proportional to the downstream distance. The constant  $A$  in front of the equations also varies between tests, which corresponds to different fire sizes. Based on these results, it can be inferred that, the larger the fire size, the higher the constant  $A$  will be, being proportional to the change in fire size. The fitted equations in Fig. 22 have an adjusted  $R^2$  value not less than 0.98, which means the fitted equations match the measured data well.

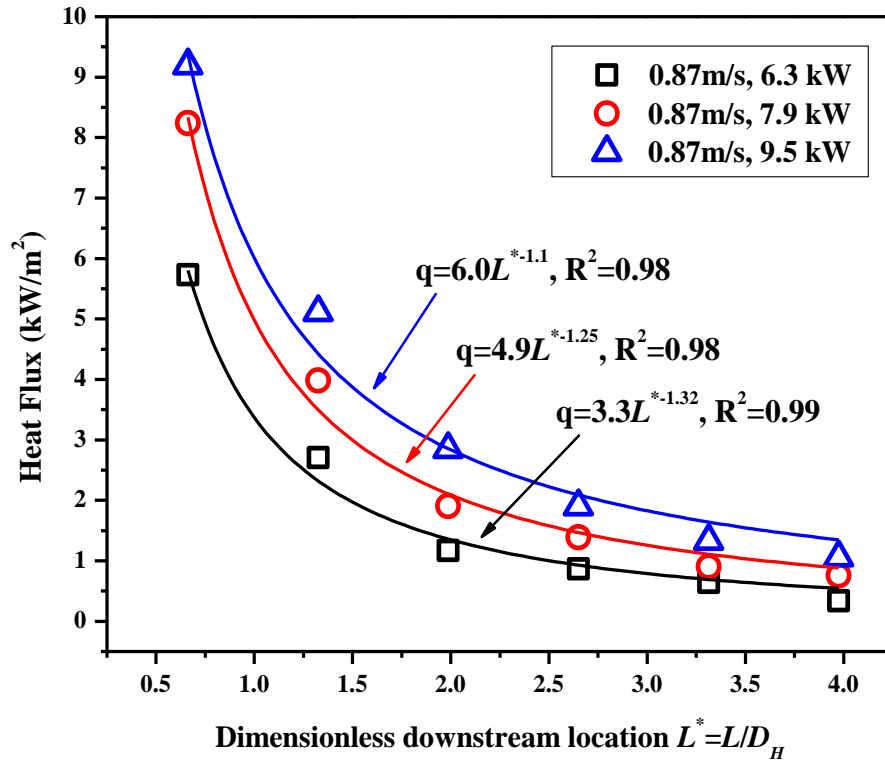


Figure 22. Heat flux distribution under low wind velocities.

#### 4.2 Richardson Number Analysis

What is clear from previous studies is that, when an external ambient flow is applied over a fire, natural convection from buoyancy and forced convection from the wind will both play a role in the shape of the flame and, consequently, the heat flux from the flame to surrounding unignited fuels. As the velocity of the wind is increased, a considerable portion of the heat flux from the flame will be received by the downstream surface because the flame will “tilt” or “attach” closer to that surface, increasing both convective heat transfer due to its closer location and radiative heat transfer due to its improved view factor. Apte [91] et al. studied wind-driven flame spread in an enclosed tunnel over PMMA, clearly

delimitating attached and plume flow regimes, however they were not able to draw larger conclusions as the flame spread and accelerated as a function of time [92]. Similarities can be seen, however, in combined forced and natural convection over a hot plate as our small-scale experiments are mostly dominated by convective heat transfer [93-95]. For these problems, the Grashof,

$$Gr_x = \frac{g\beta(T_h - T_\infty)x^3}{\nu^2} \quad (16)$$

and Reynolds numbers,

$$Re_x = \frac{Ux}{\nu} \quad (17)$$

have been used to described both heat transfer and transition problems in flames and hot plates, where  $T_h$  is the hot gas temperature,  $T_\infty$  is the ambient temperature,  $x$  is downstream distance along the plate,  $g$  the acceleration due to gravity,  $U$  the ambient velocity,  $\beta$  the thermal expansion coefficient, and  $\nu$  the kinematic viscosity of the ambient air. For flow over a hot plate, the relative role of buoyant and inertial forces has been divided into three regions based on the value of a correlating parameter,  $Gr_x / Re_x^b$ . It is noticed that several different values for the numerator,  $b$  have been selected in previous literature to describe flow over hot surface. For example [96], they chose  $b$  to be either 1.5 or 2.5 based on the geometry of the flow scenarios.

In this work,  $b = 2$  is chosen to describe the competition between forced and natural convection, taking the more common form of a Richardson number,

$$Ri_x = \frac{Gr_x}{Re_x^2} = \frac{g\beta(T_f - T_\infty)x}{U^2}, \quad (18)$$

where instead of using  $T_h$ , the temperature of the hot gases, the highest local flame temperature,  $T_f$  is used to describe the temperature difference which drives buoyancy. The local flame temperature was obtained by interpolating available temperature data in one vertical direction (nearly 20 points). These temperatures are found by applying a fit to the profiles of temperature and then interpolating the resulting equation to find the maximum temperature. Figure. 23 shows the measured local maximum flame temperature. This figure shows the temperature data obtained at a downstream location 16.5 cm from the trailing edge of the burner, with a fire size 9.5 kW and wind velocity 1.91 m/s. First, a best-fit equation is found for the existing dataset, then it is interpolated to find the highest local flame temperature. The same method is applied to all the test cases to get the temperature information for  $Ri_x$  analysis.

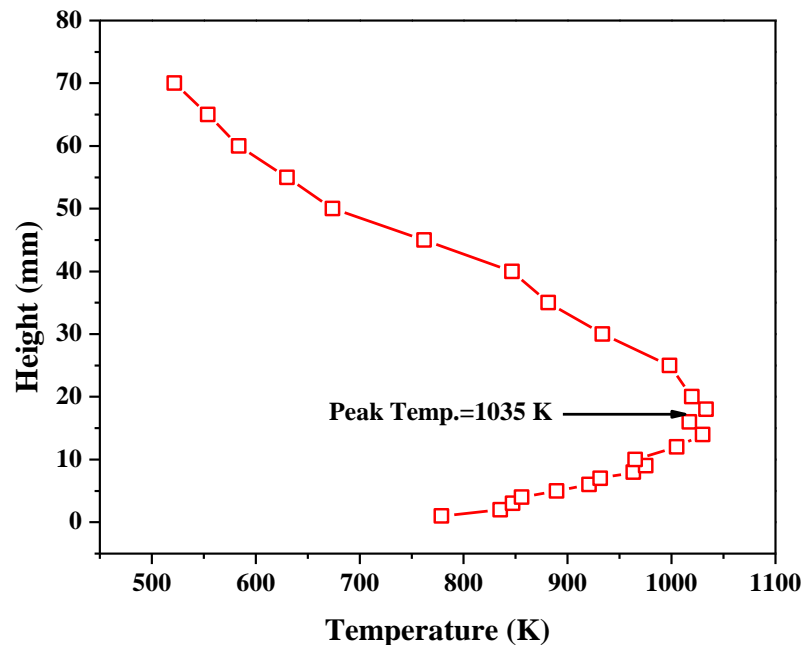


Figure 23. Vertical temperature profile taken 16.5 cm downstream of the trailing edge of the burner, with a fire size of 9.5 kW and a wind velocity of 1.91 m/s.

The local  $Ri_x$  can then be used to describe this competition within three regimes, dominated by, forced convection, mixed convection, and finally natural convection. These regions can be expressed as:

$$Ri_x \begin{cases} < 0.1 & \textit{forced convection controlled} \\ (0.1 \sim 10) & \textit{mixed convection} \\ > 10 & \textit{natural convection controlled} \end{cases} \quad (19)$$

Mixed convection flows have often been described as dominated by inertial forces when  $Ri_x < 0.1$ , and by buoyant forces when  $Ri_x > 10$  [97, 98]. For a fire problem under the effect of wind, where strong buoyant forces are introduced both due to high temperatures and distributed heat release, with relatively low wind velocities, most problems lie in the mixed convection region, where  $Ri_x$  is between 0.1 and 10. The details and implications of heat transfer modes in this mixed region ( $0.1 < Ri_x < 10$ ) is of particular interest in our case, where the transition from an inertial-dominant to buoyancy-dominant regime occurs. Thus, based on the temperature information collected from the flame, a local  $Ri_x$  number analysis can be performed. This will be used alongside the heat flux distribution to try to indicate a threshold for transition, coupled with observation of attached and plume behavior of the flame, such as that shown in Fig. 20.

The heat flux distribution to the surface downstream of the burner under high wind velocities is shown in Figs. 24 and 25. A clear transition point can be seen for these heat flux distributions. The location for the peak point is moving with increasing wind velocity. Since there are a limited number of heat flux data points for each experiment, to find the exact position where the local heat flux reaches a maximum, the data must be interpolated and fit.

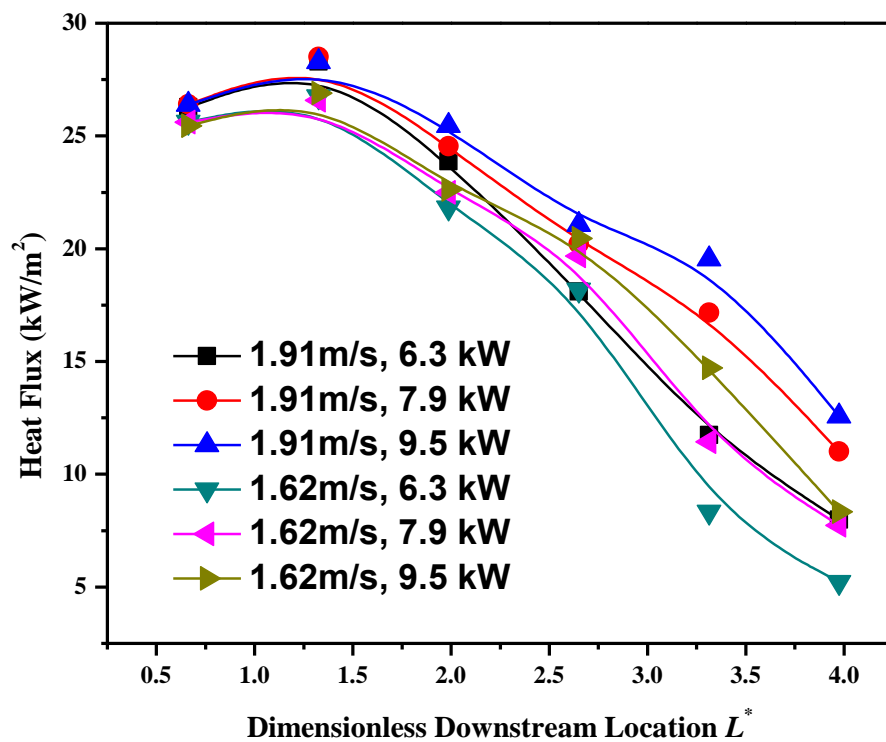


Figure 24. Heat flux distribution under high winds (1.62 and 1.91 m/s).

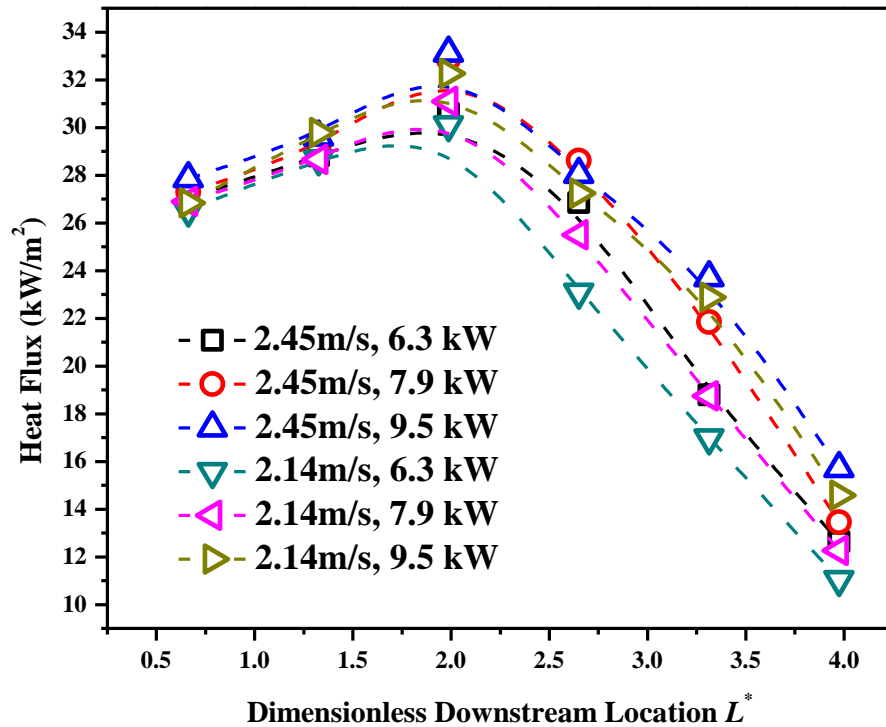


Figure 25. Heat flux distribution under high winds (2.14 and 2.45 m/s).

The local  $Ri_x$  number is also determined here for high wind velocities to describe competition between natural and forced convection. The highest local flame temperature was used as  $T_f$  and the distance  $L$  is taken as the characteristic length scale for  $Ri_x$ . From Figs. 26 and 27, one can tell that  $Ri_x$  generally increases with non-dimensional downstream distance  $L^*$ , from about 0.3 to 2.5. In order to find the implication of  $Ri_x$  and its influence on the heat flux distribution, a detailed analysis is performed.

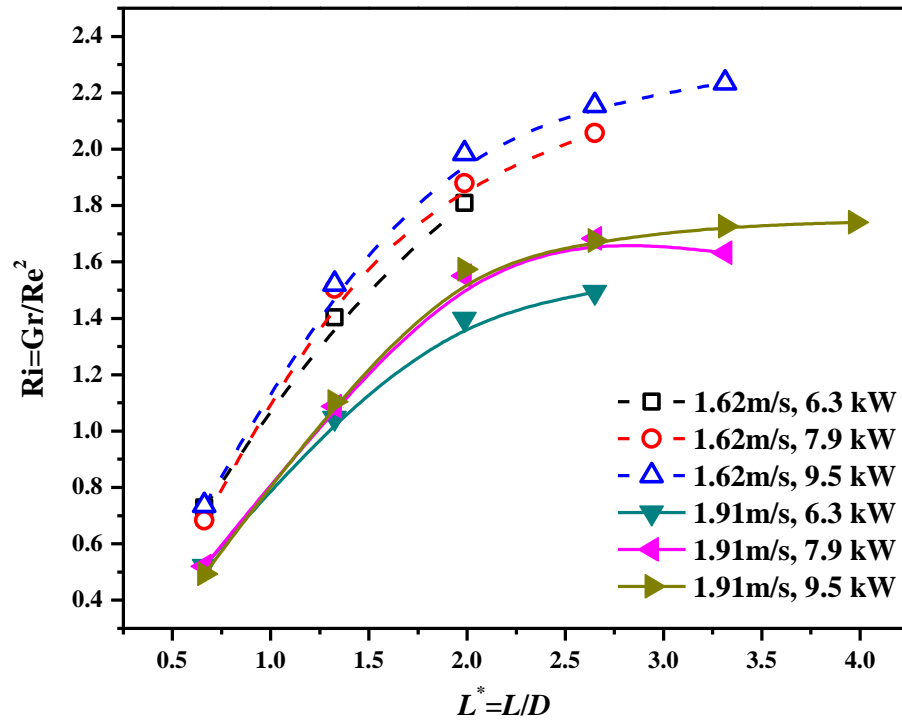


Figure 26. Local  $Ri_x$  number under high winds (1.62 and 1.91 m/s).

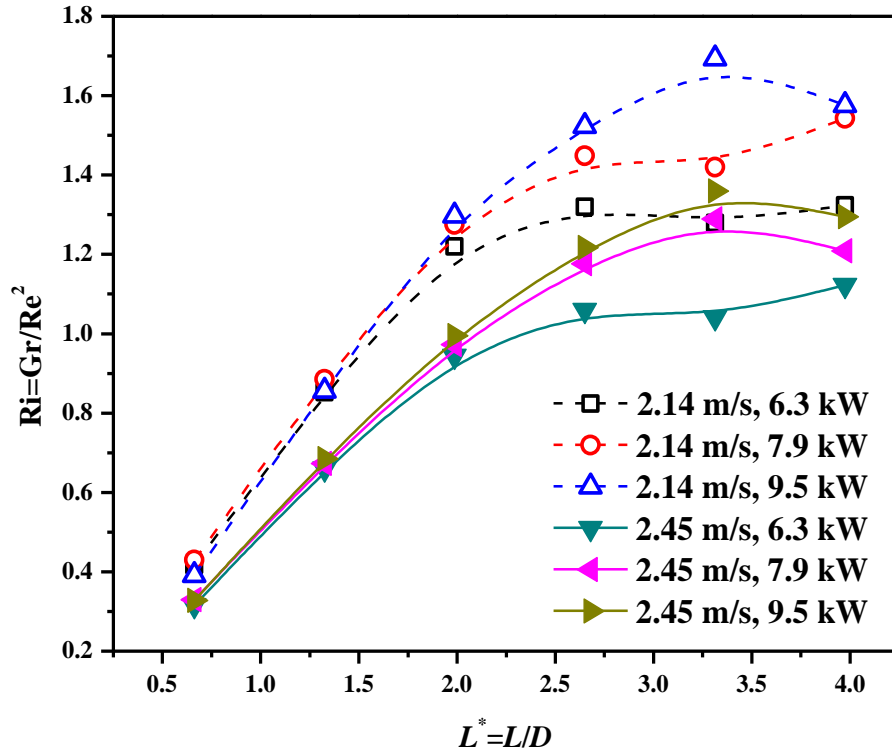


Figure 27. Local  $Ri_x$  number under high winds (2.14 and 2.45 m/s).

### 4.3 Non-dimensional Heat Flux and Correlations

An analysis of the local Richardson number,  $Ri_x$  was performed for the aforementioned fire cases. It is found that  $Ri_x$  along the downstream insulation board will undergo a transition as the flame grows and spreads downstream. When the flame starts at the burner leading edge,  $Ri_x$  is small ( $Ri_x < 1$ ) as  $Gr_x$  is smaller than  $Re_x$ , and the flame is forced to the surface, indicating that buoyant forces are weaker than the momentum forces introduced by the wind. With continued downstream distance and heat-release from the flame, the buoyant force increases until it equals the forward momentum forces ( $Ri_x = 1$ ). After this point, the flame becomes buoyantly dominated and appears as an upward plume lifted away from the

fuel surface. In Figs. 28 and 29,  $Ri_x$  and the local total heat flux to the surface are plotted against  $L^*$  for two scenarios, a 9.5 kW fire size under 1.91 m/s wind velocity, and a 7.9 kW fire size under 2.14 m/s wind velocity. In both scenarios, the dimensionless location where  $Ri_x=1$  ( $L_{Ri_x=1}^*$ ) and where the peak heat flux is observed ( $L_{peak}^*$ ) appear to occur at the same location, shown in Fig030. Then the same method has been applied to all the experimental cases investigated. The two key locations,  $L_{Ri_x=1}^*$  and  $L_{peak}^*$ , were noted and tabulated. Figure 28 then compares the correlation between  $L_{Ri_x=1}^*$  and  $L_{peak}^*$ . As they are very nearly linearly correlated, it shows the location where the buoyant-inertial transition appears also is the location of maximum heat flux. This means that when the local  $Ri_x$  reaches unity, or the buoyant force equals the viscous force in wind-driven fires scenarios, the local heat flux on the downstream surface reaches a maximum. This has strong implications for the fuel heating process. A correlation of local heat flux distribution and local  $Ri_x$  will next be developed.

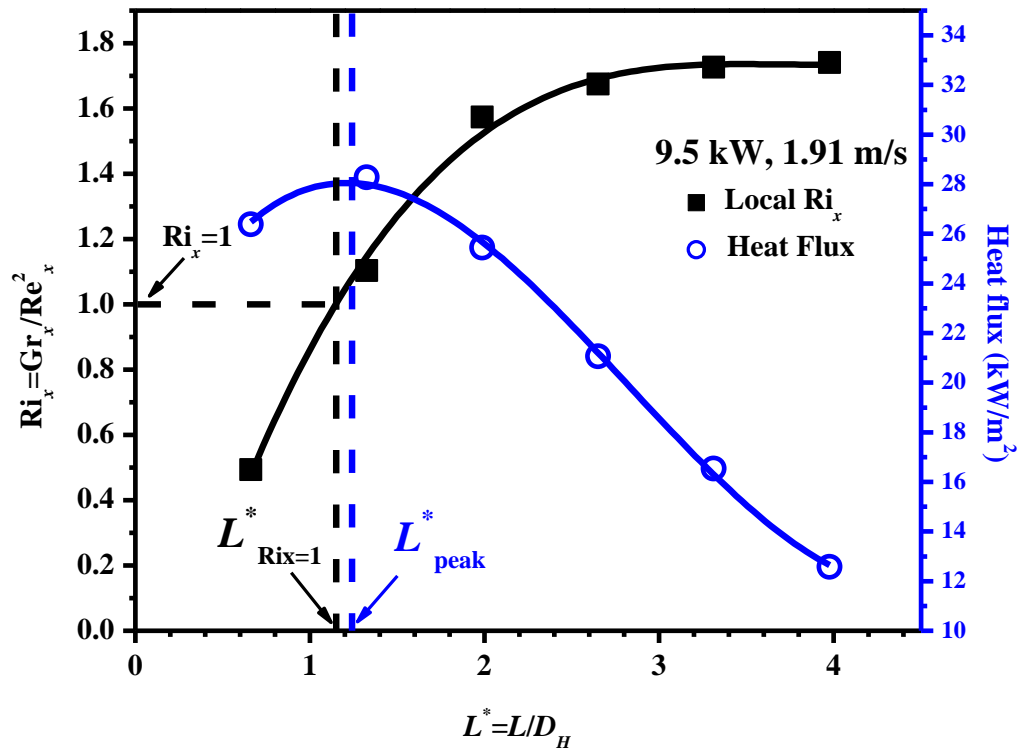


Figure 28. Local  $Ri_x$  number with local heat flux (9.5 kW, 1.91 m/s).

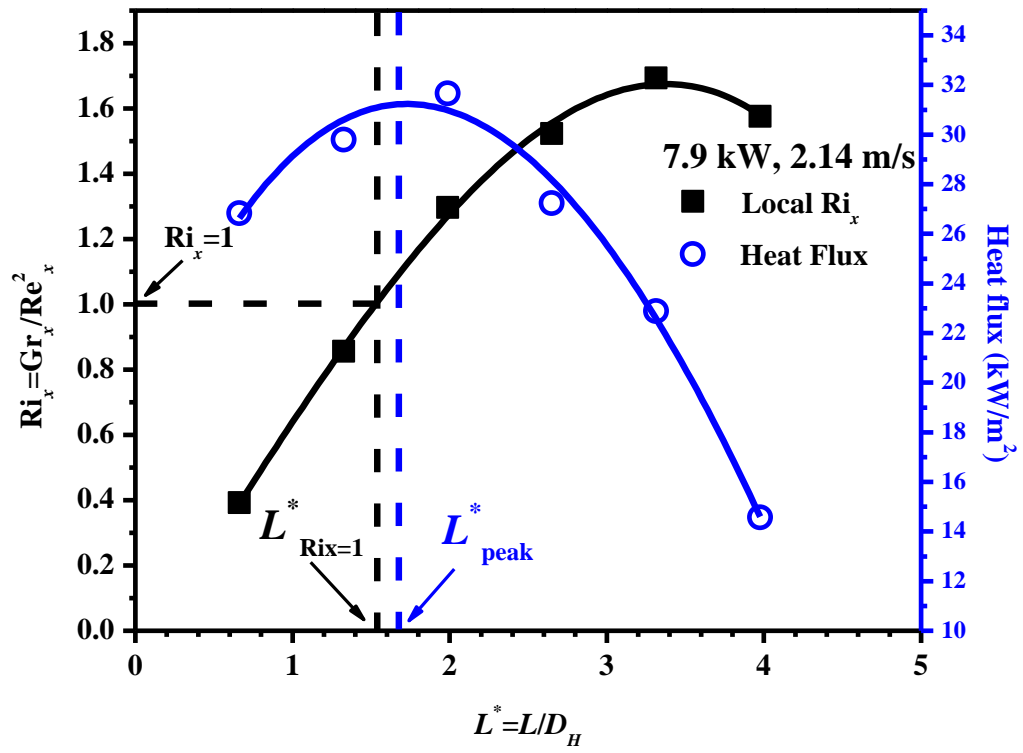


Figure 29. Local  $Ri_x$  number with local heat flux (7.9 kW, 2.14 m/s).

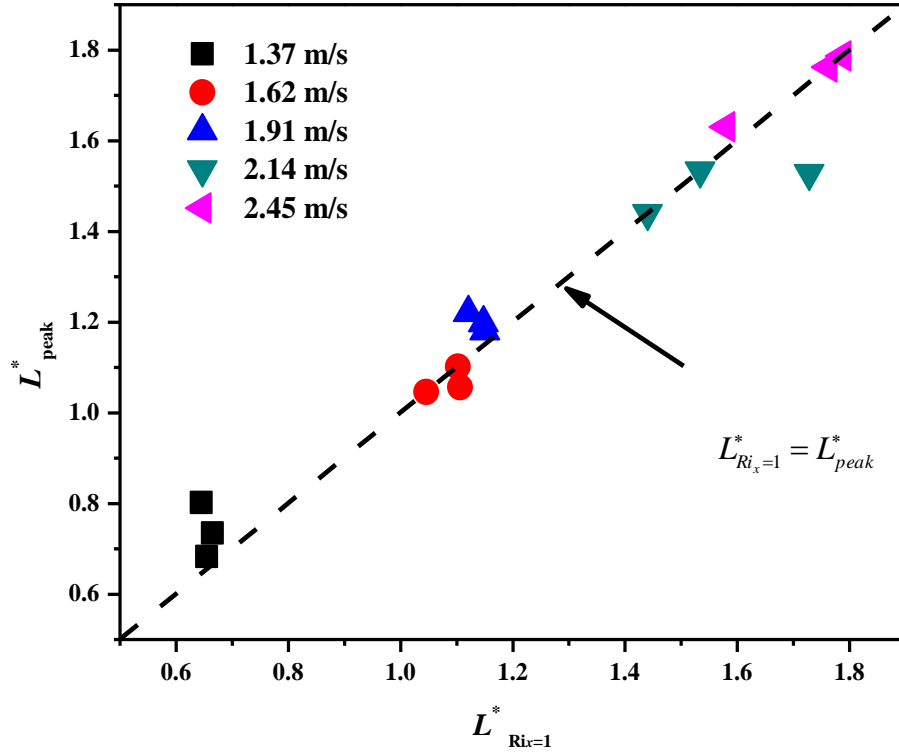


Figure 30. Comparison of dimensionless downstream location at  $Ri_x = 1$  with the peak heat flux value.

Looking back to images of the flame in forced and plume-like configurations, the peak heat flux observed where  $Ri_x=1$  seems reasonable as the flame is observed to slightly curve before reaching an inflection point where it transitions to a plume-like configuration. This inflection point apparently causes significant flame attachment, which most likely results in very high convective heat fluxes (only total, radiative plus convective measurements were conducted for this study). Figure 31 shows the dimensionless local total heat flux  $\dot{q}_f^*$  plotted against the local  $Ri_x$ , where  $\dot{q}_f^*$  is

$$\dot{q}_f^* = \dot{q}_f'' / (\rho_a c_p \Delta T \sqrt{AgL}) \quad (20)$$

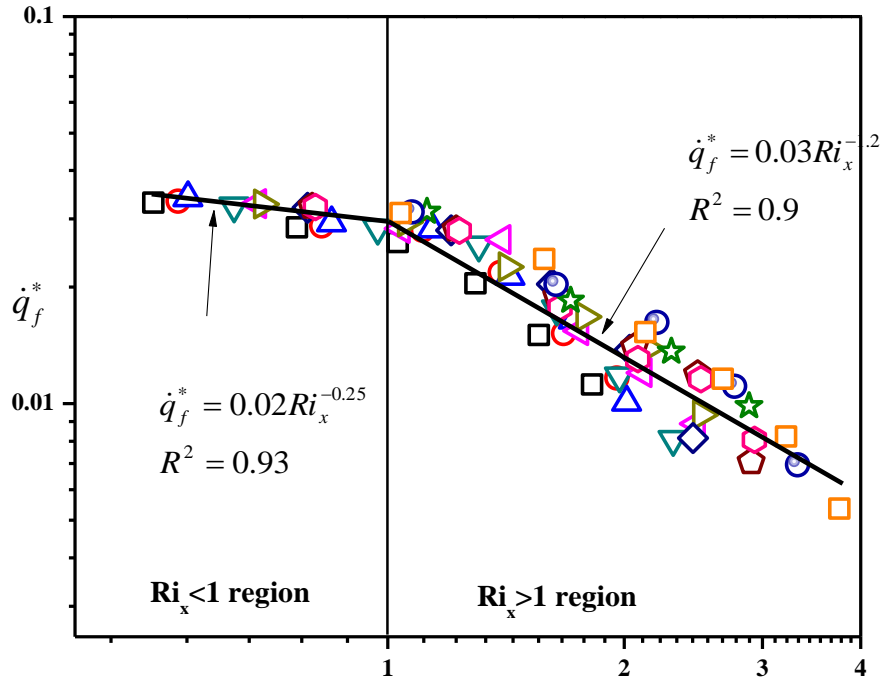
and 
$$A = \Delta T / (T_f + T_\infty) \quad (21)$$

with  $\Delta T = T_f - T_\infty$  the difference between the flame and ambient temperature, and  $\rho_a$  and  $c_p$  the density and specific heat capacity of air, respectively.  $A$  is an adapted Atwood number for ideal gases used in the study of hydrodynamic instabilities in density stratified flows, more commonly defined as  $A = (\rho_1 - \rho_2) / (\rho_1 + \rho_2)$ . The Atwood number is an important parameter in the study of Rayleigh-Taylor instabilities, which are believed to be important in wind-driven flame spread problems [99].

A piece-wise function which correlates the non-dimensional heat flux distribution (Eq. 20) with the local  $Ri_x$  number was fit to experimental data and can be expressed as:

$$\dot{q}_f^* = \begin{cases} 0.02 Ri_x^{-0.25} & Ri_x < 1 \\ 0.03 Ri_x^{-1.2} & Ri_x > 1 \end{cases} \quad (22)$$

The local total heat flux to the downstream surface can then be correlated between two regimes, with a turning point at  $Ri_x=1$ . Before  $Ri_x=1$ , the non-dimensional heat flux changes with local  $Ri_x$  as  $\dot{q}_f^* = 0.02 Ri_x^{-0.25}$ , with a  $R^2=0.93$ , while when  $Ri_x>1$ , it changes as  $\dot{q}_f^* = 0.03 Ri_x^{-1.2}$ , with a  $R^2=0.9$ . Both equations provide a relatively good fit to the experimental data. Equation (22) is shown as a solid line in Fig. 31, where it can be used to estimate the local total heat flux distribution on the downstream surface for a variety of ambient flows and fire sizes.



$$Ri_x = Gr_x / Re_x^2$$

Figure 31. Dimensionless local total heat flux with local  $Ri_x$ .

#### 4.4 Discussions and Conclusion

In this chapter, the total heat flux distribution on the downstream surface is investigated in wind-driven line fires. It is found that the heat flux distribution profile changes under different wind velocity and fire size regimes. When the wind velocity is low, the heat flux will decrease with downstream surface, and when the wind velocity is high, local heat flux will first rise to a peak value then decrease with downstream distance. The local Richardson number is used to fit experimental data and it is found that the location where the local heat flux reaches its maximum matches the location where the local  $Ri_x$  number reaches unity. This signals a transition point at  $Ri_x=1$ , at which point the local heat flux profile reaches a turning point, too. Finally, a piece-wise function is proposed to correlate the non-

dimensional heat flux with local  $Ri_x$  number. Information from this chapter on the local heat flux distribution could help shed light onto the fuel heating process and fuel ignition process in wind-driven wildland fires.

## **Chapter 5: Flame Fluctuations and Attachment Length**

Pulsations, or “bursts” of flame forward beyond a mean flame front have been observed for many different fires, however, few if any works in the literature have addressed this subject. In this study, a stationary gas burner is used to investigate forward pulsations of flames. The flame shape and location of a wind-driven fire are important information as they could potentially determine the region where the flame can reach, and thus the pre-heating area. The flame shape and location are recorded using high-speed side-view video and a methodology is applied to study the controlling parameters.

### **5.1 Measurement Methodology**

A region starting at the downstream edge of the burner and extending fully downstream, 1 cm above the surface [12], was determined as a region of interest where extension of the flame would relate to flame attachment and fuel particle heating, as shown in the dashed rectangle in Fig. 32. The flame location was then determined in this region of interest by tracking the furthest-most downstream tip of the flame. This location fluctuated in time, where it was observed that the flame would pulse downstream, “bursting” into what would be the unburned fuel region in a spreading fire experiment. Experimental videos were loaded into a MATLAB script for analysis. While the 1 cm height chosen for the region of interest is somewhat arbitrary, the results are found to scale regardless of this height, with their absolute values adjusting slightly. To eventually connect these results to real wildland fire spread, a fuel bed height could be defined for specific scenarios.

With captured high definition video perpendicular to the flame, the two-dimensional intermittent flame behavior and its corresponding characteristic properties is extracted.

This, of course, averages any variability along the width of the flame, however, the flame generally seemed to pulsate along its entire width when observed from above, indicating that spatial averaging does not induce a large error to the analysis.

Each image in the video was cropped to this same region of interest and then converted to a black and white image using a threshold value based on the average light intensity. This analysis included taking a number random images from the video and determining the flame/non-flame regions based on light intensity for that specific image using a MATLAB tool based on Otsu's method [100]. The result of this light intensity analysis for each image was a conversion factor which was averaged from each of the 6 images randomly selected from each video. This average conversion factor was used for all images in the video and further analysis of the experiment. The flame attachment location ( $x_a$ ) was finally determined as the furthest downstream pixel in the region-of-interest that satisfied the flame threshold level, as shown in Fig. 32.

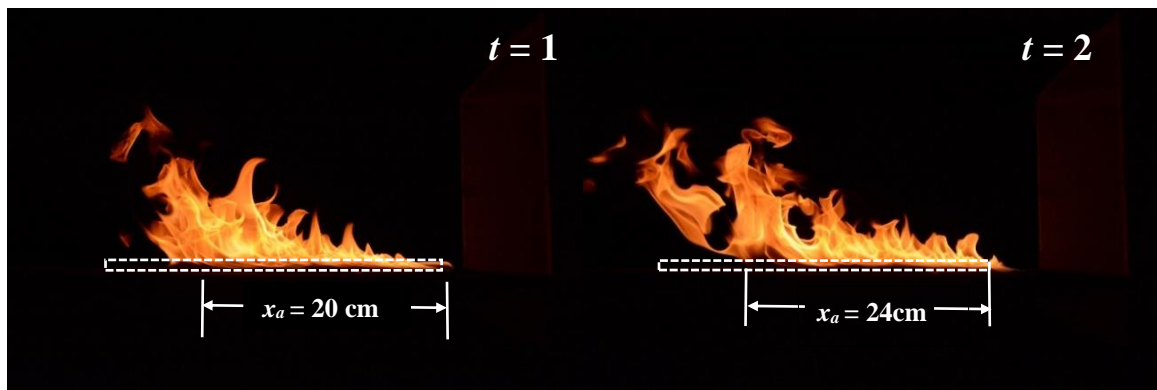


Figure 32. Flame location between two time steps in a forced flow experiment. The flame attachment location ( $x_a$ ) is measured from the downstream edge of the burner to edge of the flame within the attachment region.

In the image analysis, the threshold was chosen based on the highest level of light intensity present in 6 random images. Then this thresholding method is applied to convert the gray-scale flame images to binary images from black and white, with 1 indicating flame and 0 indicating non-flame. Average images from one experiment are obtained by dividing the summation of all binary matrices by the total number of images. A 50% probability method was used to define the average flame shape following Audoin et al. [101], shown in Fig. 33. The process of image analysis is shown from still flame images obtained in experiments to a black-white binary image, and finally to the average flame shape and geometry represented by a red line. The average flame shape, including the average flame length from the center of the burner to the flame tip ( $L_f$ ), the flame tilt angle from the flame tip to the horizontal ( $\theta$ ), and the horizontal flame extension length ( $x_f$ ) were obtained using flame outlines from side-view images, illustrated in Fig. 34.



Figure 33. Flame image processing based on luminosity

The flame location in the downstream direction, within a region of interest (ROI) 1 cm above the flat, inert surface past the end of the burner was then calculated based on whether the flame was present using the 50% probability criterion. This was necessary as the flame was observed to fluctuate within this region in time, resulting in intermittent flame attachment close to the surface.

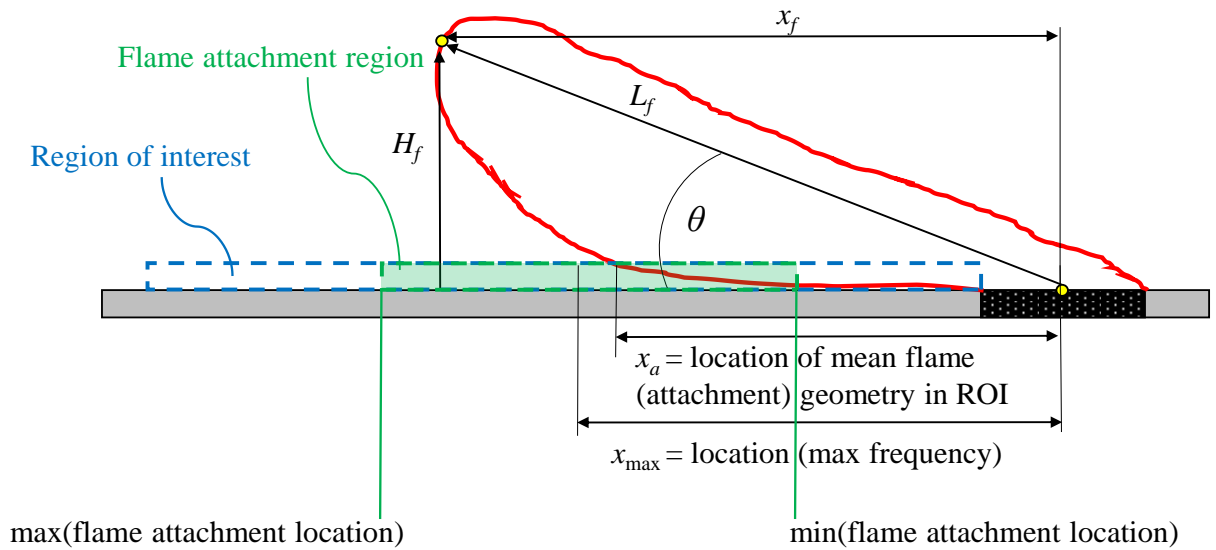


Figure 34. A side-view of mean flame properties including the flame height  $H_f$ , flame length  $L_f$ , maximum frequency location  $x_{max}$ , mean flame attachment length  $x_a$ , horizontal flame length  $x_f$  and flame tilt angle  $\theta$

The flame pulsation frequency was obtained from the forward flame location as a function of time (Fig. 35) using a variable-interval time-averaging (VITA) method [102], following the analysis of pulsations from thermocouples in larger scale spreading experiments [10]. Level-crossing was only considered for the forward direction, thus only when the flame was not at a location in the previous time step, and then appeared at the next time step, was it considered a crossing to avoid double-counting. The resulting forward flame pulsation frequency was then determined at each downstream location by dividing the number of crossings by the total number of frames, multiplied by the frame rate of the video.

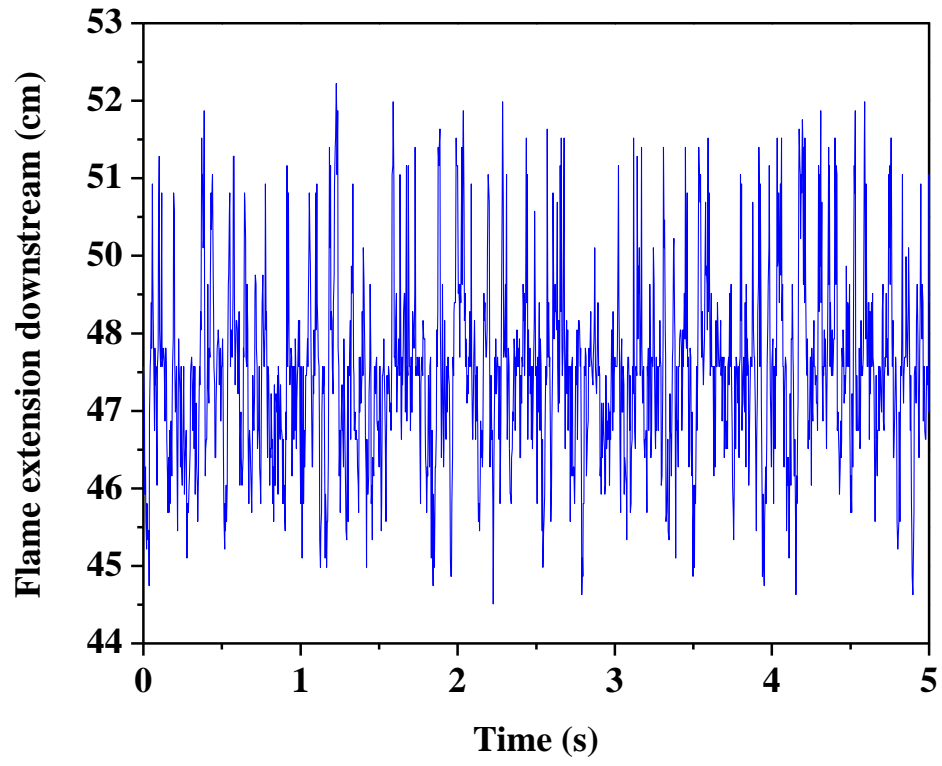


Figure 35. Fluctuating flame extension with time.

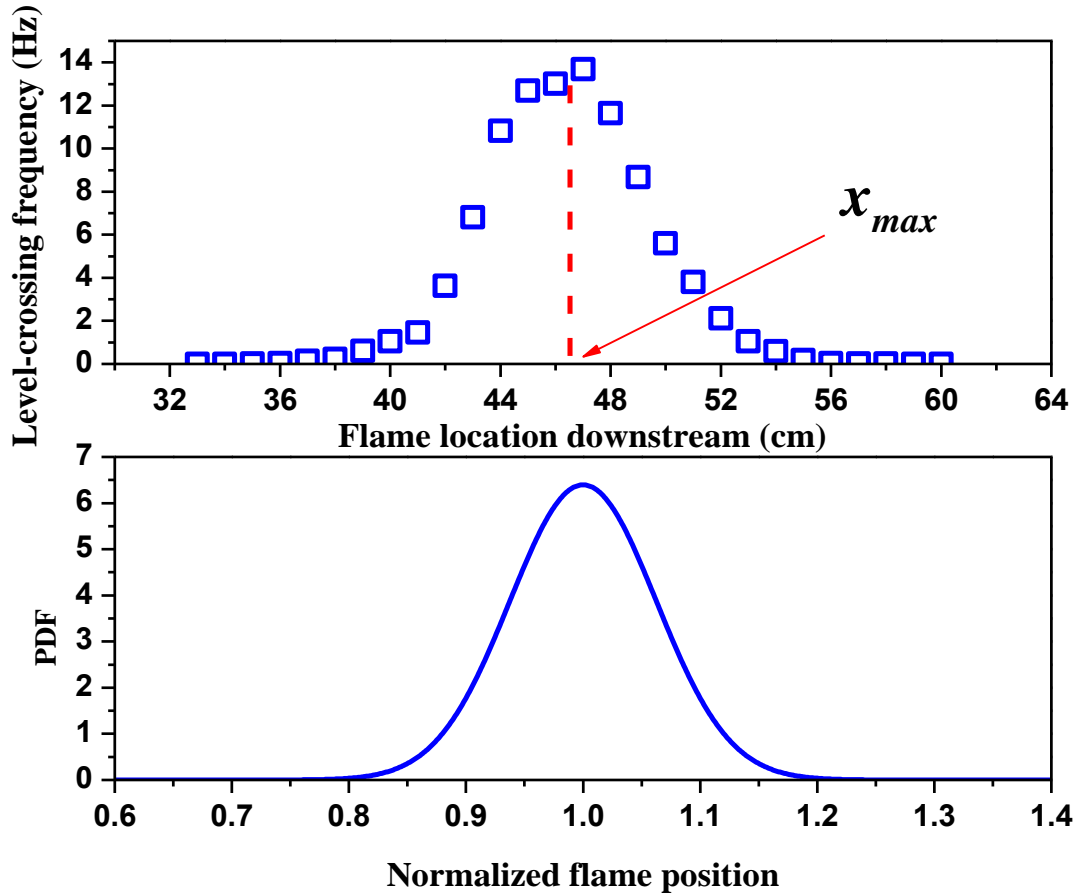


Figure 36. Probability Density Function (PDF) of normalized flame position

## 5.2 Maximum Flame Pulsation Location

The downstream flame extension within the attachment region fluctuated in time, causing intermittent flame contact within the simulated unburnt fuel region. The flame position in time was compared to each of these locations and the number of occurrences was tallied. The frequency for each location was then determined by dividing the number of crossings by the total number of frames analyzed, and multiplying by the frame rate of the video. Thus, based on the flame location over time (Fig. 36, top), the level-crossing frequency can be extracted for each flame location downstream (Fig. 36, bottom). The maximum flame frequency position,  $x_{max}$  was determined using the method described in previous section,

corresponding, for instance, to 46.5 cm in Fig. 36, bottom. The same method was used for each fire/wind configuration. This length was observed to be similar to the average flame attachment length, which in this experiment was determined by measuring the instantaneous attached flame length,  $x_a$  within a 1 cm tall crop box downstream of the burner for each frame and averaging this value.

The flame forward pulsation frequency,  $f_F$  may have an effect on the rate of fire spread when intermittent heating is important [10]. It would therefore be desirable to know the location of maximum frequency, and if that location corresponds to mean flame features for which relationships already exist. Using the defined mean flame geometry from Fig. 32, we can calculate an approximate horizontal flame length,

$$x_f = L_f \cos(\theta) \quad (23)$$

which provides a reasonable correlation between the flame length and flame tilt angle. This has previously proven useful in the study of flame shapes under wind [103]. Assuming the centerline of the flame is straight, the flame tilt angle,  $\theta$ , is approximately a function of wind velocity,  $U_{wind}$  and a buoyant vertical velocity from the flame  $V$  [104, 105], approximated as,

$$\tan(\theta) \approx \frac{V}{U_{wind}}. \quad (24)$$

Based on correlations by Thomas [106] and Rasbash [107],  $V$  can be correlated with the flame length for vertical fires as,

$$V = 0.51(gL_f \frac{\Delta T_f}{T_0})^{0.5}, \quad (25)$$

where  $g$  is the acceleration due to gravity,  $L_f$  is the flame height,  $\Delta T_f$  is the flame temperature rise over ambient, and  $T_0$  is the ambient temperature. Assuming the centerline of the flame is approximately a straight line, as illustrated in Fig. 32,

$$\tan(\theta) \approx \frac{0.51(gL_f \frac{\Delta T_f}{T_0})^{0.5}}{U_{wind}}, \quad \cos(\theta) = \frac{U_{wind}}{\sqrt{0.26gL_f \frac{\Delta T_f}{T_0} + U_{wind}^2}}. \quad (26)$$

Thus, the flame horizontal length,  $x_f$  can be re-written as,

$$x_f = L_f \cdot \frac{U_{wind}}{\sqrt{0.26gL_f \frac{\Delta T_f}{T_0} + U_{wind}^2}}. \quad (27)$$

Figure 35 shows the relationship between the location of the maximum flame pulsation frequency,  $x_{max}$ , with the horizontal flame length,  $x_f$ . It is found that there is a clear linear relationship between the maximum frequency position and the horizontal flame length, with an  $R^2$  value of about 0.87, which indicates the data fits fairly well with the function. Including Eq. (27), we then can develop a relationship between  $x_{max}$ ,  $L_f$  and  $\theta$ , which can be expressed as

$$x_{max} = 5.2 + 0.74L_f \cdot \frac{U_{wind}}{\sqrt{0.26gL_f \frac{\Delta T_f}{T_0} + U_{wind}^2}}, \quad (28)$$

where  $L_f$  and  $x_{max}$  are measured in cm.

Equation (28), plotted in Fig. 37, describes the relationship between the maximum frequency location and the averaged flame shape. The maximum flame pulsation frequency is seen to occur in a specific normalized position of wind-blown flames, perhaps indicating that there is a location where attachment is most unstable and the flame's position

fluctuates with time. Using this fit, the location of the maximum flame pulsation frequency can be estimated using mean flame properties, particularly the flame length and the wind speed, which is useful as these parameters are much easier to measure in spreading flames. Continued study using stationary flames such as these may help to further elucidate the mechanisms by which these processes occur and improve our understanding of flame spread through wildland fuels.

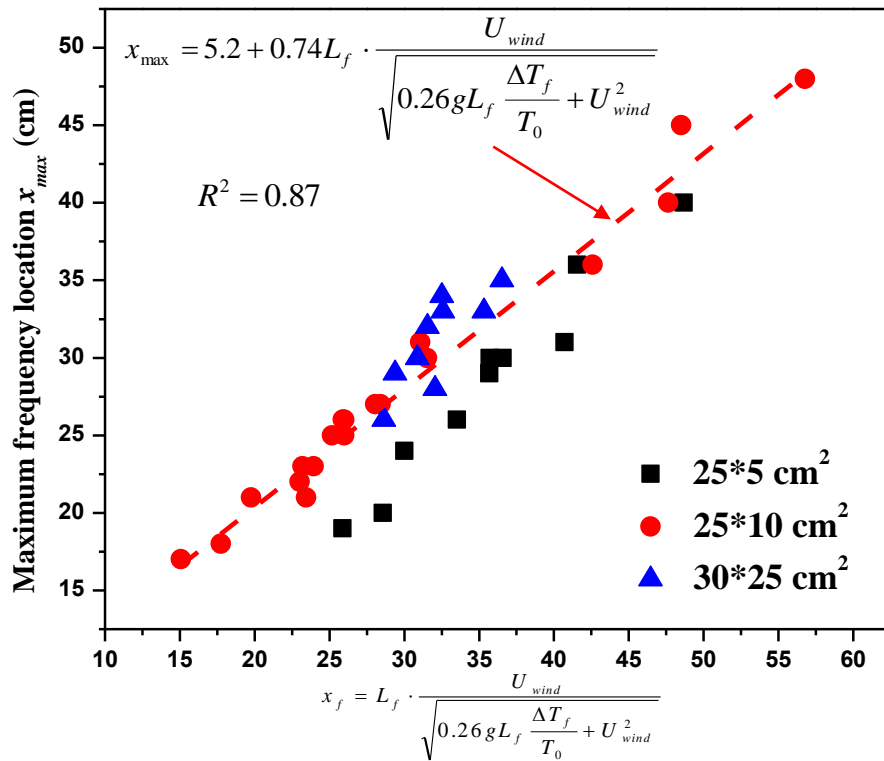


Figure 37. Horizontal flame length versus the location of maximum frequency,  $x_{max}$

Another important question that arises in flame spread is the distance a flame may extend forward of the mean flame attachment length,  $x_a$ . Previous studies have focused only on a

mean value, however, a statistical understanding of the flame location can provide more useful information when fine fuels in wildland are sensitive to fluctuation of the flame.

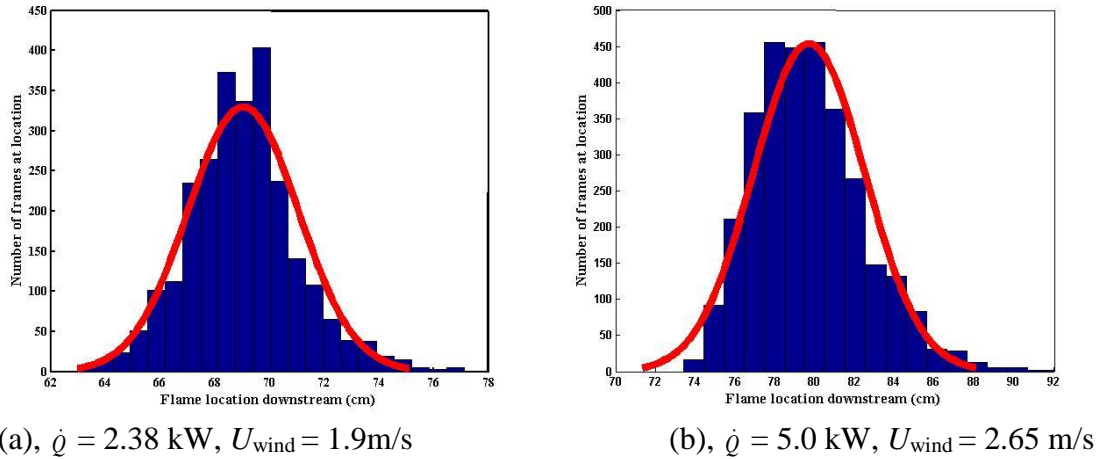
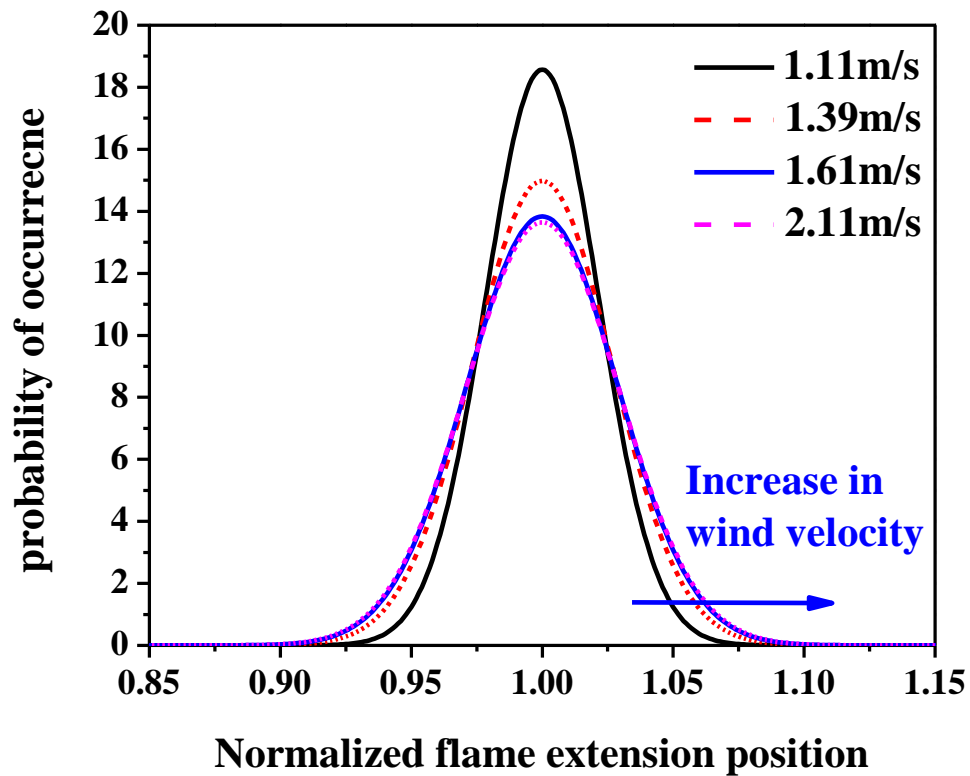


Figure 38. Histograms of flame extension length,  $x_a$  for a  $25 \times 5 \text{ cm}^2$  burner.

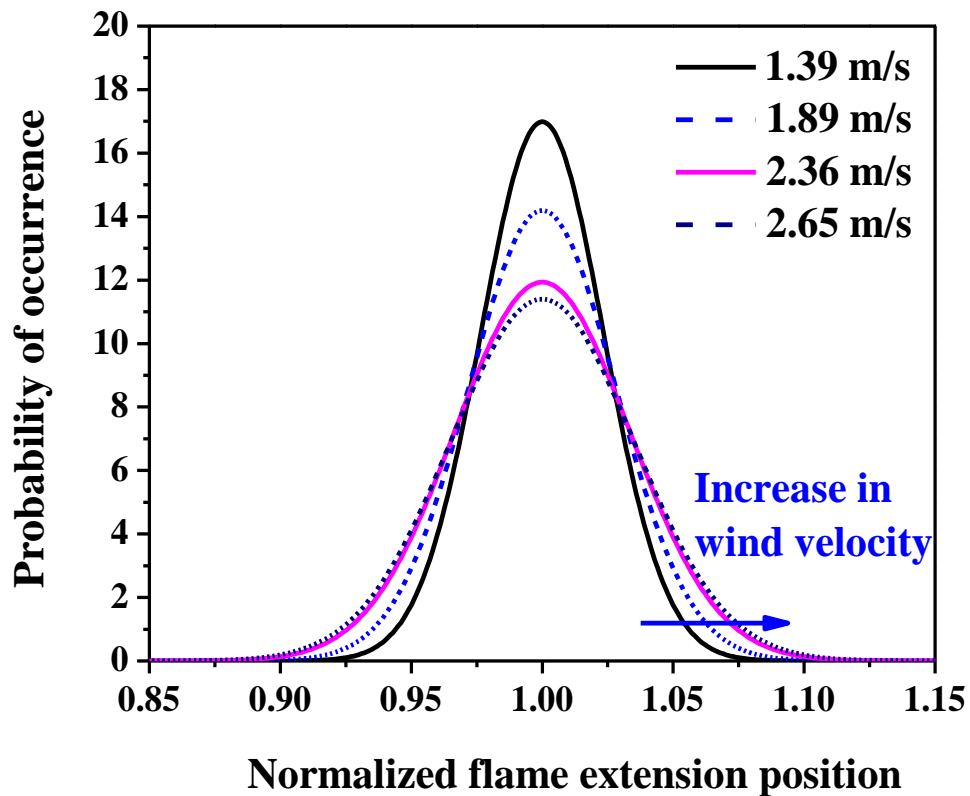
In order to illustrate the periodic movement of the attachment region, probability density functions (PDFs) of the normalized flame location versus the probability of the flame occurring at that location were created, shown in Fig. 38. The flame locations were normalized by the mean flame attachment length,  $\bar{x}_a$ , using the methods described above where the Gaussian curve-fits for occurrence created such that the area under each curve was equal to unity. These PDF's therefore indicate the probability that the attachment region of a flame would extend beyond the mean flame location and vice versa. As shown in Fig. 38, both configurations have a  $25 \times 5 \text{ cm}^2$  burner with 8(a),  $\dot{Q} = 2.38 \text{ kW}$ ,  $U_{\text{wind}} = 1.9 \text{ m/s}$ , and  $Fr = U_{\text{wind}}^2 / gL = 4.28$ ; and 8(b),  $\dot{Q} = 5.0 \text{ kW}$ ,  $U_{\text{wind}} = 2.65 \text{ m/s}$  and  $Fr = 6.27$ .

Figure 39 shows the Gaussian fits to the PDF's of  $x_a$  for two different heat-release rates, 3.2 and 5.0 kW, for a range of wind velocities. It is clear from the Fig. 39 that, for the same fire size, an increase in wind velocity will cause the flame to extend increasingly further

from the mean flame position, even when normalized with mean properties. The significance of this result is that increasing winds will cause the attachment region of flames to extend significantly further into unburnt fuels during flame spread, further explaining why periodic bursts of flames may be a significant factor in heating during flame spread.



(a) Fire size = 3.2 kW



(b) Fire size = 5.0 kW

Figure 39. Probability of normalized flame attachment length,  $x_a/\bar{x}_a$  for different fire sizes and wind velocities.

The variance of the normalized flame attachment length,  $x_a/\bar{x}_a$  from Gaussian curve fits,  $\sigma^2$ , were extracted for each fire case. Increasing values of  $\sigma^2$  indicate an extension of the “wings” of the PDF’s as shown in Fig. 39, which represents an increasing probability of both up and downstream extensions from the mean flame position. In other words, a large  $\sigma^2$  increases the probability of a flame “burst” forward from the mean flame locations.

Further study of the flame extension found that  $\sigma^2$  has a strong correlation with  $Fr^{2/3}/Q^*$ , where  $Fr = U_{wind}^2 / gL$  and  $Q^* = \dot{Q} / (c_p T_0 \rho_0 g^{0.5} L^{2.5})$ .  $Fr^{2/3}/Q^*$  has been found to be a good indicator of wind-driven flame movement in previous studies [108, 109]. The variance  $\sigma^2$  first increases with increasing  $Fr^{2/3}/Q^*$ , then reaches a plateau (Fig. 40). This signifies that, as the ratio between wind momentum over flame buoyancy increases, the flame extends further from the mean flame attachment length,  $\bar{x}_a$ . As  $Fr^{2/3}/Q^*$  continues to increase and exceeds about 2.5, the correlation begins to level off, where  $\sigma^2$  is less dependent on the ratio. This observation is expected as the flame starts to become fully attached to the surface at high wind velocities, reaching a maximum possible extension length with significantly less movement from the mean flame location. Eventually at high velocities, the flame will start to extinguish at the leading edge, however, this situation was avoided in this study as it is not in the same regime as spreading fires.

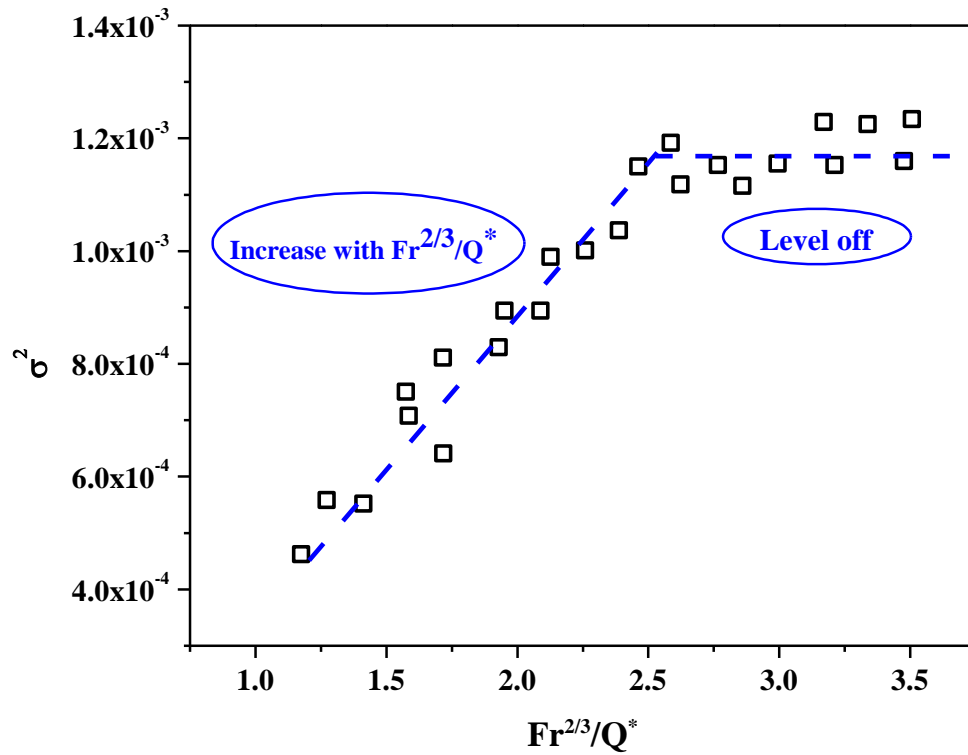


Figure 40. The variance,  $\sigma^2$  of the normalized flame attachment length,  $x_a/\bar{x}_a$ , from Gaussian curve fits versus  $Fr^{2/3}/Q^*$

### 5.3 Flame Attachment Length

The flame attachment length of a wind-driven fire along the downstream surface is also an important parameter in assessing flame spread. It more directly describes the competition between natural convection and forced convection, and should correlate with measured heat fluxes along the surface for these smaller, convectively-dominated flames. Averaged flame images were first obtained using a 50% threshold that was describe in Section 4.1 to determine the flame shape. In Fig. 41, we first obtained the averaged flame shape for one case from hundreds of separate images. The flame attachment length for each test was

obtained by analyzing averaged side-view images. An intensity threshold determining the flame/non-flame region was applied to the images to give iso-contours of the flame shape.

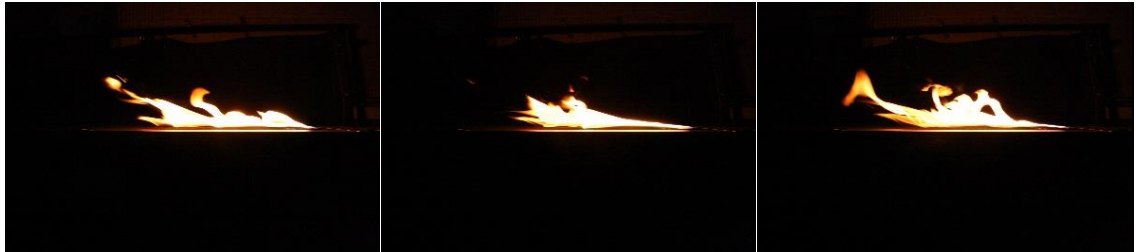


Figure 41. Averaged flame image from experimental pictures

After obtaining the averaged flame shape, the flame images are processed in a MATLAB program, to get the iso-contour flame images for each case. Figure 42 shows resulting averaged flame with different wind velocities for the same fire size. The flame attachment length was then defined as the distance between the burner trailing edge to the downstream location where the flame contour is 5 mm from the downstream surface. Different threshold

heights were used to determine the flame attachment length (1, 2, 4, 6 mm) to give a representation of the potential error seen in Fig. 42. As the wind velocity is increased, the distance along which the flame attaches to the surface increases, but does so at a slower rate once the flame becomes nearly attached along the surface. This behavior will increase heat fluxes to the downstream surface which would, in turn, increase rates of flame spread. We measured the flame attachment length using the scales given in the figures. The flame attachment length information is then further analyzed and compared with a local  $Ri_x$  number used earlier as well as compared to the location where local heat flux reaches a peak value.

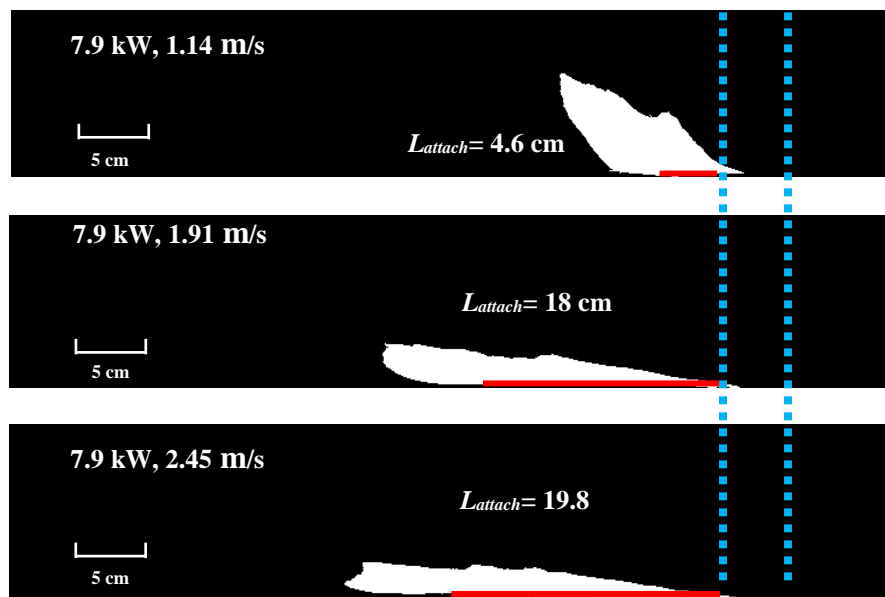


Figure 42. Averaged flame images under different wind velocities show the attachment length ( $L_{attach}$ ) of the flame to the surface with scales. Regions between the two blue dashed lines represent the burner depth, while the red solid lines, which are 5 mm in height, represent the flame attachment length measured along the downstream surface.

The dimensionless flame attachment length,  $L_{attach}^*$  was calculated by dividing the attachment length by the hydraulic diameter of the burner surface,  $D_H$ .  $L_{attach}^*$  was then plotted against  $L_{Ri_x=1}^*$ , the dimensionless location where  $Ri_x=1$ , representing nearly equal competition between buoyancy and momentum at that point. After plotting the values, shown in Fig. 43, a clear linear relationship was found between  $L_{attach}^*$  and  $L_{Ri_x=1}^*$ ,

$$L_{attach}^* = 1.55 + 0.5L_{Ri_x=1}^*. \quad (29)$$

Because we can choose different thresholds for determination of the flame attachment length, different definitions for  $L_{attach}^*$  could shift the values in Fig. 43 up or down a little bit, however the attachment height (5 mm) was varied  $\pm 15\%$  to determine the error bars shown, which clearly has little effects on the relationship. Therefore, the flame attachment length appears to be directly correlated with the location of maximum heat flux, meaning that this location corresponds to the transition between where boundary layer to plume like burning occurs.

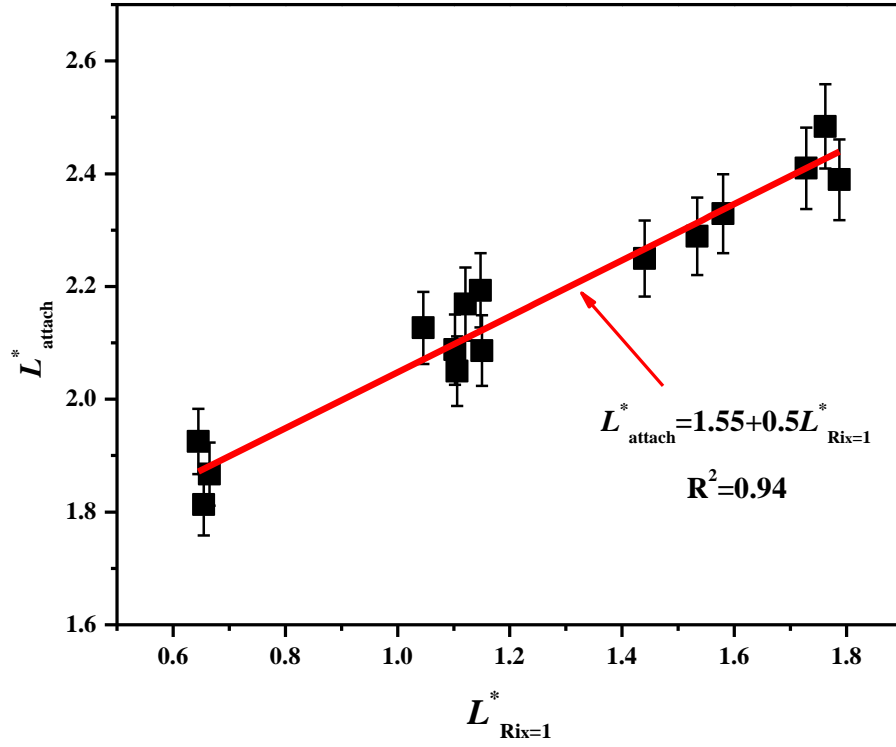


Figure 43.  $L_{Rix=1}^*$  with dimensionless flame attachment length  $L_{attach}^*$  where error bars shown represents variation in the chosen threshold heights.

Following analysis from the previous section where a relationship was found between the local  $Ri_x$  number and the location where the local heat flux reaches a peak, the non-dimensional flame attachment length on the downstream surface,  $L_{attach}^*$  in terms of  $L_{peak}^*$  is found to be expressed as:

$$L_{attach}^* = 1.55 + 0.5L_{Rix=1}^* \quad (30)$$

#### 5.4 Discussions and Conclusion

In this chapter, the flame shape in wind-driven fire is investigated, with a focus on the flame intermittent fluctuation length and flame attachment length on the downstream

surface. An average flame shape was first obtained using image analysis, followed by a flame extension length in the region-of-interest tracked using the VITA method. The location of maximum flame pulsation frequency was collected and compared with the average flame measurements. A correlation was proposed between the flame horizontal length and the maximum flame pulsation frequency location and a linear equation was found between the two parameters. The variance of the flame fluctuation was been found to be related to  $Fr$  and the fire heat release rate,  $Q^*$ . The flame attachment length on the downstream surface was also studied, and a linear correlation was found between the flame attachment length and the location where the local  $Ri_x$  reaches unity, the location where the flame starts to detach from surface shifts a little bit from the location where local heat flux reaches a maximum value.

Information from this chapter on the flame intermittent fluctuation can help shed light on the flame intermittent heating behavior. By using some average parameters determined from flame measurements, such as the flame length, flame height and flame tilt angle, one can estimate the flame fluctuation extension length. The variance of flame fluctuation is sensitive to wind velocity and fire heat release rate, which was found to be well correlated

with  $Fr^{2/3}/Q^*$ .

## Chapter 6: Flame Intermittent Frequencies

Most literature on wind-driven fire spread has focused on steady-state burning characteristics of these fires, preferring this time-averaged view of flame tilt angles, burning rates and downstream heat fluxes to the more complicated, stochastic movements that flames make. The fluctuation of the flame front, however, has recently been determined to play an important role in flame spread, in particular for wildland fires. The movement of flames therefore may have implications in a variety of wind-driven scenarios, wherever flames reside long enough to heat unburnt fuels and thus contribute to forward fire spread. While some flame “pulsation” have been studied in the past, such as the intermittent “puffing” of pool fires under stagnant conditions, this behavior is different from what is observed from wind-driven configurations. The puffing frequency of the pool fires has, however, been found to correlate well with the diameter of the fire source. These experiments on buoyant plumes suggest that puffing is primarily a result of a buoyant flow instability, which involves a strong coupled interaction between the buoyant plume and a toroidal vortex formed a short distance above the burner surface. This scaling has also been represented as a Strouhal–Froude relationship  $St \sim Fr^{-0.5}$ . In wind-driven fires, the pulsation of the flame will probably not scale with burner size in the same way as fires under stagnant conditions, as the wind velocity, which is a critically important element in the flame movement, is not included in the formulation.

In the previous chapter, the local total heat flux distribution on the downstream surface of wind-driven line fires was investigated and a local Richardson number ( $Ri_x = Gr_x / Re_x^2$ , flame buoyancy over wind momentum) was employed to scale the measured non-

dimensional heat fluxes. The average flame attachment length was also found to be linearly related to the local  $Ri_x$ . Those experiments represented a first step toward understanding the behavior of spreading wind-driven fires. However, only time-averaged quantities were reported, which would be able to help estimate the amount of heat that can be received by the downstream unburnt fuel by a given time, thus helping to further understand the fuel ignition and fire spread in wind-driven flames.

In this study, a stationary, non-spreading gas-burner fire configuration was chosen as it allows for a thorough statistical analysis of the flame structure. Long-duration experiments allow for a large sample size and more control over variations in experimental parameters, such as decoupling the heat-release rate of the fire from flow conditions, unachievable in spreading fires. The flame zone depth in the direction of fire spread can also be carefully adjusted via the size of the burner. High speed video is useful on these fires to reveal and track buoyant instabilities in the fire flow which resemble those appearing in spatially-uniform fuel beds [10]. The same intermittent movements observed in the fuel bed experiments were observed with the stationary burner, but with the ability to collect a larger data set. The flame forward and downward pulsation of wind-driven line fires will be studied, respectively to shed light into the ignition of unburnt fuels by flame contact and thus the fire spread. The flame forward pulsation frequency will be extracted from flame videos using the VITA method, while the local flame-fuel contacting frequency on the downstream surface will be obtained through a FFT of heat flux sensor data. Scaling laws will be developed for these two frequencies respectively and equations will be derived to correlate the frequency with related controlling parameters.

## 6.1 Flame Forward Pulsation Frequency

The flame forward pulsation was measured for stationary burners under wind. The flame location was determined using side-view high speed videos. Each image in the video was cropped to the same region-of-interest, a region defined from the downstream edge of the burner surface to the end of the image in the downstream direction, with a certain height above the surface. This region, in theory, could represent a fuel bed depth in a spreading fire (see the dashed rectangle in Fig. 44). Flame images were then converted to greyscale images in MATLAB by averaging all three color channels, and a threshold applied to result in a black-and-white image of flame and no-flame regions. As shown in Fig. 44, the flame position and flame shape are constantly changing when there is a perpendicular wind. The flame location is determined in the region of interest by tracking the furthest downstream tip of the flame detected from thresholding. This location fluctuates in time and would “burst” or quickly enter into what would be the unburnt fuel region, resulting in the intermittent heating of unburnt fuels by flame contact.

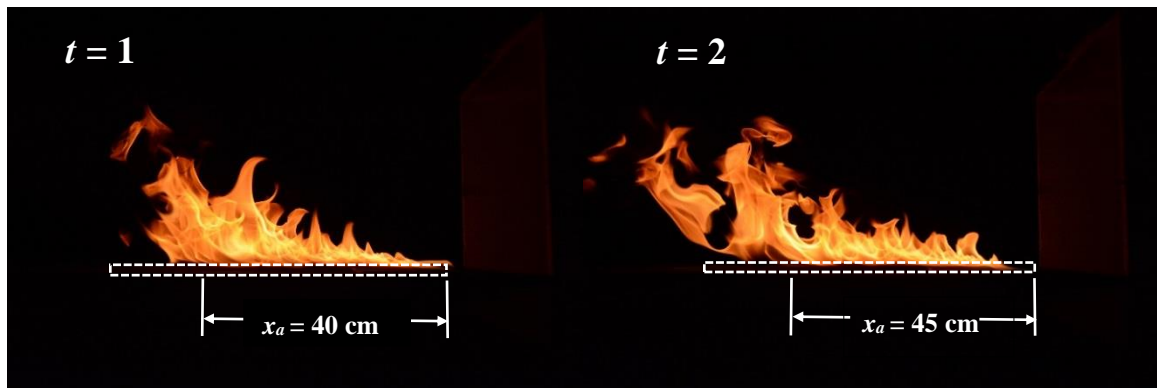


Figure 44. Flame location between two time steps in a forced flow experiment

Resultant flame locations as a function of time, shown in Figure 45, were analyzed using the VITA method. Level-crossing was only considered in the technique for the forward

direction, thus only when the flame was not at a location in the previous time step, and then appeared at the next time step, was it considered a crossing to avoid double-counting. The resulting flame forward pulsation frequency was then determined at each downstream location by dividing the number of crossings by the total number of frames, multiplied by the frame rate of the video. For this study, a 1 cm crop box height was used as the region of interest, as shown in Fig. 44. Other heights up to 4 cm were also tried, however the results were found to follow the same scaling shown here regardless of the height, with only their absolute values adjusting slightly. The mean values of the frequency data obtained from all the thresholds was used for later analysis. To connect results eventually to real flame spread, a fuel bed height will need to be defined for the scenario at hand.

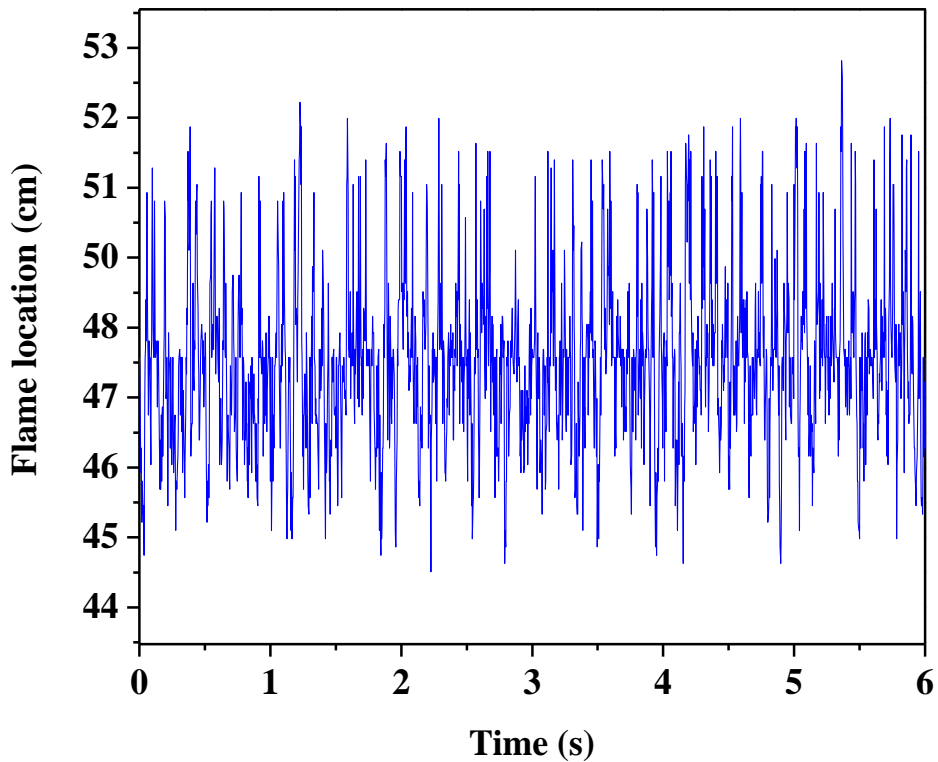


Figure 45. Fluctuating heat flux signals over time

Figure 46 shows resultant frequencies following application of the VITA technique. As can be seen, the frequency is initially 0 within the continuous flame region nearer to the burner, but as the flame intermittently moves forward and backwards, it enters and leaves the unburned region producing a parabolic profile of frequencies. A maximum frequency therefore occurs between the continuous flame region and the maximum forward extension of the flame, indicated in Figure 46. The frequency at this location is used in the analysis as a maximum representative frequency of the flame along the surface.

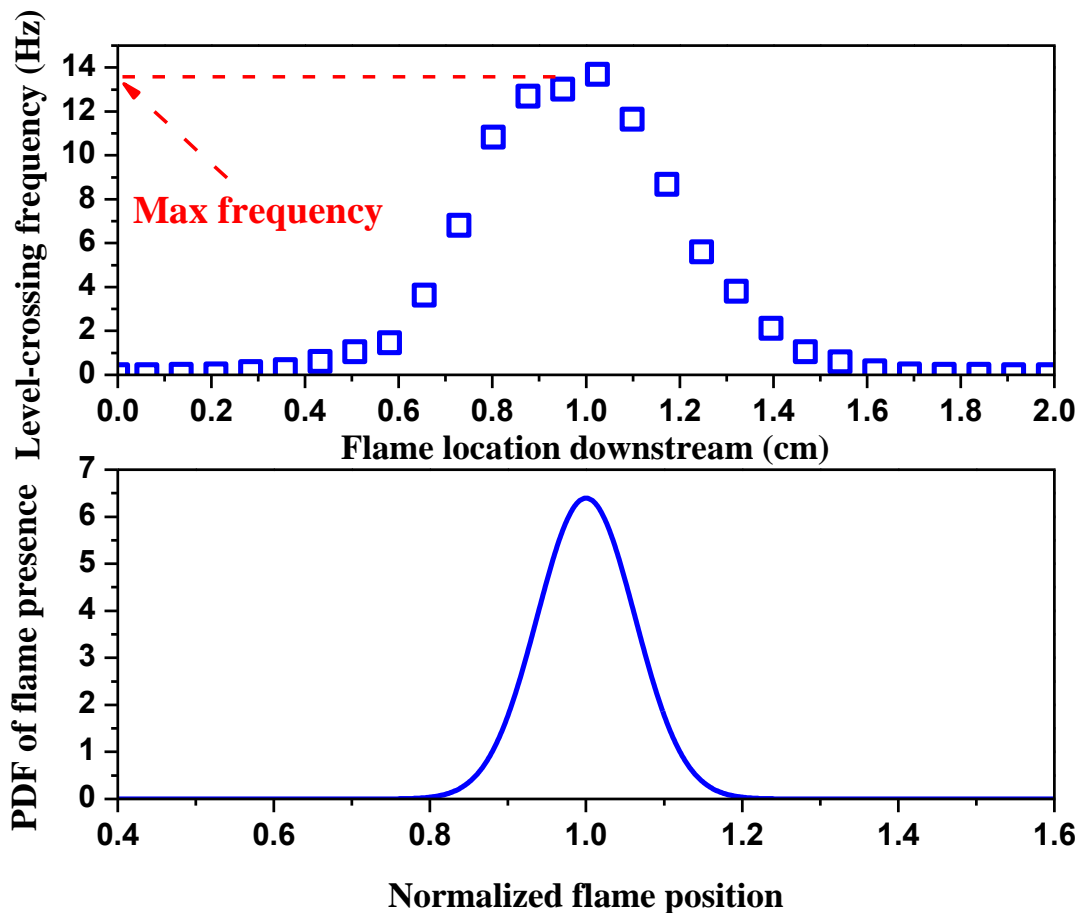


Figure 46. Level-crossing frequency and Probability Density Function (PDF) shows the flame locations on the downstream surface (7.9 kW, 2.45 m/s)

Applying the VITA method to all fire sizes and wind velocities, maximum frequencies are extracted, shown in Fig. 47. It shows that the flame pulsation frequency increases relatively linearly with the wind velocity, while it decreases with fire size in all the experiments tested. The frequencies observed range from less than 10 Hz to about 15 Hz.

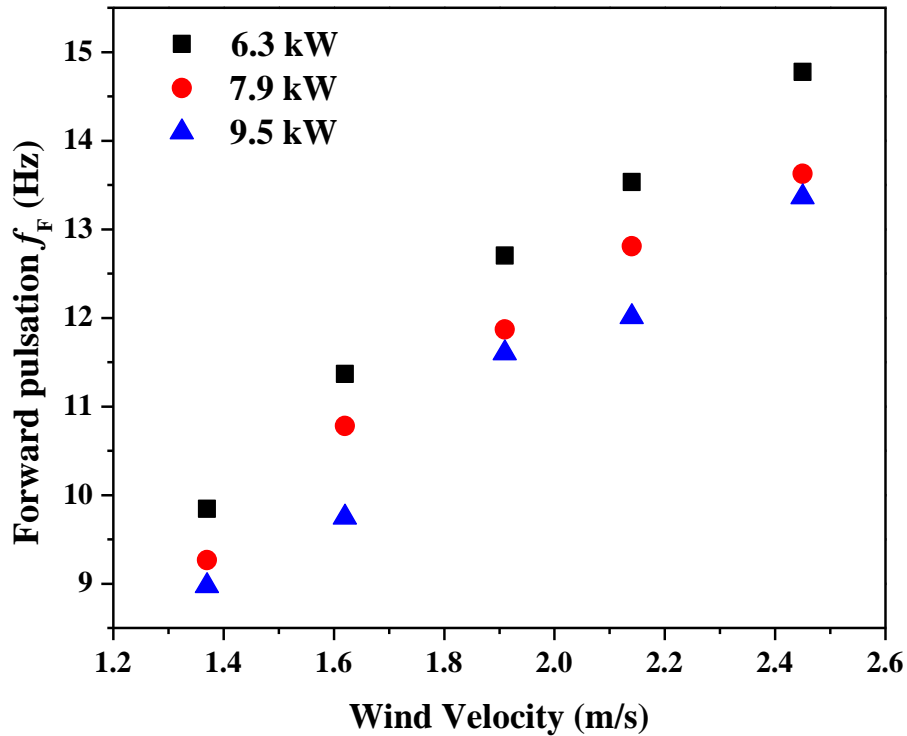


Figure 47. Forward pulsation frequency with different wind velocities and fire size

For the flame forward pulsation frequency, it is thought to be the result of competition between the forward momentum of the ambient wind and buoyancy from the flame itself. A scaling analysis can be performed, assuming relevant parameters, which reveals two primary groups that the forward pulsation frequency is dependent on, the Froude number (wind momentum over inertial force) and  $Q^*$  (buoyancy). A phenomenological explanation can be arrived at by first assuming the flame forward-pulsation frequency can be related to

both the ambient wind velocity,  $u$  and the flame length,  $l_f$ , which characterizes buoyancy from the fire, as

$$f_F \sim \frac{u}{l_f} \quad (31)$$

In a wind-driven fire, the flame length has previously been found to be a function of the wind velocity and mass burning rate in the form [110, 111],

$$\frac{l_f}{D} = A \left( \frac{\dot{m}''}{\rho_a \sqrt{gD}} \right)^B \cdot (u^*)^C \quad (32)$$

where  $D$  is the characteristic diameter or length of the burner,  $\dot{m}''$  the mass burning rate of the fire, and  $A$ ,  $B$ , and  $C$  are constants, previously found to be 62, -0.044, 0.25, respectively for gas diffusion flames [111]. A non-dimensional velocity can be defined as a ratio of the ambient wind velocity and a characteristic buoyant velocity of the fire,

$$u^* = \frac{u}{(g\dot{m}''D / \rho_a)^{1/3}} \quad (33)$$

where  $g$  is the acceleration due to gravity and  $\rho_a$  the density of ambient air. Assuming the fuel burns completely,  $\dot{m}''$  can be related to the heat-release rate of the fire,  $\dot{Q}$  as

$$\dot{Q} = \Delta H_c \cdot \dot{m}'' \quad (34)$$

which provides a more functional and universal parameter from which to define the fire.

The heat-release rate can be non-dimensionalized as  $Q^*$  [112] for a fire plume and expressed in terms of  $\dot{m}''$  as

$$Q^* = \frac{\dot{Q}}{\rho_a T_a C_p \sqrt{gD^5}} \sim \dot{m}'' \quad (35)$$

Combining equations (1-5), we arrive at equation (6), which relates the flame forward-pulsation frequency with the Froude number and the non-dimensional heat-release rate,

$$f_F \sim \frac{u^{1.044}}{Q^{*0.265}} \approx \frac{Fr^{1/2}}{Q^{*1/4}} = \sqrt{\frac{Fr}{Q^{*1/2}}} \quad (36)$$

The flame forward pulsation frequency data is then plotted against this parameter derived above in Figure 48, and a power-law relationship is found relating them as shown in Equation (37),

$$f_F = 12.9 \left( \frac{Fr^{1/2}}{Q^{*1/4}} \right)^{0.7} = 12.9 \left( \frac{Fr}{Q^{*1/2}} \right)^{0.35} \quad (37)$$

It shows that the correlation between flame forward pulsation frequency and  $Fr / Q^{*1/2}$  can be well correlated in an equation, with an  $R^2$  very close to 1, indicating an excellent fit. Thus with Eq. 37, one can well estimate the flame forward pulsation frequency using more basic and more achievable fire parameters and mean flame measurements, including the fire heat release rate and Fr number.

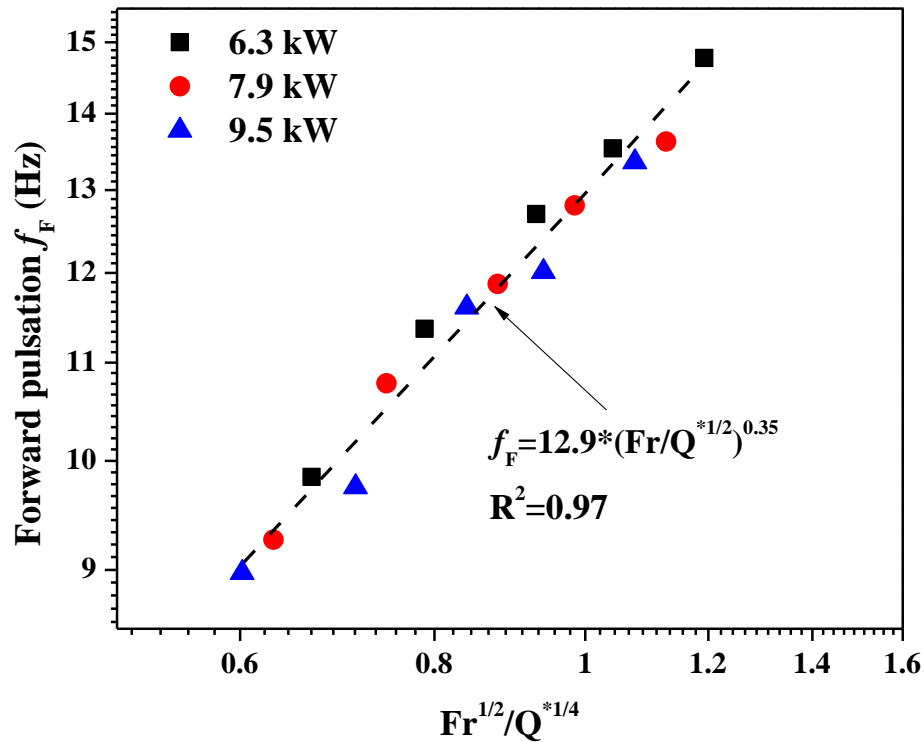


Figure 48. Flame forward pulsation frequencies are found to scale with  $Fr^{1/2}/Q^{*1/4}$

## 6.2 Flame-fuel Contact Frequency

The flame-fuel contact frequency can help determine how much heat flux can be received by unburnt fuels ahead of the flame through direct flame contact, which has recently been found to be a primary mechanism of ignition of fuels in a wind-driven wildland fire [10]. For each of the experimental conditions mentioned in Table 1, raw heat flux signals were taken at different locations on the downstream board. The flame-fuel contact frequency can be extracted from measured heat flux signals, such as the one shown in Figure 49 (top), by applying a FFT which results in a frequency spectrum, on the bottom, which has a peak at about 2 Hz.

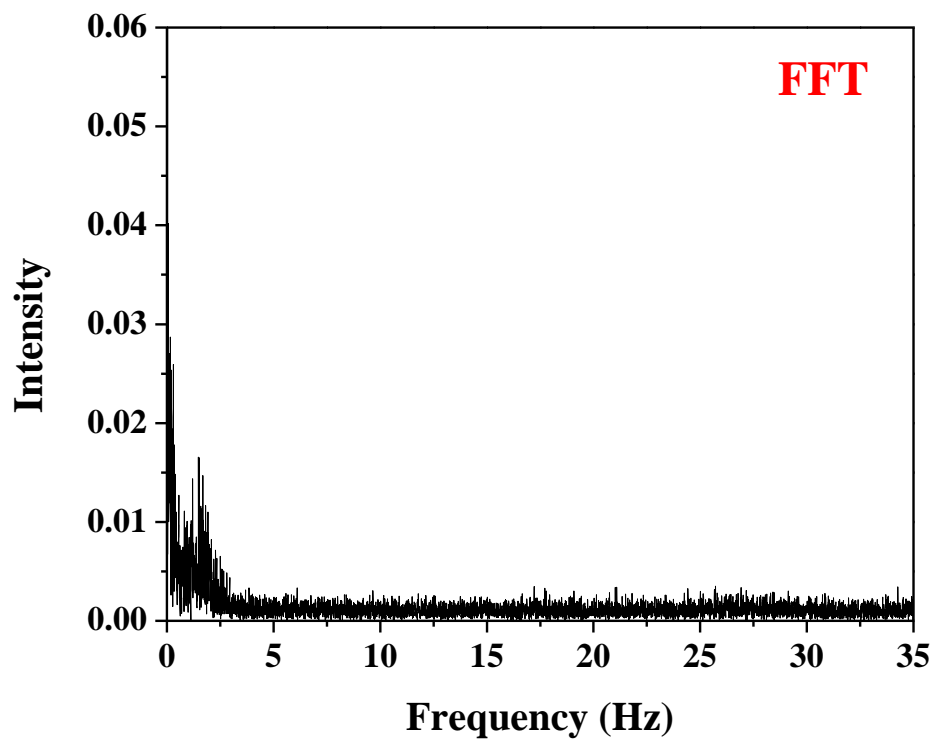
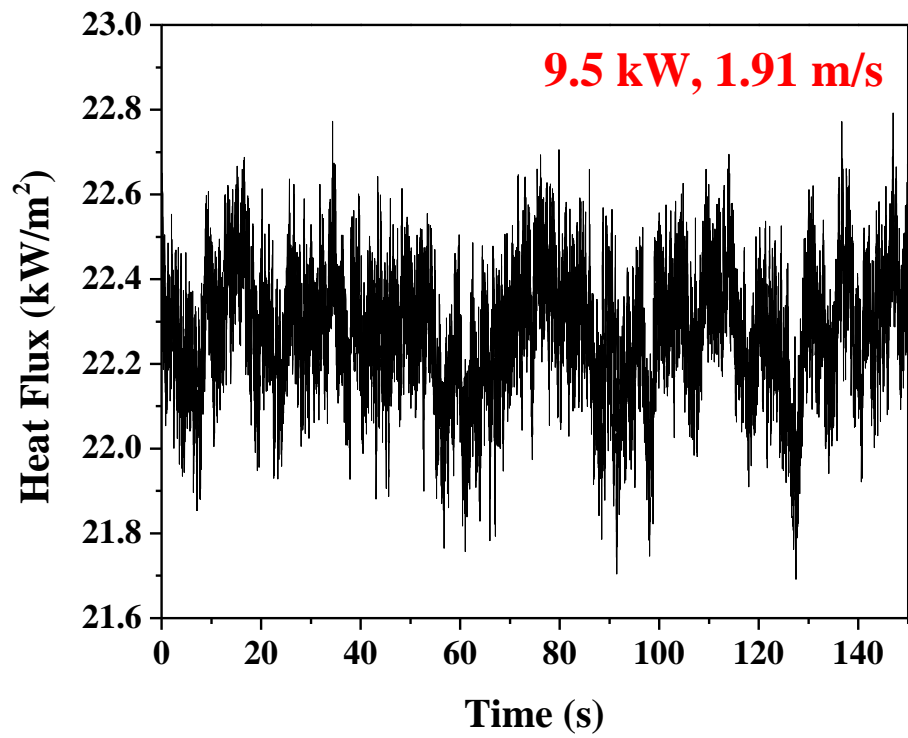


Figure 49. Heat flux raw data at 11 cm, with 9.5 kW fire size, 1.91 m/s wind velocity, and frequency spectrum obtained from FFT

The same method is applied to three cases with different wind velocities but the same fire size (9.5 kW) at 11 cm downstream, shown in Figure 50. The FFT is smoothed using a Savitzky–Golay filter and the peak intensity used to choose the peak frequency at that location. In Figure 49, it can be seen that the flame-fuel contact frequency slightly increases with increasing wind velocity, however the intensity of this peak decreases.

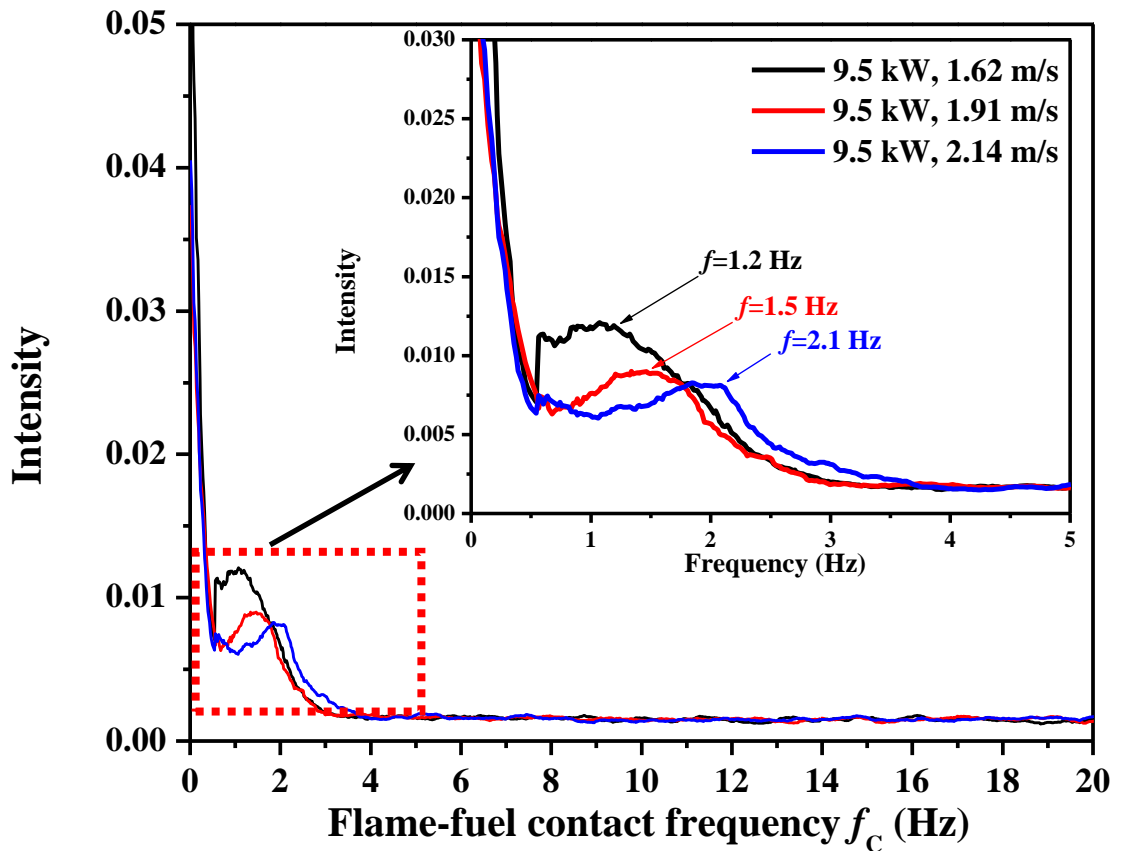


Figure 50. Comparison of frequency obtained from the FFT for different wind velocities.

The local flame-fuel contact frequency was further plotted for different wind velocities and fire sizes. Figure 51 shows one example where the fire size is 7.9 kW, with the local frequency at different locations plotted and compared. The figure shows how, for a given wind velocity, the local frequency tends to go down with downstream distance from the burner.

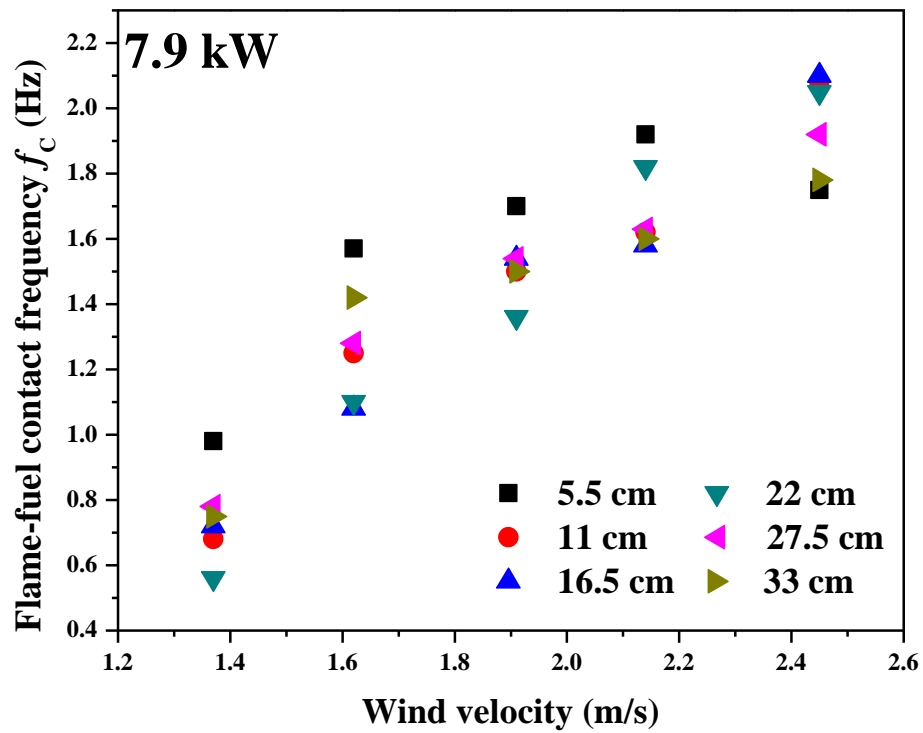


Figure 51. Local flame fuel contact frequency for 7.9 kW under different wind velocities

Previously, the flame puffing frequency without wind has been found to be only a function of burner size. Under wind conditions, however, two directional flame pulsations are clearly observed. One is the forward pulsation, where the flame is driven by the wind and moves back and forth in the stream-wise direction. The other is the upward pulsation,

which is found to be really a local phenomenon, where flame is touching and transferring heat to the local unburnt fuel within the attachment and intermittent regions. This section will discuss these two pulsation frequencies and their correlations with related parameters. For the local flame-fuel contacting frequency, following our previous work on the local heat flux distribution on the downstream surface in wind-driven line fires. The local Grashof ( $Gr_x = g\beta(T_h - T_\infty)L^3 / \nu^2$ ) and Reynolds ( $Re_x = UL/\nu$ ) numbers arise as critical parameters describing the flow and heat transfer in our setup, where  $T_h$  and  $T_\infty$  are the hot gas and ambient temperatures, respectively,  $L$  is the characteristic length,  $g$  the acceleration due to gravity,  $\beta$  the thermal expansion coefficient, and  $\nu$  the kinematic viscosity of the ambient air. The relative role of buoyancy and inertial forces in the flow have been found to be well-described by comparing the relative influence of these two parameters, often determined to be  $Gr_x / Re_x^a$ , with a varying constant  $a$ .

In a flame scenario with forced air flow, the Richardson number, with the exponent on  $Re_x$  determined as 2, was defined as:

$$Ri_x = \frac{Gr_x}{Re_x^2} = \frac{g\beta(T_f - T_\infty)L}{U^2} \quad (38)$$

$Ri$  was used to represent the ratio between natural convection (controlled by the buoyancy of the flame) and forced convection (controlled by the forced air flow velocity), and instead of using the temperature of the hot gas, the flame temperature  $T_f$  was used. The flame was then divided into regions to describe flame attachment and liftoff that shown in Eq. 19.

Inertial forces would be expected to dominate the flame behavior when  $Ri_x < 0.1$  and buoyancy forces dominate when  $Ri_x > 10$ . However, the details and implications of the heat transfer modes in the mixed regions ( $0.1 < Ri_x < 10$ ), where the transition from an inertial-

dominant to buoyancy-dominant regime, has not been well studied. Because most fires with cross air flow scenarios reside in this region, seen visually with flames that begin attached near the surface and tend to “lift off” into a more plume-like scenario downstream, study of the fire behavior in this region will help improve understanding of the flame spread mechanisms. The Local  $Ri_x$  is calculated using equation 18 and plotted against the downstream distance,  $L$ . Figures 26 and 27 shows several examples of the local  $Ri_x$  trends with downstream distance. An increasing trend is seen with increasing downstream distance, although the patterns for different wind cases are different from one another other. In Chapter 4, it was found that the local  $Ri_x$  was a good indicator to collapse the local heat flux distribution along the downstream surface. Here we also apply this method to the frequency study and come up with one way to quantify and predict the local flame-fuel contacting frequency trend with local  $Ri_x$  number.

A non-dimensional flame-fuel contacting frequency  $f_c^+$  is proposed based on a characteristic gas fuel flow rate and downstream distance,

$$f_c^+ = \frac{f_c L^+}{u^+} \quad (39)$$

$$u^+ = (g\dot{m}''D / \rho_a)^{1/3} \quad (40)$$

where  $f_c$  is the raw frequency data we obtained from heat flux gauge sensor,  $L^+$  is the downstream distance from the measuring point to the leading edge of the burner chosen as characteristic length scale,  $u^+$  is the characteristic fuel velocity based on mass loss rate,  $\dot{m}''$  is the mass flow rate,  $D$  the burner hydraulic diameter, and  $\rho_a$  the air density.

Note that this non-dimensional flame-fuel contact frequency is not a typical Strouhal number as has been previously defined in pool fire studies. St-Fr correlations have been

found for pool fire puffing frequencies under stagnant conditions, where only natural convection (buoyancy) is controlling the flame behavior, and the length scale chosen for the study was pool diameter. This appears to be more of a global instability of the system driven by buoyancy. In our study, we introduced forced convection (wind), and the length scale is chosen as the distance from the measuring point to the leading edge of the burner, where the thermal boundary layer starts to develop. The length scale chosen in this paper follows the approach in Chapter 4.1 on the effect of forced and natural convection on heat flux distribution in wind-driven line fires.

In Figure 52, the local  $Ri_x$  is plotted against the non-dimensional frequency. When  $Ri_x$  is smaller than 1,  $f_c^+$  does not change much, however after  $Ri_x$  reaches 1,  $f_c^+$  starts to decrease with  $Ri_x$ . A piece-wise function was obtained based on correlated data to describe the local frequency trend with  $Ri_x$ . Equation 41 indicates that, in a wind-driven fire, the flame-fuel contact frequency before the local  $Ri_x$  reaches 1 will remain unchanged, fluctuating around 0.7. After  $Ri_x$  reaches 1, which means natural convection and forced convection approximately balance each other,  $f_c^+$  will decrease with  $Ri_x$  in a power law trend as  $f_c^+ = 0.7Ri_x^{-0.78}$ .

$$f_c^+ = \begin{cases} 0.7 & Ri_x < 1 \\ 0.7Ri_x^{-0.78} & Ri_x > 1 \end{cases} \quad (41)$$

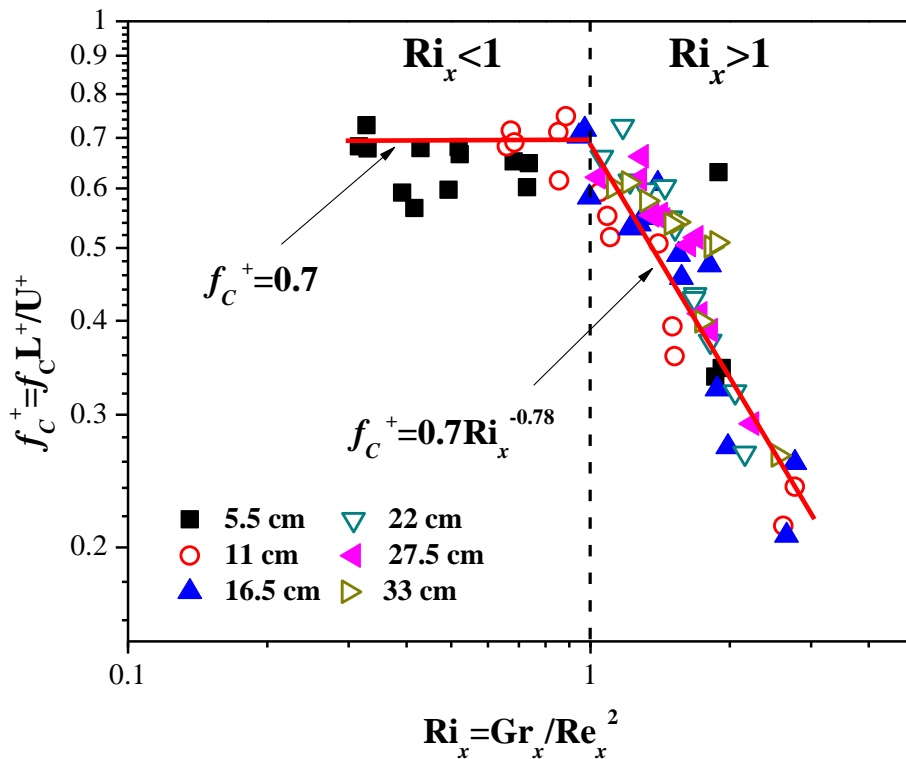


Figure 52. Non-dimensional frequency  $f_c^+$  versus local  $Ri_x$

### 6.3 Discussions and Conclusion

The flame forward pulsation frequency and local flame-fuel contact frequencies were discussed in this section, as they represent two directions of the flame movement in a wind-driven fire scenario. The flame forward pulsation frequency describes how frequently the flame will move back and forth under certain fire sizes and wind velocities, indicating the potential of the flame to reach unburnt fuels on the downstream surface. It has been found to be the result of competing mechanisms of buoyancy of the flame and the wind momentum. A scaling analysis with Froude number and the non-dimensional heat release rate has been proposed to correlate the flame forward pulsation frequency.

In order to study the heating process of the fuels under attached and intermittent regions of the flame, the local flame-fuel contact frequency has been studied from measured heat flux signals. The local flame-fuel contact describes how frequently the flame “touches” the unburnt fuel surface under the flame attachment and intermittent regions, shedding light on how the unburnt fuels are actually being heated and ignited by direct flame contact, thus providing critical information for the prediction of flame spread. This frequency is thought to primarily be due to local flame buoyancy, although the distribution of this frequency has a relationship with the flame length (the three flame regions mentioned in Fig. 1). A local  $Ri_x$  number analysis has been performed to represent the distribution of this frequency, following our previous analysis on the local heat flux distribution on the downstream surface.

Experiments were conducted on a variety wind-driven line fires where the intermittent behavior of the flame was studied. Both the flame forward-pulsation frequency and flame-fuel contact frequency were independently measured. Trends in these quantities were reviewed and non-dimensional scaling proposed for each. It was found that flame forward pulsation frequency  $f_F$ , which could indicate the potential of the flame reaching out unburnt fuels on the downstream surface, can be well correlated and predicted by a non-dimensional parameter,  $Fr/Q^{*1/2}$  in a power law trend. The mechanism of this forward pulsation has been found to be related to the competition of wind momentum and flame buoyancy. For the flame-fuel contacting frequency, which tells the local heating process of the flame to the unburnt fuels on the flame attachment and intermittent regions. A piecewise function was found between the non-dimensional  $f_c^+$  with local  $Ri_x$ , indicating that

when  $Ri_x < 1$ , non-dimensional flame contact frequency  $f_c^+$  remains approximately constant, when  $Ri_x > 1$ , it decreases with  $Ri_x$ . The information of flame forward pulsation frequency and local flame-fuel contact frequency, and their correlations with concerning parameters will help explain the wildland fire fuel ignition and flame spread.

## Chapter 7: Conclusions

In this work, a thorough experimental work has been conducted on the wind-driven line fires. Detailed information connecting intermittent fluctuations of the flame to fuel heating processes have been investigated. The local heat flux distribution on the downstream surface, intermittent pulsation frequencies of the flame, the flame extension length and flame attachment region have been studied in detail.

First, the local total heat flux from a wind-driven line fire on the downstream surface was found to have different profiles for different wind speeds and fire sizes. When the wind speed is low, the heat flux decreases with downstream distance, while with a high wind speed, the heat flux first increases to a maximum value, then decreases. The location where the maximum local heat flux received by the downstream surface in a forced flow flame roughly matches the location where the local  $Ri_x=1$ . The dimensionless local total heat flux was then correlated with downstream location in a piece-wise function based on the Richardson number, breaking up the correlation between the attached and plume regions. The visually-observed flame attachment length was also found for each test, and linear correlation was found between this length and  $Ri_x$ . Information between the flame attachment length and local  $Ri_x$  are able to help estimate the downstream location where it receives the most heat flux from a turbulent diffusion flame, and also where the flame starts to rise up and eventually enter plume region, thus shedding light on flame spread mechanisms downstream.

A time-dependent view of the flame was also taken, observing the flame forward pulsation frequency  $f_F$ , which indicates the potential of the flame reaching out to unburnt fuels on the downstream surface past the average extent of the flame, can be well correlated and

predicted by a non-dimensional parameter,  $Fr/Q^{*1/2}$ , following a power law trend. The mechanism of this forward pulsation has been found to be related to the competition of wind momentum and flame buoyancy. For the flame-fuel contact frequency, which describes the local heating process of the flame to the unburnt fuels within the flame attachment and intermittent regions. A piece-wise function was found between the non-dimensional  $f_c^+$  with local  $Ri_x$ , indicating that when  $Ri_x < 1$ , the non-dimensional flame contact frequency  $f_c^+$  remains approximately constant and when  $Ri_x > 1$ , it decreases with  $Ri_x$ . Information on the flame forward pulsation frequency and the local flame-fuel contact frequency, as well as their correlations with concerning parameters will be useful in the future to develop models for wildland fire fuel ignition and flame spread.

The extension length of the flame has also been studied as a function of time. For increasing ambient wind velocities, flames are found to intermittently extend further downstream from the mean flame front, when measured along the surface. This means a longer region of flame contact with unburnt fuels would result during flame spread, increasing flame spread rates. The maximum frequency position is also found to be linearly related with the horizontal flame length along the fuel surface, indicating that periodic properties of the flame could be estimated from mean flame measurements and wind speeds. The variance ( $\sigma^2$ ) of the mean flame attachment length is also found to be sensitive to  $Fr^{2/3}/Q^*$ . The attachment length and intermittency characteristics of flames are critical factors in heating and ignition of fine fuel particles in wildland fires. Further study of the mechanisms leading to forward pulsations of the flame front are needed to more carefully determine the influence of these mechanisms on flame spread through wildland fuels.

## Chapter 8: Future Work

This study presented a first look at the behavior of stationary wind-driven flames and their time-dependent behavior. Based on what was found, there is a large amount of future work to explore in the area. First, tests with a large fire size and high wind velocity should be introduced, as only small fire sizes (~10 kW) and relatively low wind velocities (~2 m/s) have been employed in this project. In real wildland fires, the fire size will be much larger and turbulent. The flames in this study are, at best, transitionally turbulent, so this may limit their application. Data from larger fire sizes and a range of wind velocities should be collected and compared with our existing data, seeing whether the data and experimental observations can scale with size.

The proportion of radiation vs. convection is also an important aspect that should be studied for its use in determining future models for flame spread, especially at larger scale. The local convective and radiative components can be calculated with either sapphire-window radiometers or estimated using the local temperature gradient. This information is important in that it will show a more direct picture of the fuel heating process, how much of the total heat flux is radiant heat, and how much is convective heat, shedding further light onto the heating and ignition of fuels in wind-driven fire spread.

The mechanisms governing the frequencies observed for both forward pulsations of flames and flame-fuel contact are still not fully understood. Preliminary results have already shown that the frequency of wind-driven line fires are less than in stagnant situations. But the reason for this decrease in frequency is not fully understood. Probing detailed numerical simulations of the situations studied and/or development of theory to describe this behavior may be useful to further elucidate the mechanisms responsible.

Further improvements to the experiments can also be made. Further characterization of the incoming flow may be useful for validation of numerical models. Further aspect ratios of the burner would also be useful, but that will require a larger wind tunnel. The resolution of the heat flux data may also be improved by employing a smaller diameter heat flux gauge.

In these experiments, flame spread behavior was studied on a flat plane, where the wind is flush with the surface. In real wildland fires, there could be many different geometries, for example, the flame can spread over an inclined surface, or the flame can spread in canyons. The fire behavior in these inclined geometries can be very different compared with flame spread over flat surfaces due to changes in entrainment, although the mechanisms may be similar. In later experiments, variations of these geometries will be undertaken to gain more insight into the processes governing wildland fire spread.

## Published Journal/Conference articles

1. **Wei Tang**, Colin Miller, Michael Gollner, Local Flame Attachment and Heat Fluxes in Wind-Driven Line Fires, *Proceedings of the Combustion Institute*, Volume 36, Issue 2, 2017, Pages 3253-3261.
2. **Wei Tang**, Daniel Gorham, Mark Finney, Sara McAllister, Jack Cohen, Jason Forthofer, Michael Gollner, Intermittent heating and flame extension in wind-driven fires, *Fire Safety Journal*, in press.
3. Colin Miller, **Wei Tang**, Mark Finney, Sara McAllister, Jason Forthofer, Michael Gollner, An investigation of coherent structures in laminar boundary layer flames, *Combustion and Flame*, Volume 181, July 2017, Pages 123–135.
4. Cong Zhang, Mélanie Rochoux, **Wei Tang**, Michael Gollner, Jean-Baptiste Filippi and Arnaud Trouvé. Evaluation of a data-driven wildland fire spread forecast model with spatially-distributed parameter estimation in simulations of the FireFlux I field-scale experiment, *Fire Safety Journal*, in press.
5. Michael Gollner, Colin Miller, **Wei Tang**, Ajay Singh, Recent developments in concurrent flame spread, *Fire Safety Journal*, in press.
6. **Wei Tang**, Mark Finney, Sara McAllister, Michael Gollner, An experimental study of the intermittent heating frequencies of wind-driven line fires. Preparing.
7. **Wei Tang**, Daniel Gorham, Michael Gollner, Jason Forthofer, Mark Finney, Forward pulsation behavior of wind-driven line fires, *9th U. S. National Combustion Meeting*, May, Cincinnati, Ohio.

8. **Wei Tang**, Mark Finney, Sara McAllister, Michael Gollner, An experimental study of the flame intermittent frequencies of wind-driven line fires, *10th U. S. National Combustion Meeting*, April, College Park, Maryland.
9. Gollner, M.J., **Tang, W.**, Gorham, D.J., Finney, M.A., McAllister, S., Cohen, J. and Forthofer, J., Dynamic Behavior and Structure of Wind Blown Flames, *25th International Colloquium on the Dynamics of Explosions and Reacting Systems*, August 2-7, Leeds, UK, 2015.7-20, 2015.
10. Cong Zhang, Mélanie Rochoux, Annabelle Collin, Philippe Moireau, **Wei Tang**, Michael Gollner, Evan Ellicott, Arnaud Trouvé. Front Shape Comparison in Data-Driven Wildland Fire Spread Simulations, *10th U. S. National Combustion Meeting*, April, College Park, Maryland.
11. Kun Zhao, Lizhong Yang, **Wei Tang**, Michael Gollner, Experimental and theoretical study on downward flame spread over two parallel PMMA slabs in different pressure environments, *10th U. S. National Combustion Meeting*, April, College Park, Maryland.
12. Colin Miller, Mark Finney, Sara McAllister, Torben Grumstrup, Evan Sluder, **Wei Tang**, Michael Gollner, Investigating streak-like structures in boundary layer combustion via heated plates, *10th U. S. National Combustion Meeting*, April, College Park, Maryland.

## Appendix A: Convective and radiative heat flux

In this section, we will discuss the convective and radiative heat flux components from the total incident heat flux received by the downstream surface. Radiation can be directly measured by a Medtherm radiometer, which is described in previous experimental setup part. Convection, however, can be calculated or estimated based on the temperature gradient on the board surface.

$$\dot{q}_{fl,c}'' \approx h(T_{fl} - T_w) \approx k_f \frac{(T_{fl} - T_w)}{y_f} \quad (42)$$

in which,  $\dot{q}_{fl,c}''$  is the gas phase convective heat flux, or we can further estimate the convective heat flux as

$$\dot{q}_{fl,c}'' = k_w \left( \frac{dT}{dy} \right)_{y=0}. \quad (43)$$

To calculate the convective heat flux, fine resolution temperature profiles near the insulation board surface can be measured. For example, for one measuring location with one wind velocity and fuel flow rate, six points were measured in a vertical direction with 0.4 mm in spacing. An average temperature data was taken for three repeated measurements. Figure 53 below shows the temperature profile for a given fire case, with a fire size of 7.9 kW and wind velocity 2.14 m/s. Here, we can see there is a high temperature gradient on the board surface close to the burner, and with further locations away from the burner, the temperature gradient decreases. This can be explained by the flame attachment process, when the flame is attached the near burner surface and temperature gradient and convection at the surface is very high. When the flame lifts up at further downstream

locations, the local temperature gradient becomes less obvious, and convection in that region plays less of an important role.

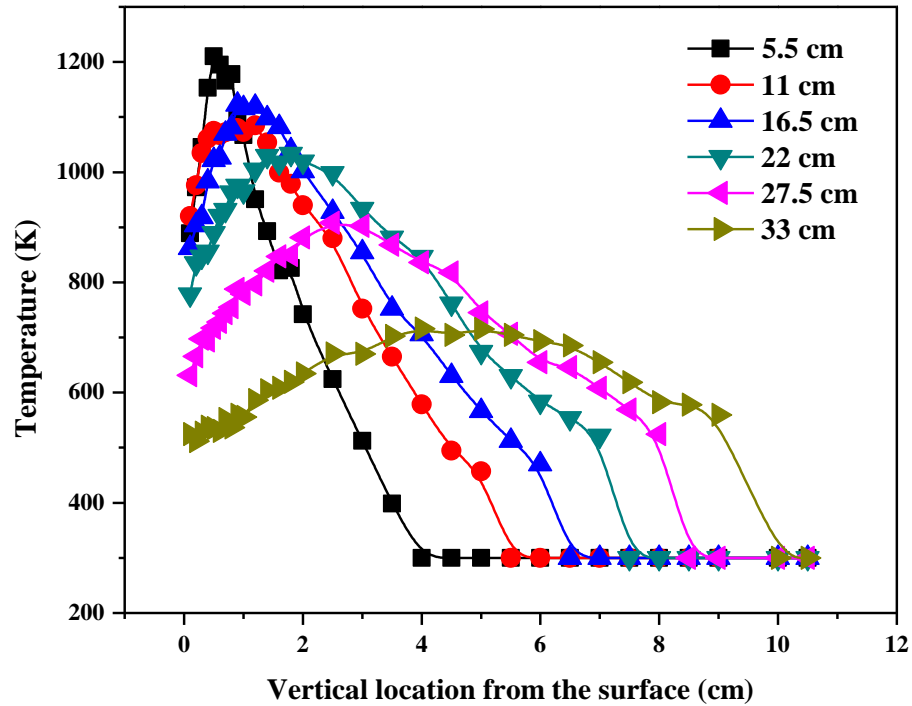


Figure 53. Temperature distribution on the downstream board with fire size 7.9 kW, wind velocity 2.14 m/s

The data was further analyzed, interpolating the temperature profile, shown in Figure 54..

From this figure, we could also see the temperature gradient difference in the near and far locations on the downstream surface. In the near-field of the burner, the local temperature gradient is much higher than in the far field.

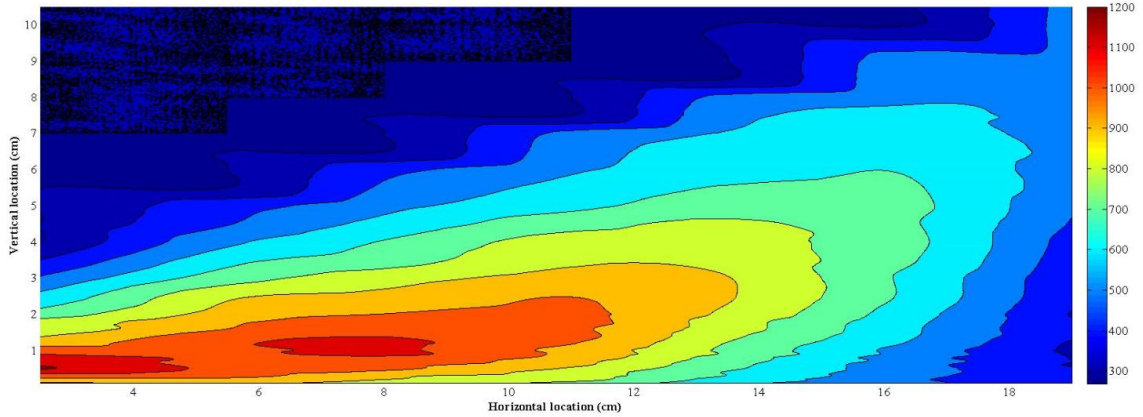


Figure 54. Interpolation of the temperatures measured above the downstream surface

Figure 55 below shows the temperature gradient profile for one case (wind velocity 2.14 m/s, fire size 6.3 kW, and measurement location 5.5 cm from the trailing edge of the burner). It can be seen that a large temperature gradient appears at the board surface. The local temperature is first estimated by fitting the data points and a gradient at the surface calculated from the derivative of this fit at the board surface,

$$T' = T'(y) \Big|_{y=0} . \quad (44)$$

The local temperature gradient at the surface is about  $4.9 \times 10^5$  K/m and thermal conductivity for air at the film temperature, which is the mean temperature of the wall and the flame, is estimated as  $4.3 \times 10^{-5}$  kW/K.m. Thus, the local convective heat flux is

$$\dot{q}_{fl,c}'' = k_w \left( \frac{dT}{dy} \right)_{y=0} \approx 21.07 \text{ kW/m}^2 \quad (45)$$

Re-visiting the total heat flux data we had from the previous section, we noticed that the local heat flux for this fire case are about  $26 \text{ kW/m}^2$ . So, radiation in this region only provides less than 20% of the total heat flux. This makes sense for these small, laminar or

transitional flames. Information from previous studies also shows that convection in the near-field of the burner field is dominant within the boundary layer for laminar flames [52].

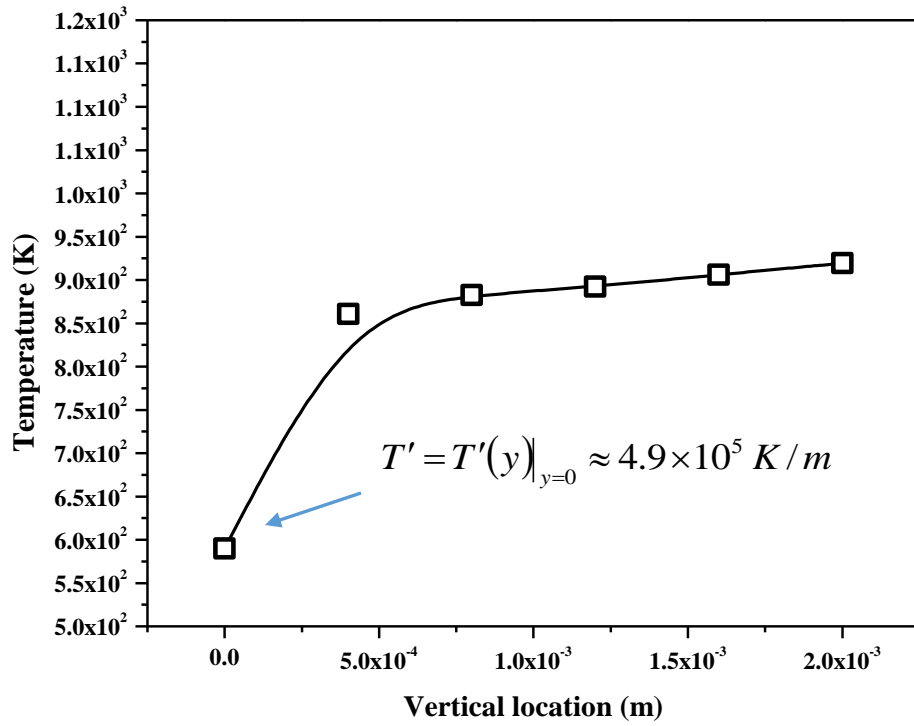


Figure 55. Temperature gradient at the surface

## Bibliography

- [1] Caton SE, Hakes RSP, Gorham DJ, Zhou A, Gollner MJ (2017) Review of pathways for building fire spread in the wildland urban interface part I: exposure conditions. *Fire Technol.* 53, 429–473.
- [2] Hakes RSP, Caton SE, Gorham DJ, Gollner MJ (2017) A Review of Pathways for Building Fire Spread in the Wildland Urban Interface Part II: Response of Components and Systems and Mitigation Strategies in the United States. *Fire Technol.* 53, 475–515.
- [3] Anthony L. Westerling, Monica G. Turner, Erica A. H. Smithwick, William H. Romme, and Michael G. Ryan (2011) Continued warming could transform Greater Yellowstone fire regimes by mid-21st century, *PNAS*, August 9, vol. 108, no. 32, 13165–13170.
- [4] Finney MA, Cohen JD, McAllister SS, Jolly WM (2013) On the need for a theory of wildland fire spread. *Int J Wildland Fire* 22(1):25–36.
- [5] Canfield JM, Linn RR, Sauer JA, Finney M, Forthofer J (2014) A numerical investigation of interplay between fire line length, geometry, and spread rate. *Agric For Meteorol* 189-190:48–49.
- [6] Adam BA, Akafuah NK, Finney MA, Forthofer J, Saito K (2014) A Study of Flame Spread in Engineered Cardboard Fuelbeds. Part II: Scaling Law Approach, *Progress in Scale Modeling* (Springer, Berlin/Heidelberg, Germany), Vol II, 85–95.
- [7] A. Putnam (1965) A model study of wind-blown free-burning fires, *Proc. Comb. Inst.* 10:1039–1046.

- [8] F.A. Albini (1982) Response of free-burning fires to non-steady wind. *Combustion Science and Technology* 29: 225-241.
- [9] Albini, F. A. (1981). A model for the wind-blown flame from a line fire. *Combust. Flame* 43, 155– 174.
- [10] Finney, M., Jack D., Jason M., Sara S., Michael G., Daniel G., Kozo S., Nelson A., Brittany A., Justin E. (2015) Role of buoyant flame dynamics in wildfire spread, *Pro. Natl Acad Sci.* 112, 32: 9833–9838.
- [11] Finney, Mark A. Cohen, Jack D. Grenfell, Isaac C. Yedinak, Kara M. (2010) An Examination of Fire Spread Thresholds In Discontinuous Fuel Beds. *International Journal of Wildland Fire.* 19: 163-170.
- [12] D. Gorham (2014) Studying wildfire spread using stationary burners. Thesis, University of Maryland.
- [13] R. Rothemel (1972) A Mathematical Model For Predicting Fire Spread In Wildland Fuels, USDA Forest Service Research Paper INT-115.
- [14] <http://activefiremaps.fs.fed.us/>
- [15] Mark A. Finney, Jason Forthofer, Isaac C. Grenfell, Brittany A. Adam, Nelson K. Akafuah, and Kozo Saito (2013) A Study of Flame Spread in Engineered Cardboard Fuelbed Part I: Correlations and Observations. Seventh International Symposium on Scale Modeling (ISSM-7) Hirosaki, Japan, Aug 6-9.
- [16] Rothemel, R.C. (1983) How to predict the spread and intensity of forest and range fires. USDA For. Serv. Gen. Tech. Rep. INT-143.
- [17] Anderson, H.E. (1983) Predicting wind-driven wildland fire size and shape. USDA For. Serv. Res. Pap. INT-305.

- [18] Rothermel, R.C. (1994) Some fire behavior modeling concepts for fire management systems. Proc. 12th conf. Fire and Forest Meteorology, 164-171.
- [19] A.C. Fernandez-Pello, T. Hirano (1983) Controlling Mechanisms of Flame Spread. Combust. Sci. Technol., 32, 1–31.
- [20] Michael Gollner, Colin Miller, Wei Tang, Ajay Singh (2017) The Effect of Flow and Geometry on Concurrent Flame Spread, Fire Safety Journal, in press.
- [21] Annamalai, K., M. Sibulkin. (1979) Flame Spread Over Combustible Surfaces for Laminar Flow Systems, Part II: Flame Heights and Fire Spread Rates, Combust. Sci. Technol., 19(5-6), 167–183.
- [22] Quintiere, J., Harkleroad, M., Hasemi, Y. (1986) Wall flames and implications of upward flame spread Combust. Sci. Technol., 48, 191–222.
- [23] K. Saito, J.G. Quintiere, F.A. Williams (1985) Upward turbulent flame spread Int. Assoc. Fire Saf. Sci. 75–86.
- [24] A. V. Singh, M. J. Gollner (2015) A methodology for estimation of local heat fluxes in steady laminar boundary layer diffusion flames, Combust. Flame, 162 2214–2230.
- [25] Mark A. Cochrane, Ane Alencar, Mark D. Schulze, Carlos M. Souza Jr., Daniel C. Nepstad, Paul Lefebvre, Eric A. Davidson. (1999) Positive Feedbacks in the Fire Dynamic of Closed Canopy Tropical Forests, Science 11:Vol. 284, Issue 5421, pp. 1832-1835.
- [26] Lönnermark, A., and Ingason, H. (2007) The Effect of Cross-sectional Area and Air Velocity on the Conditions in a Tunnel during a Fire SP Technical Research Institute of Sweden, SP Report 2007:05, Sweden.

- [27] Apte, V. B., R.W. Bilger, A. R. Green, J. G. Quintiere (1991) Wind-aided turbulent flame spread and burning over large-scale horizontal PMMA surfaces, *Combust. Flame* 85, 169–184.
- [28] J. Consalvi, Y. Pizzo, B. Porterie (2008) Numerical analysis of the heating process in upward flame spread over thick PMMA slabs, *Fire Saf. J.* 43 (5), 351–362.
- [29] K. Tsai, J. Turnbull, G. Will, D. Drysdale (2003) Upward flame spread: heat transfer to the unburned surface, *Fire Saf. Sci.* 7, 117–128.
- [30] M.J. Gollner, X. Huang, J. Cobian, A.S. Rangwala, F.A. Williams (2013) Experimental study of upward flame spread of an inclined fuel surface, *Proc. Combust. Inst.*, 34, 2531–2538.
- [31] A. C. Fernandez-Pello, (1979) Flame Spread in a Forward Forced Flow, *Combust. Flame* 36, pp. 63–78.
- [32] de Ris, J. L., Orloff, L., Ris, J. De, Orloff, L., de Ris, J. L., Orloff, L. (1975) The role of buoyancy direction and radiation in turbulent diffusion flames on surfaces, *Symp. (Intl) Combust.* 15, pp. 175–182.
- [33] Atkinson, G. G. T., Drysdale, D. D., Wu, Y (1995) Fire driven flow in an inclined trench, *Fire Saf. J.*, 25, pp. 141–158.
- [34] Xiao Chen, Jiahao Liu, Zhihui Zhou, Pan Li, Tiannian Zhou, Dechuang Zhou, Jian Wang (2015) Experimental and theoretical analysis on lateral flame spread over inclined PMMA surface, *International Journal of Heat and Mass Transfer* 91, 68–76.
- [35] Jafar Zanganeh, Behdad Moghtaderi, (2014) Investigation of flame propagation over an inclined fuel wetted porous bed. *Fire Safety Journal*, Volume 67, 113-120.

- [36] W. Tang, C.H. Miller, M.J. Gollner (2017) Local flame attachment and heat fluxes in wind-driven line fires, *Proc. Combust. Inst.*, 36 (2), 3253–3261.
- [37] Isaac T. Leventon, Stanislav I. Stoliarov (2013) Evolution of flame to surface heat flux during upward flame spread on poly(methyl methacrylate), *Proc. Combust. Inst.*, 34(2), 2523-2530.
- [38] Colin H. Miller, Michael J. Gollner (2015) Upward flame spread over discrete fuels, *Fire Safety Journal*, Volume 77, 36-45.
- [39] M.J. Gollner, F.A. Williams, A.S. Rangwala (2011) Upward flame spread over corrugated cardboard, *Combustion and Flame*, Volume 158, Issue 7, 1404-1412.
- [40] Xinjie Huang, Jie Zhao, Gang Tang, Ying Zhang, Jinhua Sun (2015) Effects of altitude and inclination on the flame structure over the insulation material PS based on heat and mass transfer, *International Journal of Heat and Mass Transfer*, Volume 90, 1046-1055.
- [41] Jun-Rui Shi, Mao-Zhao Xie, Zhi-Jia Xue, You-Ning Xu, Hong-Sheng Liu (2012) Experimental and numerical studies on inclined flame evolution in packing bed, *International Journal of Heat and Mass Transfer*, Volume 55, Issues 23–24, 7063-7071.
- [42] Colin Miller, Wei Tang, Mark Finney, Sara McAllister, Jason Forthofer, Michael Gollner (2017) An investigation of coherent structures in laminar boundary layer flames, *Combustion and Flame*, 181, 123–135.
- [43] Ajay V. Singh, Michael J. Gollner (2017) Steady and transient pyrolysis of a non-charring solid fuel under forced flow, *Proceedings of the Combustion Institute*, Volume 36, Issue 2, 3157-3165.

- [44] R.C. Aldredge (2017) Flame propagation in multiscale transient periodic flow, *Combustion and Flame*, Volume 183, 166-180.
- [45] Weigang Yan, Yang Shen, Weiguang An, Lin Jiang, Jinhua Sun (2017) Experimental study on the width and pressure effect on the horizontal flame spread of insulation material, *International Journal of Thermal Sciences*, Volume 114, Pages 114-122.
- [46] Isaac T. Leventon, Jing Li, Stanislav I. Stoliarov (2015) A flame spread simulation based on a comprehensive solid pyrolysis model coupled with a detailed empirical flame structure representation, *Combustion and Flame*, Volume 162, Issue 10, 3884-3895.
- [47] K. Tsai, F. Wan (2005) Upward flame spread: the width effect, *Fire Saf. Sci.*, 8, 409-419.
- [48] Markstein, G.H. and DeRis, J. (1992), *Wall-Fire Radiant Emission, Part 2: Radiation and Heat Transfer from Porous-Metal Wall Burner Flames*, 24th (International) Symposium on Combustion, Pittsburgh, PA, 1747.
- [49] A.V. Singh, M.J. Gollner (2015) Steady and transient pyrolysis of a non-charring solid fuel under forced flow, *Proceedings of the Combustion Institute* 36 (2), 3157-3165.
- [50] Ajay V. Singh, and Michael J. Gollner (2016) Experimental Methodology for Estimation of Local Heat Fluxes and Burning Rates in Steady Laminar Boundary Layer Diffusion Flames, *J Vis Exp.* (112): 54029.

- [51] Ajay V. Singh, Michael J. Gollner (2016) Local Burning Rates and Heat Flux for Forced Flow Boundary-Layer Diffusion Flames, *AIAA Journal*, Vol. 54, No. 2, 408-418.
- [52] Ajay Singh. A Fundamental Study of Boundary Layer Diffusion Flames, Dissertation, 2015, University of Maryland.
- [53] B. M. Cetegen and T. Ahmed (1993) Experiments on the periodic instability of plumes and fires, *Combust. Flame*, 93, 157.
- [54] Cetegen, B. M. and Dong, Y. (2000) Experiments on instability modes of buoyant diffusion flames and effects of ambient atmosphere on instabilities”, *Experiments in Fluids*, Vol. 28 (6), 546-558.
- [55] D. J. Rasbash, Z. W. Rogowski and G. W. V. Stark (1956) Properties of fires of liquids. *Fuel*, 35, 94-107.
- [56] A. Hamins, J. C. Yang and T. Kashiwagi (1992) An experimental investigation of the pulsation frequency of flames. *Twenty-fourth Symposium (International) on Combustion*, The Combust. Institute, pp. 1695-1702.
- [57] W.M. Malalasekera, H.K. Versteeg, K. Gilchrist (1996) A review of research and an experimental study on the pulsation of buoyant diffusion flames and pool fires, *Fire Mater.*, 20, 261–271.
- [58] E. J. Weckman and A. Sobiesiak (1988) The oscillatory behavior of medium-scale pool fires. *Twenty-Second Symposium (International) on combustion*, The Combust. Institute, 22, 1299-1310.
- [59] Cetegen, B. M. (1998) A phenomenological model for near-field fire plume entrainment *Fire Safety Journal*, Vol. 31, 299 – 312.

- [60] Cetegen, B. M. (1997) Behavior of naturally oscillating and periodically forced axisymmetric buoyant plumes of helium and helium-air mixtures, *Physics of Fluids*, Vol. 9. No. 12, 3742-3753.
- [61] Ahmed F. Ghoniem, Issam Lakkis, Marios Soteriou, (1996) Numerical simulation of the dynamics of large fire plumes and the phenomenon of puffing, *Symposium (International) on Combustion*, Volume 26, Issue 1, 1531-1539.
- [62] W. M. G. Malalasekera, H. K. Versteeg, and K. Gilchrist (1996) A review of research and an experimental study on the pulsation of buoyant diffusion flames and pool fires, *Fire and Materials*, Vol. 20, No. 6. 261–271.
- [63] G. M. Byram and R. M. Nelson (1970) The modeling of pulsating fires, *Fire Technology*, Vol. 6, No. 2, 102–110.
- [64] Christopher R. Shaddix, Joel E. Harrington, Kermit C. Smyth (1994) Quantitative measurements of enhanced soot production in a flickering methane/air diffusion flame, *Combustion and Flame*, Volume 99, Issues 3–4, 723-732.
- [65] Fei Tang, Longhua Hu, Qiang Wang, Zhongjun Ding (2014) Flame pulsation frequency of conduction-controlled rectangular hydrocarbon pool fires of different aspect ratios in a sub-atmospheric pressure, *International Journal of Heat and Mass Transfer*, 76, 447–451.
- [66] Hiroki Abe, Akihiko Ito, Hiroyuki Torikai (2015) Effect of gravity on puffing phenomenon of liquid pool fires, *Proceedings of the Combustion Institute* 35 2581–2587.
- [67] E. E. Zukoski, B. M. Cetegen, T. Kubota (1984) Visible Structure Of Buoyant Diffusion Flames, *The Proceedings of the Combustion Institute*, 361-366.

- [68] P. Thomas (1963) The size of flames from natural fires, Symposium (International) on Combustion Volume 9, Issue 1, 844-859.
- [69] Gunnar Heskestad (1983) Luminous heights of turbulent diffusion flames, Fire Safety Journal Volume 5, Issue 2, 103-108.
- [70] Gunnar Heskestad (1984) Engineering relations for fire plumes, Fire Safety Journal Volume 7, Issue 1, 25-32.
- [71] Longhua Hu, Long Wu, Shuai Liu (2013) Flame length elongation behavior of medium hydrocarbon pool fires in cross air flow, Fuel Volume 111, 613-620.
- [72] Byram GM (1959) Forest fire behavior. In 'Forest Fire Control and Use'. (Ed. K Davis) Ch. 4, pp. 90–123. (McGraw-Hill: New York).
- [73] J. Moorhouse (1982) Scaling criteria for pool fires derived from large-scale experiments, Intl Chem Sym, 71, 165-179.
- [74] C.S. Lam, E.J. Weckman (2015) Wind-blown pool fire, Part II: Comparison of measured flame geometry with semi-empirical correlations, Fire Saf. J., 78, 130–141.
- [75] J.R. Welker, C.M. Sliepcevich (1966) Bending of wind-blown flames from pool fires, Fire Technol., 2, 127–135.
- [76] P.K. Raj (2010) A physical model and improved experimental data correlation for wind induced flame drag in pool fires, Fire Technol., 46, 579–609.
- [77] V.B. Apte, .R.W. Bilger (1991) Wind-aided turbulent flame spread and burning over large-scale horizontal PMMA surfaces, Combustion and Flame, Volume 85, Issues 1–2, 169-184.

- [78] Tang W., Gorham D., Gollner M., Forthofer J., Finney M. (2015) Forward pulsation behavior of wind-driven line fires. 9th U. S. National Combustion Meeting.
- [79] Tang W., Finney M., McAllister, S., Gollner M. (2017) An experimental study of the flame intermittent frequencies of wind-driven fires, 10th U. S. National Combustion Meeting.
- [80] Wei Tang, Daniel J. Gorham, Mark A. Finney, Sara Mcallister, Jack Cohen, Jason Forthofer, Michael J. Gollner, (2017) An experimental study on the intermittent extension of flames in wind-driven fires, Fire Safety Journal, in press.
- [81] C. Miller, M. Finney, S. McAllister, T. Grumstrup, E. Sluder, W. Tang, M. Gollner, (2017) Investigating streak-like structures in boundary layer combustion via heated plates, 10th U. S. National Combustion Meeting.
- [82] <https://www.dantecdynamics.com/>
- [83] <http://www.omega.com/section/thermocouples.html>
- [84] <http://www.vatell.com/node/5>
- [85] <http://medtherm.com/>
- [86] <http://www.ni.com/en-us/support/model.ni-9214.html>
- [87] Christian M. Rippe, Brian Y. Lattimer, (2015) Full-field surface heat flux measurement using non-intrusive infrared thermography, Fire Safety Journal, Volume 78, 238-250.
- [88] Xavier Silvani, Frédéric Morandini (2009) Fire spread experiments in the field: Temperature and heat fluxes measurements, Fire Safety Journal, Volume 44, Issue 2, 279-285.

- [89] W. Tang, L.H. Hu, L.F. Chen (2013) Effect of blockage-fire distance on buoyancy driven back-layering length and critical velocity in a tunnel: An experimental investigation and global correlations, *Applied Thermal Engineering*, Volume 60, Issues 1–2, 7–14.
- [90] Back, G., Beyler, C.L., Dinunno, P. and Tatem, P. (1994) Wall Incident Heat Flux Distributions Resulting From An Adjacent Fire, *Fire Safety Science* 4: 241-252.
- [91] Moghtaderi, B., Novozhilov, V., Fletcher, D.F., Kent, J.H. and Apte, V.B. (1997) Effect Of Water Spray On Re-ignition Characteristics Of Solid Fuels, *Fire Safety Science* 5: 829-840.
- [92] K. Mekki, A. Atreya, S. Agrawal, I. Wichman (1990) Wind-Aided Flame Spread Over Charring And Non-Charring Solids: An Experimental Investigation, *Twenty-Third Symposium (International) on Combustion*, 1701-1707.
- [93] N. Luo, W.G. Weng, M. Fu (2015) Theoretical analysis of the effects of human movement on the combined free-forced convection, *Int. J. Heat Mass Transfer*, 91, 37–44.
- [94] H. Imura, R.R. Gilpin, K.C. Cheng (1978) Experiments on the onset of longitudinal vortices in Horizontal Blasius flow heated from below, *J. Heat Transfer*, 100, 429–434.
- [95] H. F. Oztop, I. Dagtekin (2004) Mixed convection in two-sided lid-driven differentially heated square cavity, *Int. J. Heat Mass Transfer*, 47, 1761–1769.
- [96] Anthony W. Strawa, Brian J. Cantwell (1985) Visualization of the structure of a pulsed methane–air diffusion flame, *Physics of Fluids*, 28, 2317.

- [97] Raj Kamal Tiwari, Manab Kumar Das (2007) Heat transfer augmentation in a two-sided lid-driven differentially heated square cavity utilizing Nano-fluids, *International Journal of Heat and Mass Transfer*, Volume 50, Issues 9–10, 2002-2018.
- [98] Said Turki, Hassen Abbassi, Sassi Ben Nasrallah (2003) Two-dimensional laminar fluid flow and heat transfer in a channel with a built-in heated square cylinder, *International Journal of Thermal Sciences*, 42, 1105–1113.
- [99] B Porterie, D Morvan, JC Loraud, M Larini (2000) Fire spread through fuel beds: Modeling of wind-aided fires and induced hydrodynamics, *Physics of Fluids*, 12, 1762.
- [100] [https://en.wikipedia.org/wiki/Otsu%27s\\_method](https://en.wikipedia.org/wiki/Otsu%27s_method)
- [101] L. Audouin, G. Kolb, J.L. Torero, J.M. Most (1995) Average centreline temperatures of a buoyant pool fire obtained by image processing of video recordings, *Fire Safety J.*, 24(2):167-187.
- [102] R.F. Blackwelder, R.E. Kaplan (1976) On the wall structure of the turbulent boundary layer. *J. Fluid Mechanics*, 76(1): 89-112.
- [103] Longhua Hu, Chen Kuang, Xinpeng Zhong, Fei Ren, Xiaolei Zhang, Hang Ding (2017) An experimental study on burning rate and flame tilt of optical-thin heptane pool fires in cross flows, *Proceedings of the Combustion Institute*, Volume 36, Issue 2, 3089–3096.
- [104] Longhua Hu, Shuai Liu, John L. de Ris, Long Wu (2013) A new mathematical quantification of wind-blown flame tilt angle of hydrocarbon pool fires with a new global correlation model, *Fuel*, 106, 730–736.

- [105] Beyler CL. Fire hazard calculations for large, open hydrocarbon fires, In: SFPE Handbook of Fire Protection Engineering 3, 268-314.
- [106] P. H. Thomas, C. T. Webster, M. M. Raftery (1961) Some experiments on buoyant diffusion flames, Combustion and Flame, Volume 5, 359-367.
- [107] D. J. Rasbash, Z. W. Rogowski, G. W. V. Stark (1956) Properties of Fires of Liquid, Fuel, 35, 94-107.
- [108] Oka, Yasushi, et al. (2002) Effects of Cross-Winds to Apparent Flame Height and Tilt Angle from Several Kinds of Fire Source. Fire Safety Science, 7, 915-926.
- [109] Hitoshi Kurioka, Yasushi Oka, Hiroomi Satoh, Osami Sugawa (2003) Fire properties in near field of square fire source with longitudinal ventilation in tunnels, Fire Safety Journal, 38, 319–340.
- [110] J.A.R. Woods, B.A. Fleck, L.W. Kostiuk, (2006) Effects of transverse air flow on burning rates of rectangular methanol pool fires, Combust Flame, 146, 379-390.
- [111] G. Heskestad (1981) Peak gas velocities and flame heights of buoyancy-controlled turbulent diffusion flames, Proc Combust Inst, 8, 951-960.
- [112] James G. Quintiere (2006) Fundamentals of Fire Phenomena, John Wiley & Sons Ltd, The Atrium, Southern Gate, Chichester, West Sussex PO19 8SQ, England.